

Microcomb technology: from principles to applications

Haowen Shu,^{a,b,*†} Bitao Shen,^{a,†} Huajin Chang,^a Junhao Han,^a Jiong Xiao,^c and Xingjun Wang^{a,b,c,d,e,*}

^aState Key Laboratory of Advanced Optical Communications System and Networks, School of Electronics, Peking University, Beijing, China

^bFrontiers Science Center for Nano-optoelectronics, Peking University, Beijing, China

^cWuhan National Laboratory for Optoelectronics and School of Optical and Electronic Information, Huazhong University of Science and Technology, Wuhan, China

^dPeking University Yangtze Delta Institute of Optoelectronics, Nantong, China

^ePeng Cheng Laboratory, Shenzhen, China

Abstract. Integrated microcombs bring a parallel and coherent optical frequency comb to compact chip-scale devices. They offer promising prospects for mass-produced comb sources in a compact, power-efficient, and robust manner, benefiting many basic research and practical applications. In the past two decades, they have been utilized in many traditional fields, such as high-capacity parallel communication, optical frequency synthesis, frequency metrology, precision spectroscopy, and emerging fields like distance ranging, optical computing, microwave photonics, and molecule detection. In this review, we briefly introduce microcombs, including their physical model, formation dynamics, generation methods, materials and fabrications, design principles, and advanced applications. We also systematically summarize the field of integrated optical combs and evaluate the remaining challenges and prospects in each aspect.

Keywords: integrated microcomb; integrated photonics; nonlinear optics.

Received Oct. 31, 2024; revised manuscript received Dec. 15, 2024; accepted Dec. 17, 2024; published online Dec. 31, 2024.

© The Authors. Published by CLP and SPIE under a Creative Commons Attribution 4.0 International License. Distribution or reproduction of this work in whole or in part requires full attribution of the original publication, including its DOI.

[DOI: [10.3788/PI.2024.R09](https://doi.org/10.3788/PI.2024.R09)]

1 Introduction

Optical frequency comb technology has been revolutionizing a wide range of fields, especially the precise metrology related to counting time, a fundamental physical quantity that underpins much of modern science and technology^[1,2]. Initially, the term “optical frequency comb” referred explicitly to self-referenced mode-locked lasers^[3]; however, the concept has been broadened to encompass various optical sources consisting of multiplex discrete frequency components with equal spacing and spanning broadband. The exceptional coherence and stabilization properties of optical frequency combs provide unprecedented precision in measuring time and frequency, facilitating applications such as optical atomic clocks^[4], ultraprecise sensing^[5], and high-resolution spectroscopy^[6]. Despite their transformative potential, traditional mode-locked laser systems often face

limitations due to their size, cost, and complexity, which hinder their integration into more compact and scalable chip-based systems. In the early 2000s, researchers sought to miniaturize this technology, leading to the development of microcombs—frequency combs generated in microcavities through nonlinear optical effects^[7,8].

The basic setup for microcomb generation includes a high-quality-factor (high- Q) microcavity and an external pump laser. As the pump laser couples into the microcavity, it builds up a strong intracavity optical field sufficient to excite nonlinear optical effects. The balance between nonlinear gain and cavity loss and between nonlinear phase shift and cavity dispersion enables the system to support mode-locked pulse states, commonly referred to as dissipative solitons^[9]. The theoretical prediction of the existence of dissipative solitons was laid out through simulations with the Lugiato–Lefever equation (LLE), which describes the dynamics of the optical field within the cavity^[10]. Despite this, initial experimental attempts to achieve the mode-locked state encountered significant challenges. Factors such as thermal instability, dispersion management, and the

*Address all correspondence to Haowen Shu, haowenshu@pku.edu.cn; Xingjun Wang, xjwang@pku.edu.cn

†These authors contributed equally to this work.

necessity for precise control over the resonator geometry posed substantial hurdles for researchers. However in 2014, a significant breakthrough was achieved when the mode-locked state was successfully observed in optical microcavities^[11], marking a pivotal milestone in integrated microcombs.

Integrated microcomb technology generally represents a remarkable synthesis of nonlinear dynamics, material science, advanced nanofabrication, and broad engineering applications. The cornerstone of this technology is the realization of integrated microcavities, which are fundamental to achieving high-performance microcombs. Various platforms have been developed to accomplish this, each employing distinct fabrication processes that have enabled the production of integrated microcavities with quality (Q) factors exceeding 10^8 ^[12]. Based on the diverse platforms^[13–26], researchers have gained a deeper understanding of the underlying principles and dynamics of microcomb generation. On the other hand, advancements in design methodologies have unveiled numerous mode-locked states^[11,27–33], each emerging under different dispersion regimes and interactions with various physical fields. These states are crucial for enabling a diverse range of applications. Initially focused on traditional frequency comb applications such as atomic clocks^[34], precise sensing^[35], and spectroscopy^[36], the scope has broadened considerably. New applications have emerged, leveraging the unique properties of microcombs in optical communication^[37], parallel LiDAR^[38], optical signal processing^[39], and even chaotic information systems^[40]. Furthermore, integrating microcomb technology with other photonics technologies has catalyzed the development of highly minimized systems^[41]. These integrated systems combine remarkable volume, capacity, speed, precision, scalability, and compactness, representing a significant leap forward. By merging with broader integrated photonics, these systems enhance existing applications and create new possibilities in the realm of optical and electronic engineering.

This review offers a thorough examination of the advancements in microcomb technology, according to the developmental timeline illustrated in Fig. 1. The review is structured into four main sections, each dedicated to a different aspect of microcomb development: principles, fabrication, design, and applications.

I. Fundamental Principles. The second section outlines the fundamental principles underlying microcomb generation. It discusses the dynamics of generation and various mode-locked pulses, including bright solitons and dark pulses. This section also explores the different equations used for the simulation and analysis of microcombs, providing a theoretical framework that supports experimental methods. Various experimental generation techniques are detailed, highlighting strategies such as precise pump frequency and power tuning, auxiliary laser cooling, and self-injection locking.

II. Materials and Integration. The third section surveys the material platforms and fabrication processes critical for developing integrated microcomb devices. It compares different substrate materials—metal fluorides and silicon dioxide to Hydex, silicon nitride, chalcogenides, group IV semiconductors, III–V compound semiconductors, and electro-optical crystals—each chosen for their unique properties that benefit specific applications. Additionally, it addresses the methods used for packaging and integrating these materials into miniaturized microcomb modules or chips.

III. Characteristics and Design. The fourth section reviews the key parameters for device characterizations and the design

method for spectral shape tuning, conversion efficiency enhancement, and noise suppression, outlining the critical design considerations that enhance performance and functionality.

IV. Applications. The fifth section discusses the broad range of applications for microcombs, from high-precision metrology and sensing to parallel data transmission and advanced signal processing. It highlights the latest applications developed and the progress toward miniaturized systems, setting the stage for future fully integrated microcomb systems.

Finally, the review concludes with recent progress and challenges in microcomb technology. We also envision the future of fully integrated microcomb systems for diverse applications.

2 Fundamental Principles

As a type of optical frequency comb, the microcomb consists of distinct optical frequency components with fixed phase relationships^[70], as depicted in Fig. 2. According to the Fourier transform relation, the microcomb can be viewed as periodic pulse trains in the time domain. In the frequency domain, a particular optical mode of the microcomb can be described with the well-known comb equation^[1]

$$f_n = n f_{\text{rep}} + f_{\text{ceo}}. \quad (1)$$

f_n is the frequency of n -th mode of the microcomb. f_{rep} is usually called the repetition frequency, representing the equal distance between comb lines and the repetition rate of the period pulse train. f_{ceo} is called the carrier envelope offset (CEO) frequency. Thus, the precise frequency of each frequency component and the pulse envelope evolution as propagating in a cavity can be well determined with the restriction of these two-dimensional freedoms.

A typical microcomb setup comprises a pump laser and a high- Q optical nonlinear microcavity. When the pump light is resonant within the microcavity, an optical field with ultrahigh power density is tightly confined within nanowaveguide structures^[89]. Microcombs are produced when the conditions for nonlinear effects, typically four-wave mixing (FWM)^[91], are met. With the power enhancement of microcavities, the nonlinear effects are significantly enhanced with moderate pump power, unlike mode-locked lasers, where the gain spectrum of the medium limits the bandwidth, and the microcomb bandwidth is determined by the optical nonlinear processes, allowing for broader spectral coverage. The high nonlinear parametric gain is necessary to compensate for the intrinsic loss^[91] to stimulate comb lines. Thus, microresonators are well-suited nonlinear boosters due to extreme light confinement and power enhancement effects. Meanwhile, microresonator dispersion engineering is crucial to meet phase-matching conditions with nonlinear phase shifts, allowing parametric oscillation efficiency. According to the analysis above, the formation of a microcomb requires the balance of nonlinear gain and cavity loss, as well as nonlinearity and dispersion, which always needs delicate design of microcavities, such as mode-volume, coupling efficiency, and dispersion.

2.1 Formation Dynamic

The formation process of microcombs shows rich evolution dynamics. Existing microcomb states, such as primary comb states, chaotic states, and the mode-locked dissipative Kerr soliton (DKS) state, are highly related to the cavity characteristics

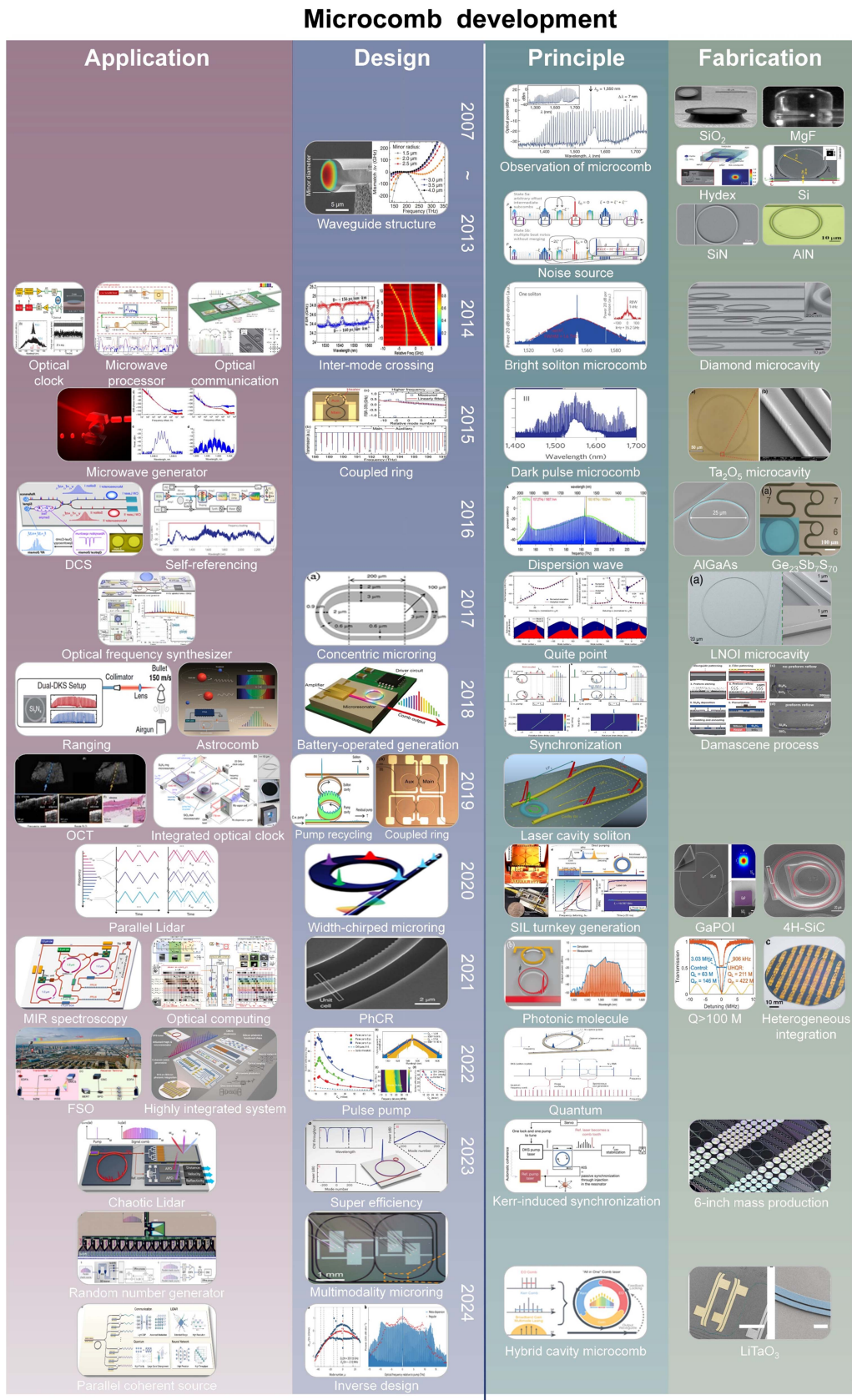


Fig. 1 Timeline of the microcomb technology development. The four columns from left to right are developments of the application, the design, the principle, and the fabrication, respectively.

Abbreviations: DCS, dual-comb spectroscopy; OCT, optical coherence tomography; MIR, mid-infrared; FSO, free-space optical communication; PhCR, photonic crystal ring; SIL, self-injection locked; Q, quality factor; M, million. References: optical clock^[42]; microwave processor^[43]; optical communication^[37]; microwave generator^[44]; dual-comb spectroscopy^[36]; self-referencing^[45]; optical frequency synthesizer^[46]; ranging^[35]; astrocomb^[47]; OCT^[48]; integrated optical clock^[34]; parallel LiDAR^[49]; MIR spectroscopy^[50]; optical computing^[51]; FSO^[52]; highly integrated system^[53]; chaotic LiDAR^[54]; random number generator^[55]; parallel coherent source^[56]; waveguide structure^[57]; inter-mode crossing^[58]; efficient coupled ring^[59,60]; concentric microring^[61]; battery-operated generation^[62]; pump recycling^[63]; width-chirped microring^[64]; PhCR^[65]; pulse pump^[66]; super efficiency^[67]; multimodality microring^[68]; inverse design^[69]; observation of microcomb^[70]; noise source^[71]; bright soliton microcomb^[11]; dark pulse microcomb^[72]; dispersion wave^[73]; quiet point^[74]; synchronization^[75]; laser cavity soliton^[76]; SIL turnkey generation^[77]; photonic molecule^[78]; quantum^[79]; Kerr-induced synchronization^[80]; hybrid cavity microcomb^[81]; SiO₂^[82]; MgF₂^[14]; Hydex^[15]; Si^[16]; SiN^[17]; AlN^[18]; diamond microcavity^[19]; Ta₂O₅ microcavity^[20]; AlGaAs microcavity^[21]; Ge₂₃Sb₇S₇₀^[22]; LNOI microcavity^[23]; Damascene process^[83]; GaPOI^[84]; 4H-SiC^[25]; Q > 100 M^[85]; heterogeneous integration^[86]; 6-inch mass production^[87]; LiTaO₃^[88].

and excitation conditions. They represent distinct features in the time and frequency domains. When tuning the pump laser from the effective blue-detuned regime into the effectively red-detuned regime, as shown in Fig. 2, the resonance frequency is shifted towards lower frequencies by Kerr nonlinearity and thermal effects when intracavity power increases. As the intracavity power builds up, cascaded FWM gives rise to equidistant and coherent optical components with a spacing constrained to the microcavity's free spectral range (FSR). Figure 3 illustrates the numerical simulation [Fig. 3(a)] and experimental results [Fig. 3(b)] of the comb formation in anomalous dispersion microresonators, which goes through various regimes, including primary comb states, chaotic states, and multiple- and single-soliton states.

(a) Primary comb state: as the pump laser wavelength is tuned into resonance, the intracavity power gradually increases, approaching the resonant state. When the phase-matching condition is satisfied, the rising intracavity power intensifies nonlinear effects such as degenerate four-wave mixing. Once the parametric gain in the microcavity exceeds the intrinsic decay rate, sparsely spaced symmetrical comb lines form on both sides of the pump light. This process is known as parametric oscillation^[8,93]. The mode number μ_{th} of the first sideband is typically separated by several FSRs from the pump mode and can be approximated by the following equation^[11]:

$$\mu_{th} = \sqrt{\frac{\kappa}{D_2}}. \quad (2)$$

(b) Subcomb state and chaotic state: as the pump laser approaches the resonance, subcombs are generated around primary comb lines, eventually covering the entire band. Due to the mismatch between the primary comb line spacing and the subcomb line spacing, multiple frequency components appear near each resonance, leading to reduced coherence. The complex nonlinear effects between the subcombs are intensively enhanced when the pump approaches the resonant peak, nearly reaching the maximum intracavity power. The intense interaction between the comb teeth causes erratic power fluctuations, exhibiting random modulation in both the time and frequency domains, with the noise bandwidth increasing alongside the intracavity power. The behavior of the intracavity field displays a spatiotemporal chaotic nature^[55,94,95]. In addition, the chaotic comb lines present an uncorrelated characteristic.

(c) DKS state: when the pump laser scans across the resonance, a unique mode-locking transition occurs, resulting from the double balance between the nonlinearity and dispersion, as well as loss and gain. In the frequency domain, all comb lines establish a stable phase relationship with each other, overcoming earlier issues of low coherence. In the time domain, periodic pulse trains are formed, characterized by high-intensity peaks on

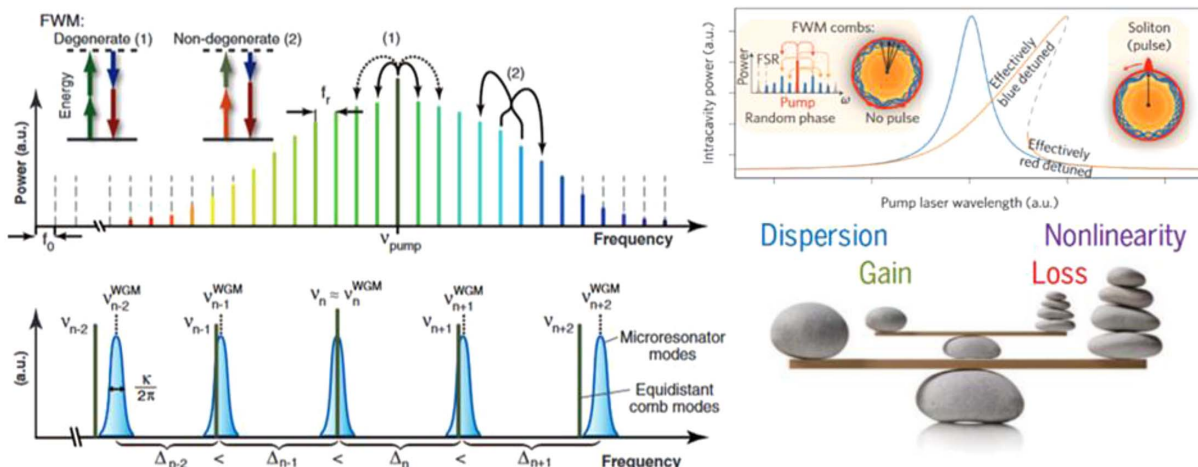


Fig. 2 The basic principles of microcombs^[11,89,90].

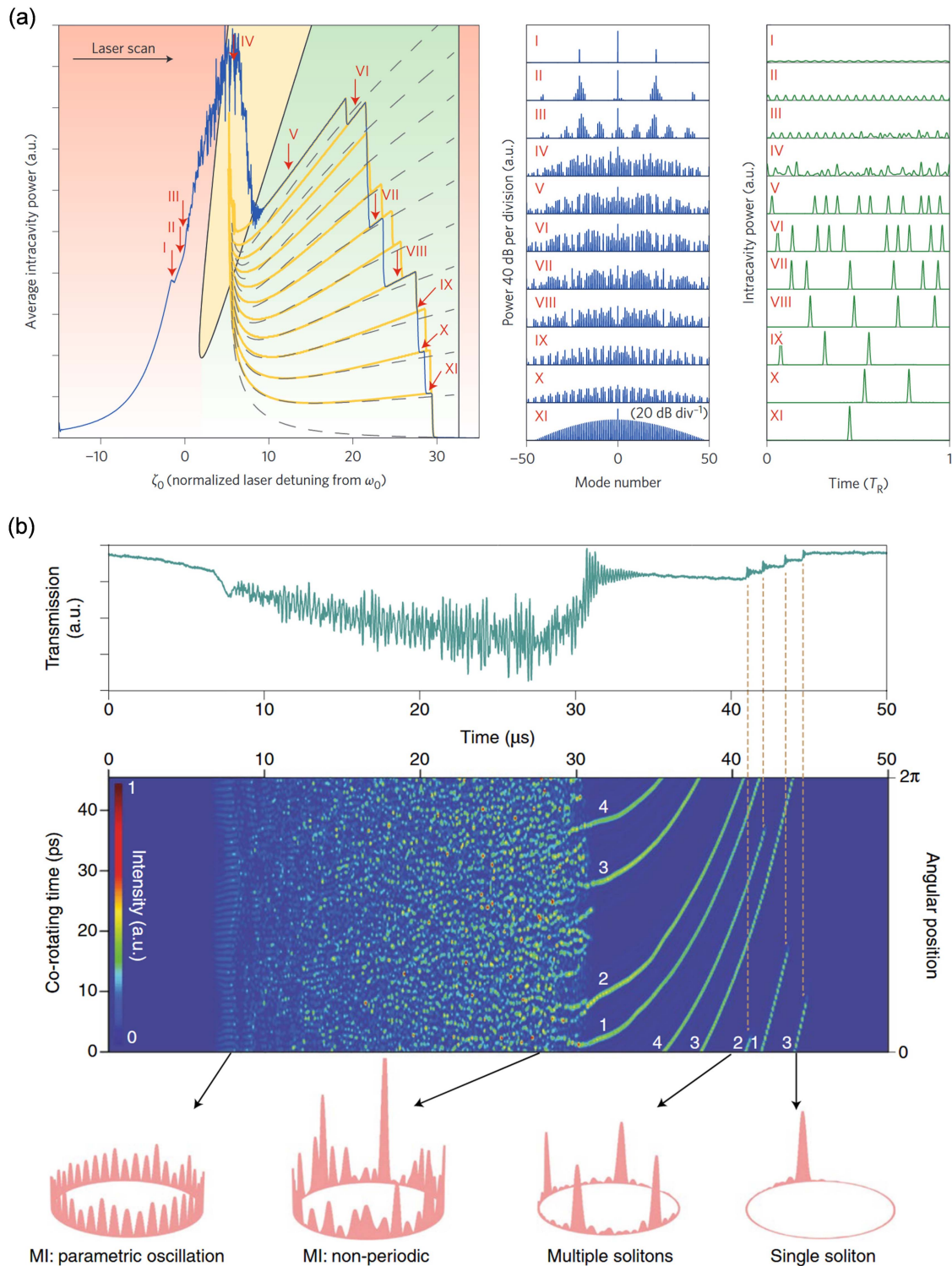


Fig. 3 Dynamic evolution of mode-locked soliton formation in a microresonator^[11,92] (a) Numerical simulation results. Average intracavity power trace during the laser scan. The colored region shows the existing area of different comb states: soliton state (green), breather solitons with time-variable envelop (yellow), and solitons cannot exist (red). (b) Experimental observation of soliton steps, Top: pump power transmission of a silica microresonator as the pump tunes, exhibiting multiple steps indicative of soliton formation. Middle: imaging of soliton formation corresponding to the scan where the x-axis is time, and the y-axis is time in a frame that rotates with the solitons. Bottom: soliton intensity patterns measured at four moments, mapped onto the microcavity coordinate frame.

a low background. These pulses, referred to as bright solitons, are robust waveforms that preserve the stable envelope during propagation in the dispersive media. Unlike fiber cavities, soliton pulses in dissipative microcavities form spontaneously without needing external stimulation^[96].

Apart from bright solitons, there are diverse mode-locked pulses under different conditions. In Table 1, we summarize the characteristics of different mode-locked states, including bright solitons^[11,96], dark solitons^[58,72], breather solitons^[97–101], soliton crystals^[102–107], soliton molecules^[108], Stokes solitons^[31], Brillouin–Kerr solitons^[32,109], and laser cavity solitons^[76,110].

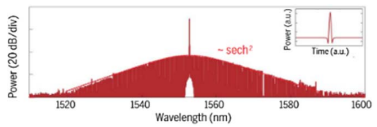
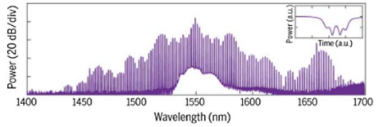
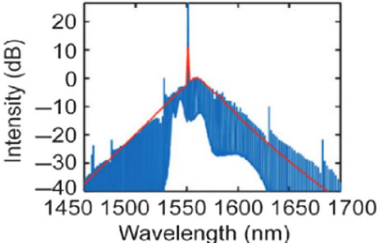
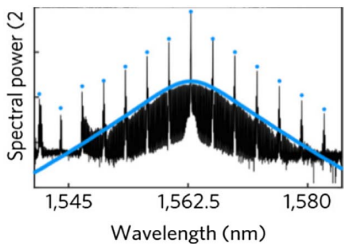
As aforementioned, bright solitons^[11] are generated in anomalous dispersion microcavities when tuning the pump laser from blue-detuning to effective red-detuning. These solitons are stable eigen-solutions of the LLE for anomalous dispersion^[10,111]. As shown in Fig. 3(a), there are multiple distinct steps in the intracavity power profile, each representing specific order solitons. The soliton order typically describes the number of solitons within a roundtrip, depending on the evolution dynamic and the pump-cavity detuning. With the continuous transition from different steps, the soliton number decreases, finally reaching the single-soliton state. The single bright soliton state exhibits low-noise radio-frequency (RF) beat notes and smooth spectral envelopes.

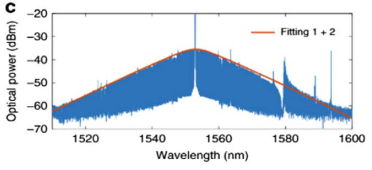
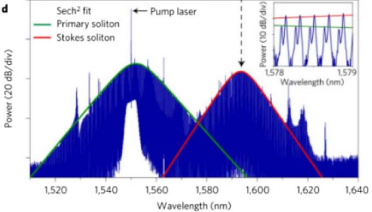
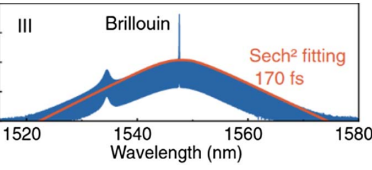
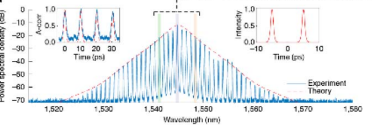
In contrast, dark pulses^[72] exhibit periodic dips in the time domain. These dark pulses are stable eigen-solutions in normal dispersion cavities. The mode-locking process can be explained as the balanced propagation of two switching waves in opposite directions. The dark pulses cannot be spontaneously stimulated through the sweeping process due to the absence of parametric gain in normal dispersion cavities. The experiment observation of dark pulses is usually assisted by effective anomalous dispersion with inter-mode coupling, as shown in Sec. 4.

Based on bright and dark solitons as general solutions, varieties of soliton types can be demonstrated by exploiting other effects such as dynamic instability, solitons interactions, phonon–photon interaction, and hybridization with gain media, corresponding to breather solitons^[99], soliton crystals^[102], soliton molecules^[108], Stokes solitons^[31], Brillouin–Kerr solitons^[32], and laser cavity solitons^[76].

Bounded with the intracavity field, multiple solitons with equal distance within the roundtrip can be self-organized, known as perfect soliton crystals^[102]. Due to the coherent interaction among regular temporal solitons, the perfect soliton crystal exhibits a sech^2 envelope with comb line spacing several times the FSR^[102,106]. When defects such as the absence or the dislocation of solitons are present, the incomplete coherence cancellation causes clusters of comb lines around the primary

Table 1 Summary of Different Mode-Locked Soliton States of Microcombs

Soliton Type	Characteristic	Dispersion	Typical Spectrum
Bright solitons ^[11]	The power spectral envelope exhibits a sech^2 shape corresponding to temporal pulses.	Anomalous	
Dark solitons ^[72]	Time domain dark pulses (flat-topped bright soliton pulses) and high conversion efficiency.	Normal	
Breather solitons ^[100]	Periodically varying soliton peak intensity and duration.	Both	
Soliton crystals ^[102]	Unique “fingerprint” spectrum and dense soliton pulses in the time domain.	Anomalous	

Soliton molecules ^[108]	As boundary states of solitons, distinct soliton states are superposed with different carrier frequencies.	Anomalous	
Stokes solitons ^[31]	Two solitons with the Stokes soliton formed around the Raman gain band of the primary soliton in the spectrum.	Anomalous	
Brillouin–Kerr solitons ^[32]	The soliton comb exhibits narrow-linewidth comb lines and a stable repetition rate.	Anomalous	
Laser cavity solitons ^[76]	The soliton states exhibit incredibly high conversion efficiencies and robust self-emergence characteristics.	Anomalous	

lines, exhibiting a unique “fingerprint” spectrum. The formation of soliton crystal is usually related to the background field induced by inter-mode coupling or the additional applied field, leading to the deterministic arrival. Combined with the high power of high-order soliton states, high-order soliton crystals feature high power efficiency and robust generation, which is critical for applications such as optical communication. Unlike the soliton crystal, soliton molecules are the bound states of solitons that rely on a balance between attractive and repulsive effects. They can be generated by engineering the interaction among co-existing solitons using modulated light to pump the same resonance^[108].

Distinct from the stationary soliton states mentioned above, the breather solitons manifest as periodic oscillations in pulse amplitude and duration. The breather soliton regime is between MI and the steady soliton regime^[100]. Also, the breathing dynamic can exist within the region where the stable soliton solutions are expected^[98] with the inter-mode coupling process. Such breathing dynamic originated from the periodic energy exchange between the soliton in the primary mode and the optical field in a second mode. With a period-doubling bifurcation process, chaotic solitons^[112] can be formed from the breather soliton.

Apart from Kerr effects, other third-order nonlinear effects, such as the nonlinear scattering processes, can give rise to new types of mode-locking processes. Stokes solitons^[31] are generated through Kerr-effect trapping and Raman amplification with a temporal soliton. The spectrum of the Stokes soliton is effectively redshifted relative to the initial soliton, and the two solitons usually belong to different transverse mode families.

Generating new solitons relies on the Raman gain when two solitons overlap in time and space. Their repetition rates are locked by Kerr nonlinearity. Brillouin–Kerr solitons^[32,109] are generated by stimulating a red-detuned Brillouin laser with a blue-detuned pump. Utilizing the interactions, the monostable single-soliton microcomb can deterministically access without feedback controls^[32]. Due to the high gain and narrow band of the stimulated Brillouin scattering (SBS), the new type of soliton comb features ultrahigh coherence, which is meaningful for low-noise microwave signal generation.

Laser cavity solitons (LCSs) are a new type of microcomb-based solitons achieved by nesting a microresonator in a fiber cavity with gain^[76,110]. Unlike externally driven cavity solitons, which are sustained by the energy of the continuous wave (CW) background, the LCSs receive energy directly from the gain medium. This fundamental principle makes LCSs extremely energy efficient with a theoretical max mode efficiency of 96% versus the theoretical limit of 5% for bright Lugiato–Lefever solitons^[76], as reviewed in Sec. 4. Through delicately tailoring the system parameters, especially the EDFA pump power and the laser cavity length, the targeted soliton states become the dominant attractor of the system, which can self-recover after a disruption. The LCSs offer new solutions for the turnkey and robust microcombs for real-world applications.

Except for the above mode-locked states, other states have been observed and understood, such as parametric solitons^[113,114], Pockels solitons^[115], Nyquist solitons^[116], and mode-locked pulses with high-order dispersion. These rich evolution dynamics with distinctive characteristics give microcombs potential for abundant application scenarios.

2.2 Simulation Method

As the microcomb benefits many fundamental researches and applications due to its compact size and low power consumption, it is necessary to fully understand and control it. Comb generation in microresonators involves the interaction of several cavity modes, which highly relates to cavity dispersion, pump condition, and complex nonlinear effects. Many mathematical models have been brought up to describe the formation dynamic of microcombs. Parametric oscillations are first studied mainly by focusing on a signal and an idler side mode through degenerate four-wave mixing^[8,117]. The threshold conditions and effects of dispersion are discussed^[111]. With more modes considered, the coupled mode equations (CMEs) can be used to describe the intracavity dynamic. While the microcomb tends to cover a wide span with hundreds or even thousands of modes, the calculation complexity based on CMEs significantly increases. To address this problem, the nonlinear Schrödinger equation (NLSE), widely used to describe pulse evolution in nonlinear media, is induced to understand intracavity dynamics. The Ikeda map and the LLE^[10] are proposed with reduced computation complexity and high accuracy.

2.2.1 Coupled mode equations

The equilibrium of pumping and dissipation, intracavity dispersion, and nonlinearity realize a microcavity's optical frequency comb generation. Chembo and Yu proposed a method based on CMEs^[111] to describe the complex evolution of comb modes in a cavity. In the coupled mode equations, each mode is treated as an individual electromagnetic field component, and all the comb teeth interact with each other through Kerr nonlinear effects such as four-wave mixing.

Modeling spatiotemporal systems usually requires a set of partial differential equations describing the evolution of every spatial point. Although this method can precisely calculate the field within the volume of interest, solving complex mathematical models is quite time-consuming. The modal expansion methods in CMEs rely on the fact that the spatial mode distributions are already known. Here, we considered a series of optical cavity modes. Based on the classical wave equation^[118]

$$\left[\Delta - \frac{\epsilon(\mathbf{r}, \omega, \|\mathbf{E}\|^2)}{c^2} \frac{\partial^2}{\partial t^2} \right] \mathbf{E}(\mathbf{r}, t) = 0, \quad (3)$$

the relative permittivity is ϵ , defined as

$$\epsilon(\mathbf{r}, \omega, \|\mathbf{E}\|^2) = \begin{cases} n^2(\omega, \|\mathbf{E}\|^2) & \text{if } r \leq a \\ 1 & \text{if } r > a \end{cases}. \quad (4)$$

We can expand the electromagnetic field with the eigenmodes as

$$\mathbf{E}(\mathbf{r}, t) = \sum_{\mu} \frac{1}{2} \epsilon_{\mu}(t) e^{i\omega_{\mu}t} \boldsymbol{\gamma}_{\mu}(\mathbf{r}) + \frac{1}{2} \epsilon_{\text{ext}} e^{i\Omega_0 t} \mathbf{e}_0 + \text{c.c.}, \quad (5)$$

where μ represents the various modes under consideration, defined by an infinite set of orthonormal and vectorial eigenmodes $\boldsymbol{\gamma}_{\mu}(\mathbf{r})$ of absolute frequency ω_{μ} and by their time-varying amplitude $\epsilon_{\mu}(t)$. Using Eqs. (4) and (5), we can finally rewrite the initial Eq. (3); the eigenmodes can be solved with

the separated spatial part, which is illustrated in detail in Refs. [111,119]. The explicit solution of $\boldsymbol{\gamma}_{\mu}(\mathbf{r})$ will be injected in the remaining temporal evolution parts to solve the modal amplitude $\epsilon_{\mu}(t)$. Based on slowly varying amplitude expansion, orthonormality of the eigenvectors, the following equations can be obtained for the modal field dynamics:

$$\begin{aligned} \frac{dA_{\mu}}{dT} = & - \left(i\omega_{\mu} + \frac{\kappa}{2} \right) A_{\mu} + ig \sum_{\mu_1, \mu_2, \mu_3} A_{\mu_1} A_{\mu_2} A_{\mu_3}^* \\ & + \delta_{0, \mu} \sqrt{\frac{\kappa_{\text{ex}} P_{\text{in}}}{\hbar \omega_0}} e^{-i\omega_p T}, \end{aligned} \quad (6)$$

where the optical field of the μ -th comb line is denoted as A_{μ} , κ is the cavity dissipated rate, κ_{ex} is the external coupling rate between cavity mode and bus waveguide, P_{in} is the pump laser power, ω_p is the pump laser frequency, and $g = \frac{\hbar^2 c n_2}{n_0^2 V_{\text{eff}}}$ is the equivalent Kerr nonlinear coefficient in microcavity. The equation is normalized by $\hbar \omega_0$ so that $|A_{\mu}|^2$ represents the photon number. c , n_0 , n_2 , and V_{eff} are the speed of light, refractive index, Kerr nonlinear refractive index, and effective cavity mode volume, respectively. The right side of the equation consists of the dissipation term, the nonlinear gain term, and the pump term in sequence. Further simplify the equation by removing the fast oscillation of the electromagnetic field by replacement: $a_{\mu} = A_{\mu} e^{-i(\omega_p + D_1 \mu)T}$, with $\xi_{\mu} = \omega_p + D_1 \mu$ being the frequency of the μ -th comb line. Especially, the equation takes into account the four-wave mixing gain requiring the conservation of momentum to be satisfied:

$$\mu_1 + \mu_2 = \mu_3 + \mu. \quad (7)$$

Then, we can rewrite the equation as

$$\begin{aligned} \frac{da_{\mu}}{dT} = & - \left(i\omega_{\mu} - i\xi_{\mu} + \frac{\kappa}{2} \right) a_{\mu} + ig \sum_{\mu_1, \mu_2, \mu_3} a_{\mu_1} a_{\mu_2} a_{\mu_1 + \mu_2 - \mu}^* \\ & + \delta_{0, \mu} \sqrt{\frac{\kappa_{\text{ex}} P_{\text{in}}}{\hbar \omega_0}}. \end{aligned} \quad (8)$$

This equation clearly describes the basic intercoupling relationship of the comb modes that can be used for steady-state analysis. For instance, parametric oscillation occurs proficiently once nonlinear gain surpasses mode intrinsic loss. Using the coupled mode equation, the pump threshold power P_{th} for the first pair of sideband generation can be theoretically deduced as

$$P_{\text{th}} = \frac{\kappa^2 n^2 V_{\text{eff}}}{8\eta \omega_0 c n_2}. \quad (9)$$

A complete set of coupled mode equations can describe the dynamic process of a Kerr microcomb, including cascaded FWM to wideband frequency combs. However, when a large number of modes are considered, the computational cost of the model increases sharply (proportional to the cubic of exciting modes). More importantly, the model makes it difficult to describe the pulse evolution in the time domain, which is significant in studying Kerr optical frequency combs.

2.2.2 Ikeda map

Different from the coupled mode equation, where the evolution of each comb line component is described with an equation, the Ikeda map gives a general description of the whole microcomb in the time domain with the nonlinear Schrödinger equation (NLSE) and boundary conditions. The evolution of a microcomb in the microcavity can be divided by the roundtrip. The intracavity field starts from the coupled points and goes around the cavity for each roundtrip. The propagation process can be described with the nonlinear Schrödinger equation (NLSE)^[91] as

$$\frac{\partial E_m(z, \tau)}{\partial z} = -\frac{\alpha_i}{2} E_m + i \sum_{k>1} \frac{\beta_k}{k!} \left(i \frac{\partial}{\partial t} \right)^k E + i\gamma |E_m|^2 E_m, \quad (10)$$

where E_m is the optical field propagating in the cavity for the m time, z and τ are the propagation length and time, respectively, α_i is the intrinsic loss rate, β_k is the k _{th} dispersion coefficient, and γ is the Kerr nonlinear coefficient. The coupling between the cavity and the outside is considered as the following equation:

$$E_{m+1}(0, \tau) = \sqrt{\theta} E_{\text{in}} + \sqrt{1 - \theta} e^{i\phi_0} E_m(L, \tau), \quad (11)$$

where E_n is the external pump field, θ is the coupling coefficient between the external and the cavity, ϕ_0 is the phase change, and L is the roundtrip length of the cavity. The Ikeda map is formed by combining these two equations in a discrete-time iterative manner, where the intracavity nonlinear process and the coupling process are considered^[67,120].

2.2.3 LLE

Based on the Ikeda map, it is convenient to derive the LLE^[10]. Under a mean-field approximation, the optical field at the end of a roundtrip can be expressed as

$$\begin{aligned} E_m(L, \tau) - E_m(0, \tau) \\ = -L \frac{\alpha_i}{2} E_m(0, \tau) + iL \sum_{k>1} \frac{\beta_k}{k!} \left(i \frac{\partial}{\partial t} \right)^k E(0, \tau) \\ + iL\gamma |E_m(0, \tau)|^2 E_m(0, \tau). \end{aligned} \quad (12)$$

Submitting Eq. (12) into (11), we can get

$$\begin{aligned} E_{m+1} = \sqrt{\theta} E_{\text{in}} + E_m - \left(\frac{\alpha_i L + \theta}{2} + i\delta_0 \right) E_m \\ + iL \sum_{k>1} \frac{\beta_k}{k!} \left(i \frac{\partial}{\partial t} \right)^k E_m + i\gamma |E_m|^2 E_m. \end{aligned} \quad (13)$$

Finally, a slow time variable t is introduced based on the transition of

$$E(t = mt_R, \tau) = E_m(z = 0, \tau). \quad (14)$$

With the transition, the discretized roundtrip propagation process can be generated into a single deviation equation with the approximation of $[\partial E(t = mt_R, \tau)/t] = [E_{m+1}(z = 0, \tau) - E_m(z = 0, \tau)]/t_R$:

$$\begin{aligned} t_R \frac{\partial E(t, \tau)}{\partial t} = \left[-\left(\frac{\alpha'}{2} - i\delta_0 \right) + iL \sum_{k>1} \frac{\beta_k}{k!} \left(i \frac{\partial}{\partial \tau} \right)^k \right] E \\ + iL\gamma |E|^2 E + \sqrt{\theta} E_{\text{in}}, \end{aligned} \quad (15)$$

where α' is the total loss rate of the cavity and δ_0 is the detuning between the cavity resonance and the pump laser; the above equation is the well-known LLE. According to LLE, the detuning and pump power are the decisive factors for comb generation. Figure 4 shows the numerical simulation results of the evolution process in the anomalous dispersion microresonator. It can be seen that when the detuning is small, the intracavity power is low, and the sideband cannot be excited. When the intracavity power is high enough, two sidebands will be excited by parametric gain, and more sidebands will be generated as the intracavity power is further increased, which is the primary comb state. With the further increase of the power in the cavity, the primary comb will further stimulate secondary comb teeth due to the four-wave mixing. As the secondary combs gradually become stronger, the optical comb teeth fill all the modes in a wide span. With the further increase of the detuning, the power in the cavity will decrease abruptly, and the optical field will gradually stabilize into a periodic pulse, which is called a soliton state. Due to the characteristics of solitons, multiple pulses can be supported in a single period.

Compared with the experimental results, the LLE comprehensively and precisely describes the evolution process of the microcomb in the time-frequency domain and has become the most commonly used equation in the study of microcavity nonlinear optics. The LLE can be solved by the split-step Fourier algorithm considering the periodic boundary conditions of microresonators, and other numerical solving methods like the Newton–Raphson solver^[121]. Additionally, for different platforms, various modified equations have been introduced to incorporate additional physical mechanisms, such as higher-order dispersion^[73], the thermal effect^[122], the Raman effect^[31], and the free carrier effect^[123]. These modifications further refine the accuracy of the simulations. By establishing explicit spatiotemporal models, researchers can gain deeper insight into the dynamic processes underlying microcomb generation, leading to a better understanding of this complex phenomenon.

2.3 Generation Method

The single-bright-soliton state is the required state for most applications. As predicted in theory, the experimental observation of the single-soliton states was changing due to the block of thermal-optical effects. Because of the material absorption, the intracavity optical field thermally shifts the cavity resonance as a result of thermal expansion and thermal change of the refractive index, namely, the thermal-optical effect. The generation of microcombs is usually based on a forward tuning process with the pump laser sweeping through the resonant peaks from the blue-detuning side to the red-detuning side, as depicted in Fig. 4 in the simulation. During the transition from high-power stochastic states to mode-locked states, the abrupt drop of intracavity power and consequent temperature reduction will cause the resonant peak to be blueshifted, which makes the detuning out of the soliton's existing range. This abrupt intracavity power drop leads to the self-end of the mode-locked soliton states^[124,125]. To address this problem, several experimental methods have been developed. In Table 2, we

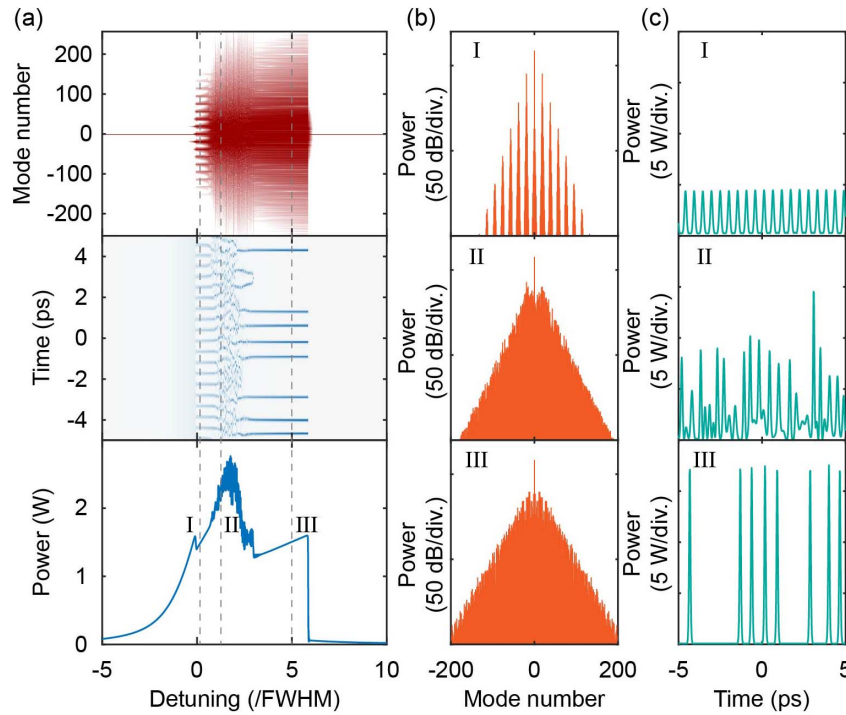


Fig. 4 Numerical simulation of the microcomb evolution. (a) The evolution process of intracavity optical spectra (top), pulse shapes (middle), and total powers (bottom). (b) Optical spectra under different states marked in (a). (c) Pulse shapes under different states marked in (a).

compare different excitation methods of mode-locked microcombs, including frequency sweeping^[125–127] and powering kicking^[124,128], pulse pumping^[66,129–131], auxiliary laser cooling^[132–136], integrated thermal tuning^[137], and self-injection locking^[86,138–142].

2.3.1 Frequency sweeping and optimized pumping

The response of the Kerr nonlinear effects can be considered to be approximately instantaneous. At the same time, the thermal effect is a relatively slow process, generally on the order of microseconds. The thermal-relaxation-induced transient instability is highly related to the detuning speed and the pump power. In the early research, the researchers mainly focused on optimizing the frequency sweeping strategies and pumping conditions for deterministically reaching mode-locked states with the thermal effect^[11], as shown in Fig. 5. The most straightforward method is the rapid sweeping, where the generation of soliton states is much faster than that of the thermal response.

To reach a fast sweeping, researchers propose the pump frequency sweeping based on a single-sideband modulator (SSBM)^[126,127], as shown in Fig. 5(a). By sweeping the applied frequency on the SSBM, the generated sideband features ultra-fast sweeping speed, even larger than 400 GHz/ μ s. It is worth noting that a fast-sweeping process results in short time windows where the soliton states exist. Thus, an optimal sweeping speed is required for the stable and easy access of the soliton states. As the detuning between the pump frequency and the resonant frequency is critical instead of the pump frequency, it is equivalent to tuning the resonant frequency. As depicted in Fig. 5(b), resistive heaters can be deposited above the microcavity to tune the resonance. By optimizing the applied voltage on the microheater, a soliton state can be generated^[137].

Except for the tuning of the detuning, it is feasible to access the mode-locked state with the tuning of pump power, known as the power kicking process^[124]. Firstly, the pump sweeps into the resonance at a high power level. Due to the thermal effect, the

Table 2 Summary of Different Excitation Methods of Mode-Locked Microcombs

Ref.	Method	Complexity	Integration level
[11,125–127]	Frequency sweeping	High	Low
[137]	Integrated thermal tuning	High	High
[124,128]	Power kicking	High	Low
[122]	Backward tuning	High	Low
[129–131]	Pulse Pump	High	Low
[132–136]	Auxiliary laser cooling	High	Low
[86]	Self-injection locking	Low	High

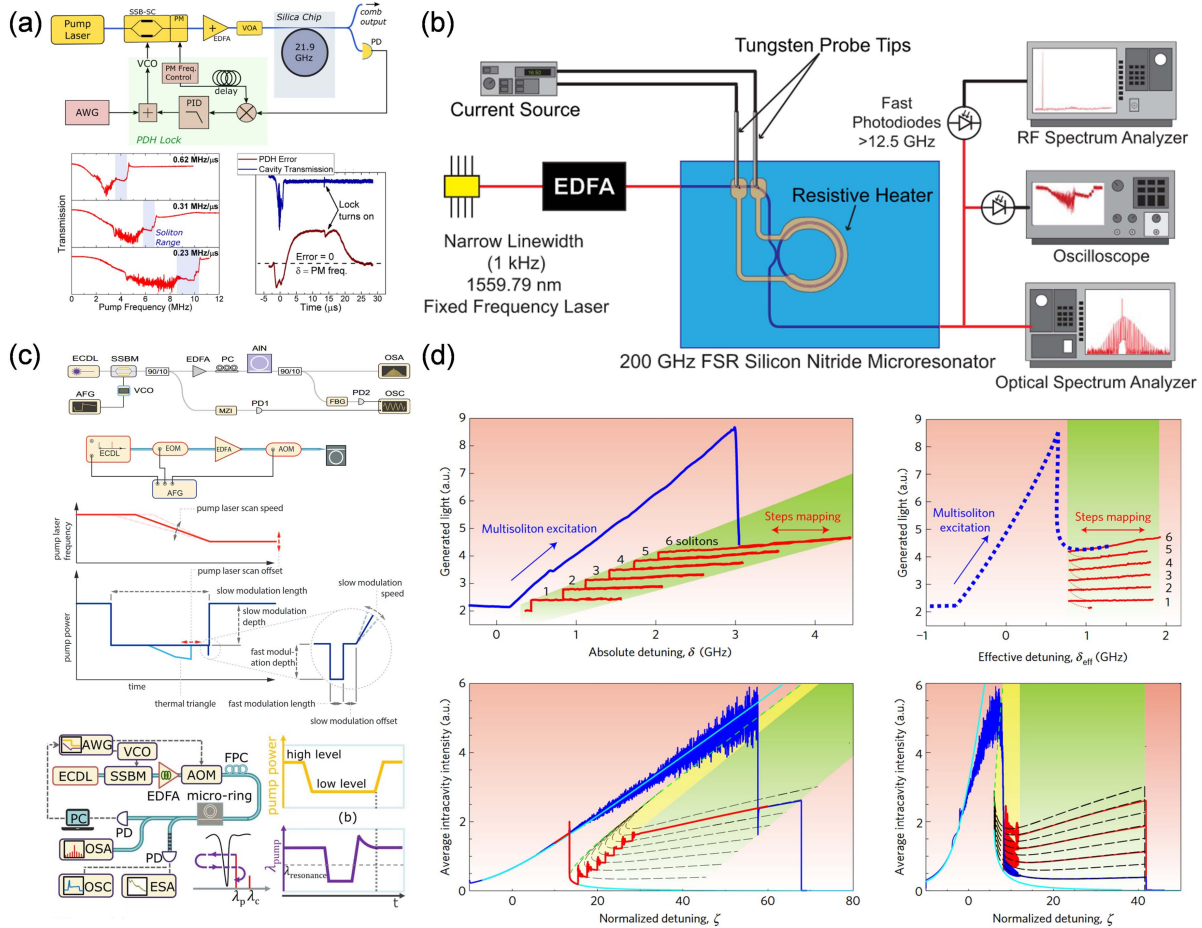


Fig. 5 Methods of frequency sweeping and pumping optimization. (a) Fast frequency scanning method^[127,137]. (b) Thermal tuning of the resonant frequency^[137]. (c) Power kicking method^[124,143]. (d) Bi-directional scanning method^[122].

system does not reach the soliton state at this detuning, while the soliton state exists with a lower pump power. Thus, the soliton state can be generated by abruptly decreasing the pump power. Meanwhile, the soliton existence range is relatively short at a low pump power. To increase the stability, the pump power abruptly increases again without losing the soliton state. The core of the power kicking process is the pump power tuning, which can be realized with an acoustic-optical modulator. In addition, the power kicking process can be combined with the rapid frequency tuning process^[143], as depicted in the lower panel of Fig. 5(c).

For the previous process, it is hard to determine the reached soliton state. In a pure anomalous dispersion cavity, the existence ranges of different soliton states overlap with each other, and the transition from a chaotic state leads to the uncertain reach of these soliton states^[11]. Meanwhile, in most cases, the single-soliton state is the required state. A backward sweeping method is proposed to solve this problem with the assistance of the thermal-optical effect^[122]. Considering the thermal effect, the existence range of a high-order soliton redshifts due to high state power. Thus, the steps of different soliton states do not overlap anymore at the blue (high-frequency or small wavelength) side. As illustrated in Fig. 5(d), the soliton order gradually decreases with a backward sweeping process and eventually reaches the single-soliton state.

Despite the stable access of soliton states, the above schemes require complex tuning processes and equipment, which is difficult to integrate with miniaturized microcomb systems.

2.3.2 Pulse pumping

The continuous wave (CW)-laser-driven DKSs in microresonators face several challenges related to conversion efficiency and the pump power thresholds, which limit their practical applications. The low conversion efficiency results from the small temporal overlap between the driving CW background and the ultrashort bright soliton pulse. For microcomb generation in a pulsed driving scheme^[129–131], a periodic driving pulse train replaces the CW laser, as illustrated in Fig. 6. The resonantly enhanced pulse supports a co-propagating soliton pulse, reducing the required driving power and the absorptive thermal effect. The pulse pumping configuration provides merits of reduction of pump power and improvement in efficiency, as well as deterministic and controlled generation of stable single or multiple DKSs. Also, the repetition rate and the CEO frequency of the generated microcomb are determined by the driving pulse, which reduces the timing jitter. However, the pulse repetition rate and the carrier-envelope frequency of the driving pulse train must match the resonance frequency to achieve coherent build-up. This intricate tuning process and the complex pulse

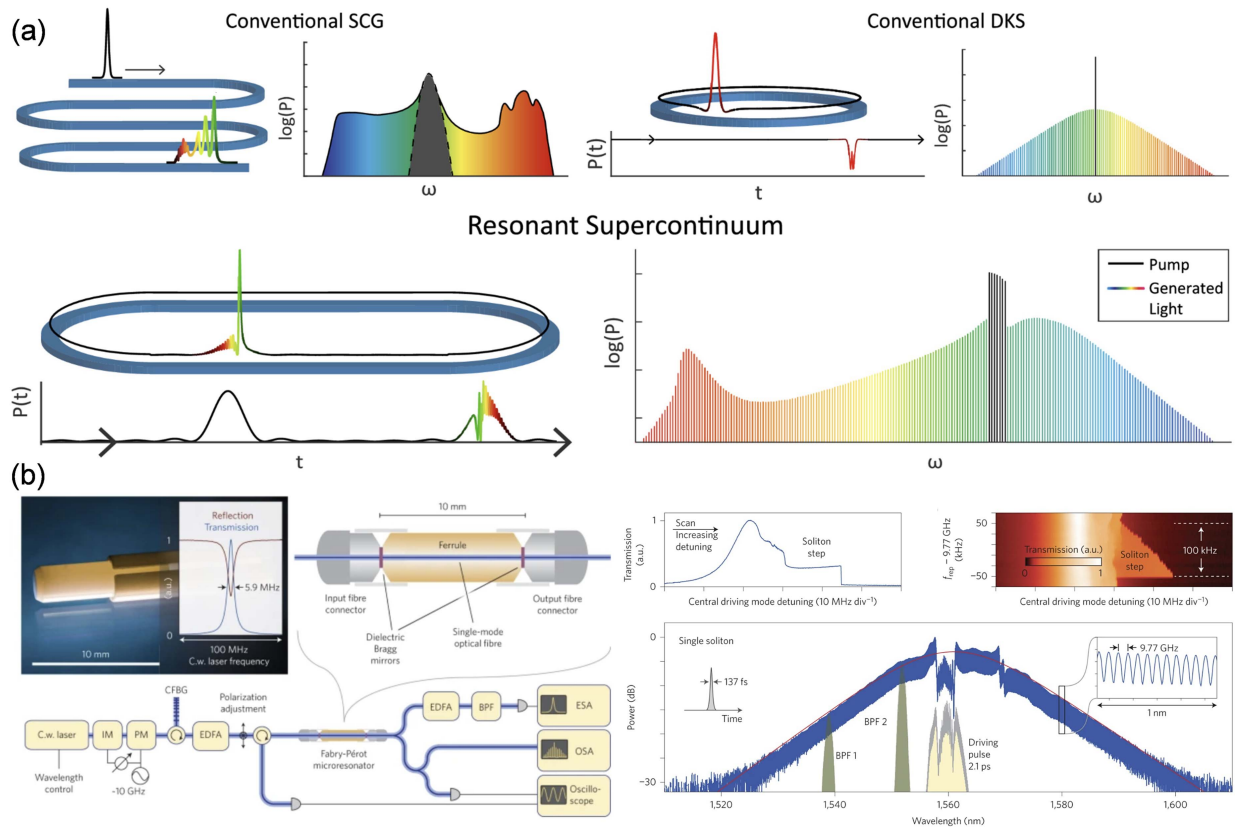


Fig. 6 Principle and experimental scheme of pulse pump method. (a) Concept and comparison of the pulse pumping with traditional methods^[129]. (b) Experimental setup, simulation results, and experimental results of pulse pumping microcombs^[129].

pump conditions make the setup challenging, which hinders its broader application.

2.3.3 Auxiliary laser cooling

Another stable arrival scheme for mode-locked microcombs is based on the idea of balancing the total intracavity power with an auxiliary laser, as shown in Fig. 7. According to different detailed mechanisms, different schemes such as “auxiliary mode”^[144], “auxiliary light”^[132,135], and “auxiliary sideband”^[134] are proposed. In this scheme, in addition to the pump laser, an auxiliary laser is required. During the tuning process, the auxiliary laser is first fixed on the blue detuning side of a resonant peak, and then the pump laser is scanned into the resonance^[135]. When the microcomb state supported by the pump laser is switched from a non-mode-locked state to a mode-locked state through scanning, the pump power in the cavity drops sharply, as mentioned above. The resonant peak near the auxiliary laser will blueshift as the pump power decreases. Thus, the auxiliary laser power in the cavity will increase to compensate for the total intracavity power change. By carefully setting the power and frequency of the auxiliary laser, simple mode-locked microcomb excitation can be achieved under a slow frequency sweeping process. In addition, the length of the soliton step will be significantly extended due to the cross-phase modulation effect of the auxiliary laser on the pump field^[133]. Recent studies have also revealed that the cavity with the auxiliary laser will exhibit an equivalent negative thermo-optical coefficient^[132], and direct mode-locked microcomb

excitation can be achieved with a backward tuning process^[136]. However, owing to the use of the auxiliary laser, this method has disadvantages in terms of device cost and overall system size.

2.3.4 Self-injection locking

In recent years, researchers have demonstrated turnkey microcomb excitation^[77] based on the self-injection locking effect^[145] by directly butt-coupling a semiconductor laser to a microresonator^[138], as depicted in Fig. 8(a). Traditionally, since the laser is sensitive to reflections, an optical isolator needs to be placed after the output of the laser. In the self-injection locking scheme, narrow-band reflections from high-quality-factor microcavities are utilized^[139] without the optical isolator. As the laser is directly connected with the high-quality-factor microcavity, the narrow-band reflection from the microcavity will lock the output frequency of the laser to the resonant peak of the microcavity, suppressing the frequency jitter of the laser. When the power and detuning of the laser are suitable, the mode-locked microcombs will be directly excited through the locking process. Firstly, this scheme is demonstrated based on the direct coupling between a laser diode and a bulk cavity, as depicted in Fig. 8(b). This locking process provides an integrated scheme for high-coherence optical sources, with integrated laser diodes and microcavities^[138], as shown in Fig. 8(c). Utilizing this scheme, single-chip and high-coherence mode-locked integrated microcombs can be realized with anomalous dispersion^[138] [see Fig. 8(d)] and normal dispersion^[140] [see Fig. 8(e)]. The basis of self-injection locking is the reflection or backscattering from

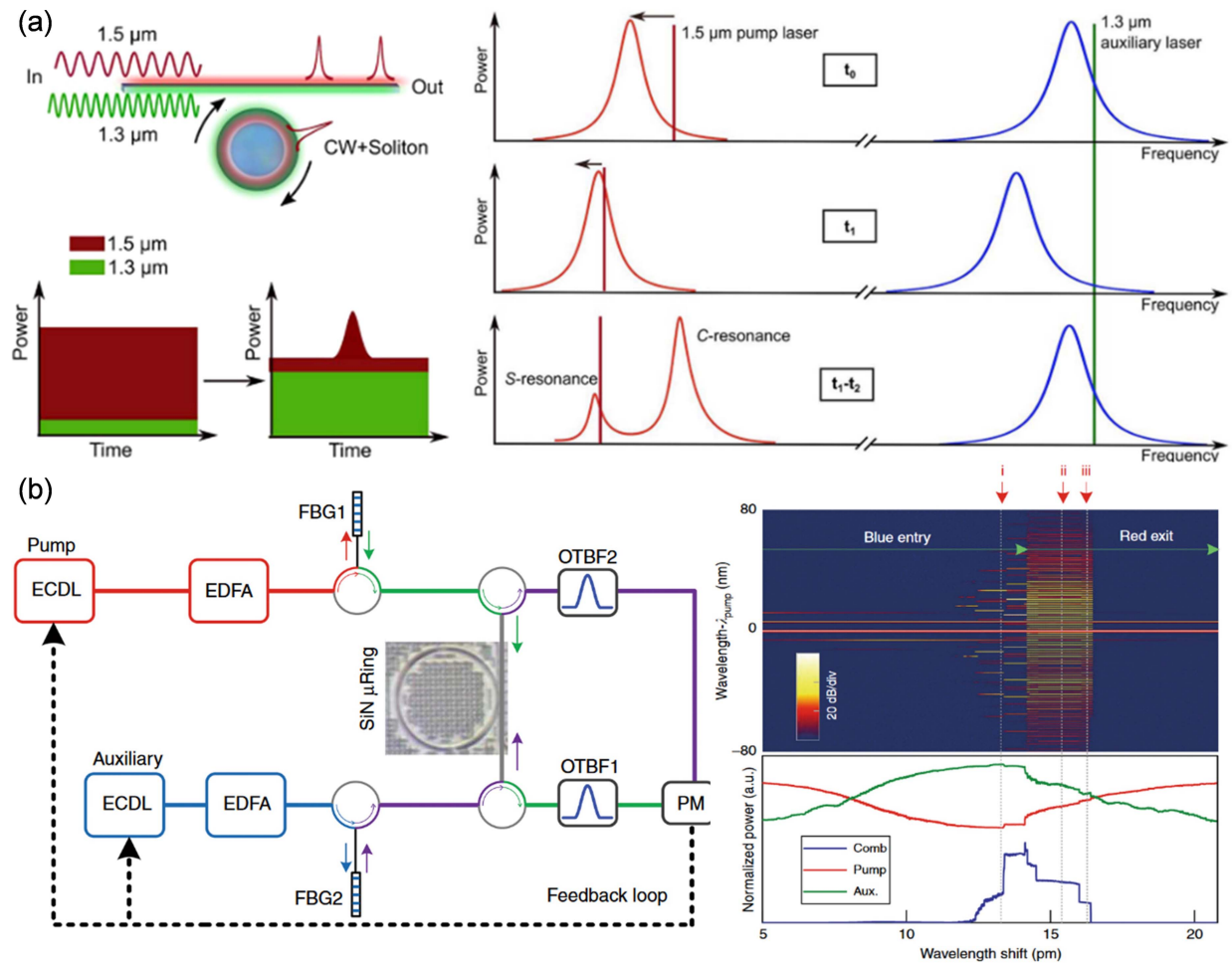


Fig. 7 Auxiliary laser cooling for soliton generation. (a) Concept and principle of the auxiliary cooling methods. (b) Experimental setup and simulation results of auxiliary laser thermal balance^[132,135].

a high-quality-factor microcavity. As shown in Fig. 8(f), the generated microcomb exhibits much better coherence compared with the free-running laser diode. The commonly used backscattering source is Rayleigh scattering^[139] in a high-quality-factor microcavity, which relies on random fabrication roughness and defects. The randomness can be solved by introducing controllable reflection structures^[142]. Although the turnkey operation and the integration are attractive, the spectral bandwidth is limited by the available pump power of integrated lasers. In addition, the generation relies on the preset of the system parameters, such as the feedback phase from the microcavity to the laser cavity. The sensitivity of the feedback phase raises concerns about the robustness of this scheme for real-world applications.

3 Materials and Integration

Since the first experimental observation of Kerr microcombs in silica microresonators^[70], various material platforms have been developed for microcomb generation, especially for chip-scale devices^[146]. This represents the convergence of materials science, optics, and engineering, offering the potential for a highly compact, portable, and fully integrated optical frequency comb. In the design and fabrication of integrated microcombs, the primary considerations are the optical properties of the materials

and the optical performance of the devices. These factors are mainly related to fundamental parameters such as optical nonlinearity, optical absorption, and refractive index. The optimization of the material formation and device design cannot be separated, and multiple factors must be considered, such as the on-chip integration of components and compatibility with nanofabrication processes. The selection of materials and the design of device structures are critical for the microcomb design, as they enhance energy efficiency, spectral bandwidth, coherence, and operational stability.

In this section, we will review the development in three subsections. The first reviews various material platforms developed over the past two decades for achieving high-quality microcavities and high-performance microcombs. The second introduces four typical fabrication processes for high- Q microcavities. The last subsection explores the packaging and integration techniques currently employed for miniaturized or integrated microcomb systems.

3.1 Materials and Functions

This subsection introduces the characteristics of various material platforms and compares them, as summarized in Fig. 9 and Table 3. Initially, silicon nitride and high-index-doped silica glass (Hydex glass), representative CMOS-compatible

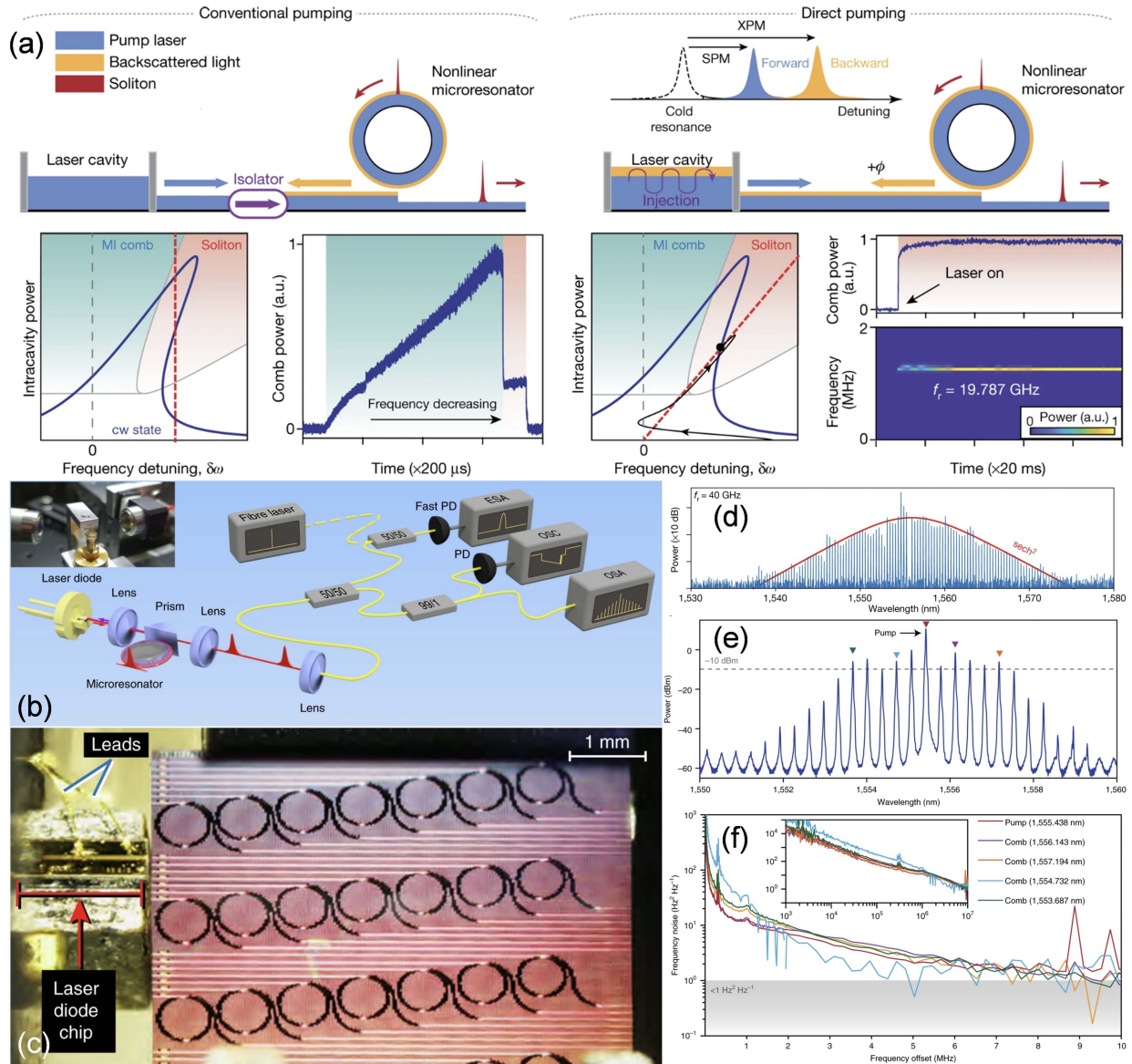


Fig. 8 Illustration of self-injection microcombs. (a) Concept and principle of self-injection locking and turnkey operation^[77]. (b) Self-injection locking of a laser diode to a bulk cavity for microcomb generation^[145]. (c) Self-injection locking of a laser diode chip to an integrated SiN microcavity chip for microcomb generation^[138]. (d) Bright soliton generated by self-injection locking^[86]. (e) The dark pulse is generated by self-injection locking^[140]. (f) Suppressed frequency noise^[140].

nonlinear platforms, were developed, demonstrating the potential for photonic integration. Subsequently, researchers have been motivated to expand beyond traditional integrated photonic materials to meet various application scenarios. One goal is to enhance or expand the nonlinear effects of devices in the commonly used bands to improve performance and efficiency. Another goal is to extend the span of microcombs to cover wider bands for various fields. Currently, microcombs have been generated on material platforms such as Si^[16], Si₃N₄^[17], metal fluorides^[14], AlGaAs^[21], LiNbO₃^[23], SiC^[25], AlN^[18], diamond^[19], Ta₂O₅^[20], and GaP^[84].

3.1.1 Metal fluoride

Metal fluoride crystal materials are highly suited for optical microcavity nonlinearities due to their broad transparent window,

low optical absorption loss, minimal dispersion, and excellent thermal and mechanical stability. For example, MgF₂ offers a wide transparent window ranging from ultraviolet (0.16 μm) to mid-infrared (7 μm), enabling the realization of high-quality factors ($Q > 10^8$) over a broad spectral range. This, combined with weak dispersion, makes MgF₂ ideal for multiband applications, such as octave-spanning tunable OPO^[151], nonlinear oscillation in visible bands^[172], and mid-infrared microcombs^[147]. High-quality MgF₂ microresonators, as shown in Fig. 10(a), also exhibit low-thermal-refractive-index constants, exceptional mechanical stability, and hardness^[173], all critical factors for creating stable microcomb systems. As shown in Fig. 10(d), with precise cavity design and system optimization, low-phase-noise Kerr combs can be generated. Notably, a micro-sized 10 GHz RF photonic oscillator^[44] has been demonstrated, which exhibits

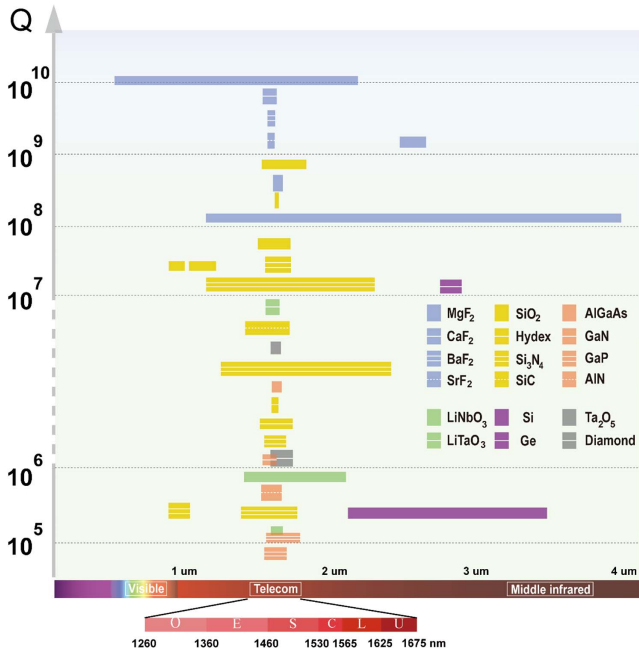


Fig. 9 Optical comb wavelength ranges and Q factors of different resonators based on various material platforms. Values of wavelength ranges and Q factors are taken from (top to bottom, left to right): MgF_2 ^[147], CaF_2 ^[148], BaF_2 ^[149], SrF_2 ^[150], MgF_2 ^[147], SiO_2 ^[70], MgF_2 ^[1], SiO_2 ^[135], MgF_2 ^[151], SiO_2 ^[117], SiO_2 ^[148], SiO_2 ^[148], Si_3N_4 ^[152], Si_3N_4 ^[153], Ge ^[88], LiTaO_3 ^[88], SiC ^[154], Ta_2O_5 ^[155], Si_3N_4 ^[156], AlGaAs ^[157], Hydrex ^[17], Hydrex ^[158], Si_3N_4 ^[122], GaN ^[19], diamond ^[19], LiNbO_3 ^[23], AlN ^[18], Si_3N_4 ^[159], Si_3N_4 ^[17], Si ^[160], LiNbO_3 ^[161], GaP ^[162], and GaP ^[162].

frequency stability (as measured by Allan deviation) several orders of magnitude higher than existing RF photonic devices with similar size, weight, and power consumption. In addition to MgF_2 , CaF_2 also has a broad transparent window (0.13–10 μm) and was among the first platforms used for microcomb generation^[148]. CaF_2 cavities, as shown in Fig. 10(b), have achieved a quality factor exceeding 2.5×10^9 and can generate microcombs of over 80 nm span with an input pump power of 50 mW. Similar ultrahigh- Q factors [above 10^9 , see Fig. 10(c)] have also been achieved based on BaF_2 ^[149] and SrF_2 ^[150].

While metal fluorides have significantly advanced the development of ultrahigh- Q microcavities, integrating these materials into chip-based platforms remains a challenge. Most demonstrated systems use bulk cavities, which require specialized and costly fabrication techniques, such as polishing and crystalline growth, making on-chip integration difficult. Nonetheless, their superior optical properties continue to drive innovation in high- Q resonators.

3.1.2 Silica

Since the early days of optics through to modern optical technologies, particularly fiber-based technologies, silicon dioxide (or silica) has played a pivotal role across all eras and applications. As shown in Table 3, despite its relatively low optical nonlinear coefficient^[177], silica enables nonlinear interactions at pump powers in the microwatt range with easily achieved quality factors exceeding 10^8 ^[70,135,174,176,177]. Since the first demonstration in 2007 of silica platforms generating microcombs with over 100 GHz repetition rates and wide spectral spans^[70], as

shown in Fig. 11(d), various microcavities have been employed for microcomb generation. Due to the ease of fabrication through the melting and solidification of silica, bulky microcavities such as microspheres^[175] and microrod cavities^[176] have been well-developed, as depicted in Figs. 11(b) and 11(c). A microrod cavity with an ultrahigh quality factor above 4×10^9 has been fabricated by irradiating silica microrods with CO_2 lasers, significantly decreasing the OPO threshold power to 110 μW ^[176].

Beyond bulk microcavities, several on-chip microcavities, such as silica wedge microresonators^[177] [shown in Fig. 11(f)] and microtoroids^[82] [shown in Fig. 11(a)], have been developed to expand applications and improve performance. In 2012, fabrication methods of silica wedge resonators compatible with traditional semiconductor processing processes were proposed^[177], with excellent control over the microcavity FSR and a record high Q of up to 8.75×10^8 . These silica-based wedge resonators show constant finesse over a wide range of diameters, supporting microcomb generation with the comb line spacing ranging from 2.6 to 220 GHz^[42,178]. With delicate design and fabrication of the wedge shape, broadband dispersion tuning can be realized^[179]. In addition, integrating high- Q silica microcavities with deposited Si_3N_4 bus waveguides on a single chip offers an alternative to traditional bulky prism or fiber coupling methods^[180].

3.1.3 Hydrex

High-index-doped silica glass (Hydrex) was developed as a CMOS-compatible optical platform and has been used for linear optics since the early 2000s^[181] and for nonlinear optics since 2008. The low optical loss, typically less than 0.1 dB/m, and negligible nonlinear loss, especially under high-intensity conditions ($>25 \text{ GW}/\text{cm}^2$)^[182], make it attractive for microcomb generation. In addition, Hydrex benefits from a mature fabrication process, including low-stress deposition, which facilitates the production of high-quality waveguides and resonators, as depicted in Fig. 12. Although its refractive index is low, the core-cladding contrast remains sufficient to allow for a minimum bending radius of 20 μm . Its Kerr coefficient^[183] of $1.15 \times 10^{19} \text{ m}^2 \text{ W}^{-1}$ is approximately five times that of silica. The Hydrex platform holds the potential for achieving more integrated and flexible applications of soliton microcombs. For example, in 2010, optical “superparameter” oscillation was achieved on the Hydrex platform with a quality factor of 1.2×10^6 , where the continuous wave threshold power was as low as 54 mW, and the frequency interval range was tunable from 200 GHz to over 6 THz^[158]. Soliton microcomb generation has been demonstrated in various regimes, including single-soliton, soliton crystal^[184], and laser soliton states^[76], highlighting the platform’s flexibility and robustness in supporting diverse comb dynamics.

3.1.4 Silicon nitride

Silicon nitride (SiN) is an exceptional platform for microcomb generation due to its low optical loss, wide transparency window, and favorable nonlinear properties^[183]. SiN waveguides can achieve ultra-low propagation losses, often below 0.1 dB/m, which is crucial for supporting high- Q resonators. These high- Q resonators enable efficient light confinement, facilitating the strong nonlinear interactions necessary for generating stable and coherent frequency combs. SiN also offers a broad transparency window, spanning from the visible ($\sim 400 \text{ nm}$) to the

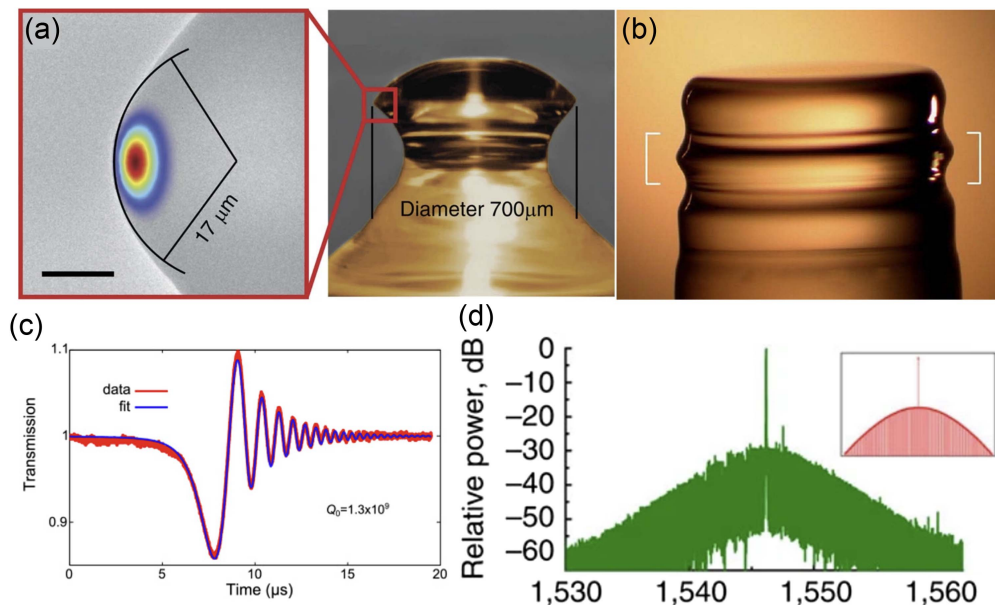
Table 3 Linear and Nonlinear Optical Properties of Various Materials for Nonlinear Photonics

Ref.	Material	Refractive Index	Kerr Coefficient ($10^{-19} \text{ m}^2 \text{ W}^{-1}$)	Transparency (μm)	CMOS Compatibility	Lowest OPO Threshold Power
[151]	MgF ₂	1.37	0.08	0.13–9	N	—
[154,25]	SiC	2.6	8	0.37–5.6	Y	8.5 mW
[163,164]	SiN	2	2.5	0–6.7	Y	73 μW @ 174 GHz
[70]	SiO ₂	1.45	0.3	0.2–4	Y	50 μW @ ~ 1 THz
[160]	Si	3.47	50	1.2–8	Y	3.1 mW @ 127 GHz
[165,166]	Ge	4.06	600	1.7–15	N	—
[17]	Hydex	1.7	1.15	0.29–7	Y	—
[148]	CaF ₂	1.43	0.12	0.13–10	N	—
[149]	BaF ₂	1.47	0.285	0.15–14	N	—
[150]	SrF ₂	1.43	0.176	0.15–12.5	N	—
[18,167]	AlN	2.12	2.3	0.2–13.6	N	25 mW @ 369 GHz
[168]	GaN	2.31	7.8	0.36–13.6	N	6.2 mW @ 330 GHz
[21,169]	AlGaAs	3.3	260	0.7–17	N	20 μW @ 1 THz
[84]	GaP	3.05	60	0.54–10.5	N	3 mW @ 100 GHz
[104]	LiNbO ₃	2.21	1.8	0.35–5	N	4.2 mW @ 200 GHz
[19]	Diamond	2.38	0.8	0.22–50	N	25 mW @ 925 GHz
[170]	Ge ₂₅ Sb ₁₀ S ₆₅	2.43	38	0.6–11	N	0.72 mW @ 1 THz

near-infrared ($\sim 4.6 \mu\text{m}$), making it versatile for applications in telecommunications, spectroscopy, and optical clocks. This broad transparency allows SiN to be used for frequency combs across multiple spectral bands, including the visible^[186] and telecom regions^[87]. SiN exhibits a relatively high Kerr nonlinear coefficient, which enhances four-wave mixing, the key mechanism for microcomb generation. The strong nonlinear response of

SiN enables comb generation at relatively low power levels, further enhancing its suitability for compact and energy-efficient photonic devices.

Nowadays, silicon nitride has emerged as a leading platform for microcomb generation, mainly due to the ultrahigh quality factors^[83,85], even close to the material limitation, with the standard planar fabrication process. As illustrated in Fig. 13, there


Fig. 10 Metal fluoride microcavities. (a) MgF₂^[147]. (b) CaF₂^[171]. (c) Q factor measurement of the BaF₂ cavity^[149]. (d) Generated bright soliton microcomb in a MgF₂ cavity^[44].

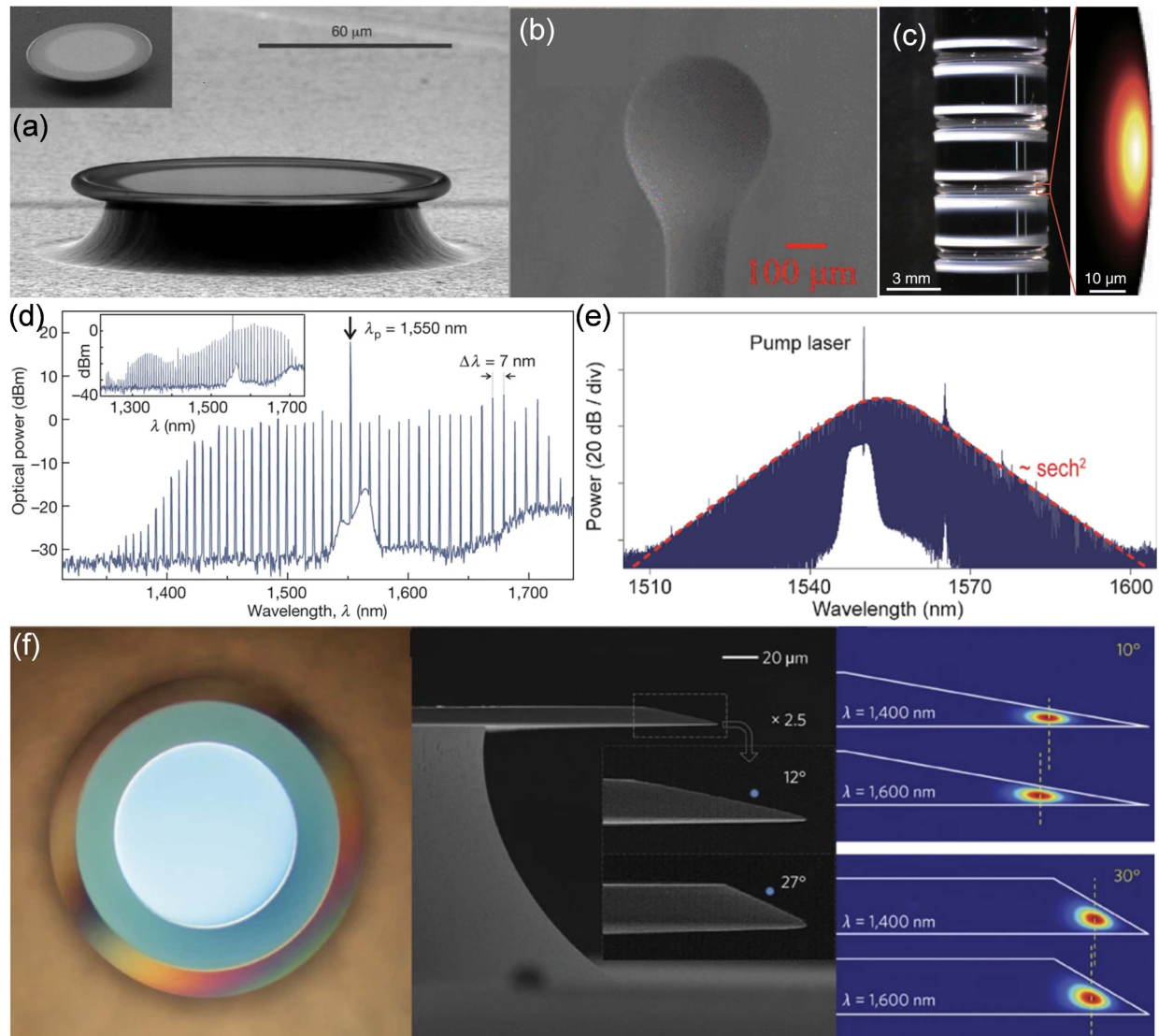


Fig. 11 Silica microcavities. (a) Silica toroid microcavity^[82]. (b) Wideband microcomb generated in silica microcavity^[70]. (c) Bright soliton microcomb generated in silica microcavity^[174]. (d) Silica microsphere cavity^[175]. (e) Silica microrod cavity^[176]. (f) Silica wedge microresonator^[177].

are two common types of integrated silicon nitride (SiN) platforms: thick and thin^[140] SiN platforms. The first is the thick silicon nitride platform, where the waveguide thickness needs to exceed 600 nm to achieve anomalous dispersion in the telecommunication band^[185], which is essential for generating bright soliton microcombs. However, during the fabrication of thick SiN films, stress accumulation at high temperatures often leads to film cracking. This issue can be addressed using the Damascene process^[83] or a multiple-deposition process^[187]. Both methods have successfully produced integrated microring resonators with quality factors higher than 10^7 . The second platform is the thin silicon nitride platform, with a typical waveguide thickness around 100 nm^[85]. By reducing the thickness, a more significant portion of the optical field is distributed into the silica cladding, which helps minimize the interaction between the optical field and the etched sidewalls, reducing scattering losses. This design has enabled the fabrication of integrated optical microcavities with quality factors^[140]

as high as 10^8 . The high quality factor achievable on both platforms has empowered researchers to explore various nonlinear optical phenomena and integrated microcavity optical comb technologies. These include photo-induced second-order nonlinear effects^[188,189], highly coherent light sources based on self-injection locking^[140], optical isolators using nonlinear phase shifts^[190], and the experimental observation of mode-locked microcombs^[11,72].

Although the silicon nitride (SiN) platform has achieved significant success and facilitated the study of various physical phenomena, the demanding fabrication conditions required for low-loss SiN waveguides limit its broader adoption. To achieve dense, high-quality SiN films with near-stoichiometric ratios, low-pressure chemical vapor deposition (LPCVD) is typically necessary. Additionally, the silica cladding surrounding the waveguides also requires LPCVD deposition^[85]. High-temperature annealing of the entire structure is essential to reduce hydrogens (mainly Si—H and N—H bonds) within the

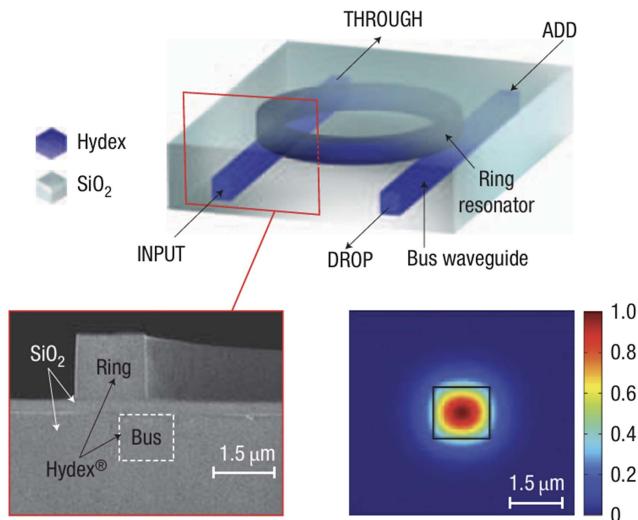


Fig. 12 Hydex microcavity^[15].

material and eliminate residues from the fabrication process, further lowering optical losses. However, these high-temperature fabrication conditions not only complicate the manufacturing process but also impose limitations on the integration of SiN with other material platforms. While plasma-enhanced chemical vapor deposition (PECVD) offers a faster and more cost-effective method for SiN film deposition^[191,192], it introduces higher intrinsic losses, primarily due to hydrogens formed during the deposition process. Efforts to reduce these losses have led to the development of post-deposition annealing techniques to minimize hydrogens. More recently, deposition methods such as

using deuterated silane (SiD_4) instead of silane (SiH_4) have been proposed to avoid hydrogen-related absorption in telecommunication bands^[193,194]. As a result, SiN fabrication is gradually shifting towards lower-temperature processes.

In the future, advancements in low-temperature deposition techniques for low-loss SiN waveguides, particularly those compatible with multiple material platforms, could pave the way for integrated, multifunctional systems based on microcombs. These improvements will expand the potential applications of SiN, enabling broader use in fields such as telecommunications, sensing, and quantum photonics.

3.1.5 Chalcogenides

With the great success of microcombs in the communication band, the extension into long wavelengths, such as the MIR^[147] bands, pushed the development of various platforms. Inspired by the chalcogenide glass fiber, integrated chalcogenide platforms are developed due to their high nonlinear optical properties and broad transparency window, particularly in the mid-infrared range^[22]. Chalcogenide glasses, composed of elements like sulfur, selenium, and tellurium, exhibit a much higher Kerr nonlinearity (χ^3) than silicon-based materials, which significantly enhances nonlinear effects for microcomb generation. This allows for efficient comb generation at lower power levels, making it ideal for power-sensitive and compact applications. One of the significant advantages of chalcogenide materials is their broad transparency range, which spans from the visible ($\sim 1 \mu\text{m}$) to the mid-infrared ($\sim 12 \mu\text{m}$). This makes chalcogenide platforms particularly attractive for mid-infrared frequency comb generation, opening opportunities in fields like spectroscopy, environmental sensing, and chemical detection, where molecular absorption lines lie within the mid-IR spectrum.

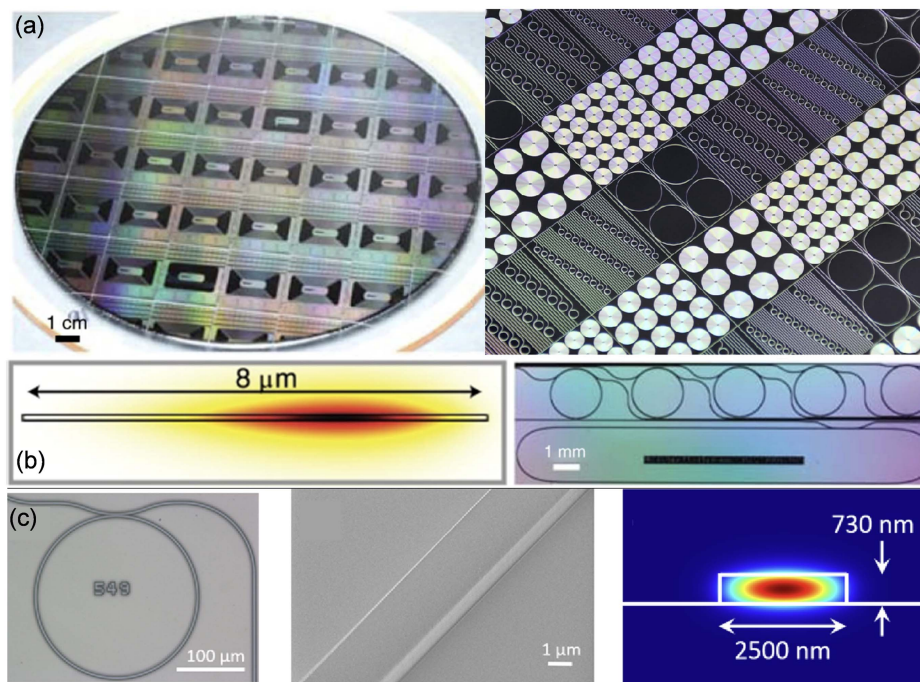


Fig. 13 Silicon nitride microcavity. (a) Massively produced silicon nitride chips^[87,140]. (b) Thin silicon nitride microcavity^[140]. (c) Thick silicon nitride microcavity^[185].

Chalcogenide waveguides can be fabricated with high-refractive-index contrast, enabling strong confinement of light and boosting nonlinear interactions. In addition, the easy fabrication process enables the integration with other integrated platforms, such as silicon^[196] and silica^[195], as depicted in Figs. 14(b) and 14(c). With the tuning of the material composition, mode-locked microcombs are observed in integrated chalcogenide microrings in telecom bands, under both anomalous and normal dispersion conditions^[170].

However, chalcogenide glasses face challenges such as higher optical losses compared to more mature platforms like silicon nitride, as well as susceptibility to environmental degradation like oxidation and moisture sensitivity. These factors can impact device longevity and performance, particularly in harsh operating environments. Nevertheless, with ongoing advances in fabrication techniques and protective coatings, the chalcogenide platform shows excellent potential for future microcomb applications, particularly in the mid-IR region, where other material platforms face absorption limitations.

3.1.6 Group IV semiconductors

With the development of electric chips, the silicon (Si) crystal is the purest crystal in the world. Thanks to the compatibility with the electrical chip fabrication process, namely, the CMOS compatibility, silicon photonics has been one of the most essential integrated photonic platforms. Silicon-on-insulator (SOI) structure is commonly used for silicon photonics^[198], where a top thin silicon layer is embedded on an oxide layer on the silicon substrate and another oxide layer deposited on the patterned structure. With the fabrication and design advancements, the quality factors above 10^7 are available from silicon photonics foundries^[199]. Despite the transparent window from 1.2 to

8 μm limiting its application for short wavelength bands and communication bands (1310 and 1550 nm) due to severe linear or nonlinear losses, the high Kerr nonlinear coefficient makes it a promising platform for microcomb generation in the mid-infrared^[160,200]. Microcomb generation has been demonstrated with the nonlinear absorption weakened with a reverse-bias PIN structure to shorten the free carrier lifetime^[123], as illustrated in Figs. 15(a) and 15(b). For the extension to a more extended wavelength band, the absorption of silica should be considered. Suspended silicon waveguides with the surrounding silica being removed are proposed for MIR range applications^[201].

Similar to silicon, other group IV semiconductors^[202], including the germanium (Ge)^[165,166] [see Fig. 15(c)] and the silicon-germanium alloy (SiGe)^[203,204], feature high Kerr nonlinear coefficients, suitable for nonlinear effects in the MIR band. Considering the absorption of silica, air cladding is preferred for low losses. Recently, as shown in Fig. 15(d), the ultrahigh Q of a 1.71×10^8 integrated platform consists of the SiGe core, and the Si cladding is proposed^[197], bringing novel integrated platforms for MIR nonlinear effects.

3.1.7 III–V compound semiconductors

The III–V semiconductor platforms, encompassing materials like gallium phosphide (GaP), aluminum gallium arsenide (AlGaAs), aluminum nitride (AlN), and gallium nitride (GaN), offer substantial promise for microcomb generation due to their high nonlinear optical coefficients and expansive transparency windows, along with strong second-order nonlinearity for self-referenced microcombs^[206]. These materials have distinct advantages that make them suitable for different spectral ranges and applications, particularly in the visible, near-infrared, and mid-infrared regions.

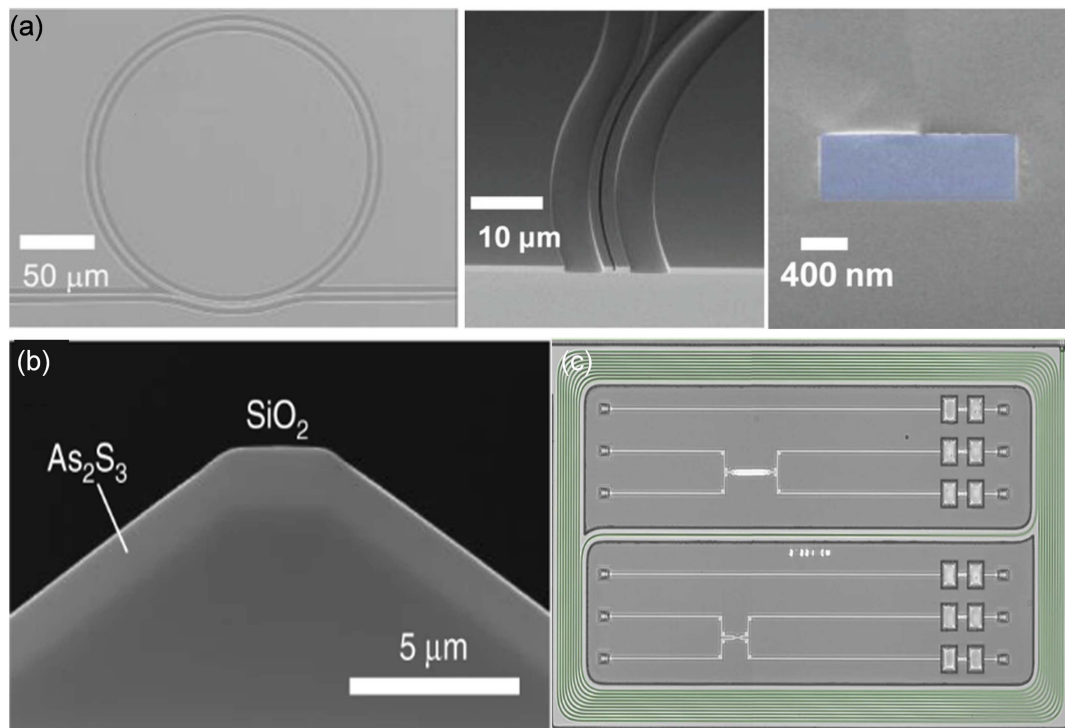


Fig. 14 Chalcogenide platforms. (a) Integrated chalcogenide microcavity^[170]. (b) Chalcogenide on silica^[195]. (c) Chalcogenide on silicon photonics^[196].

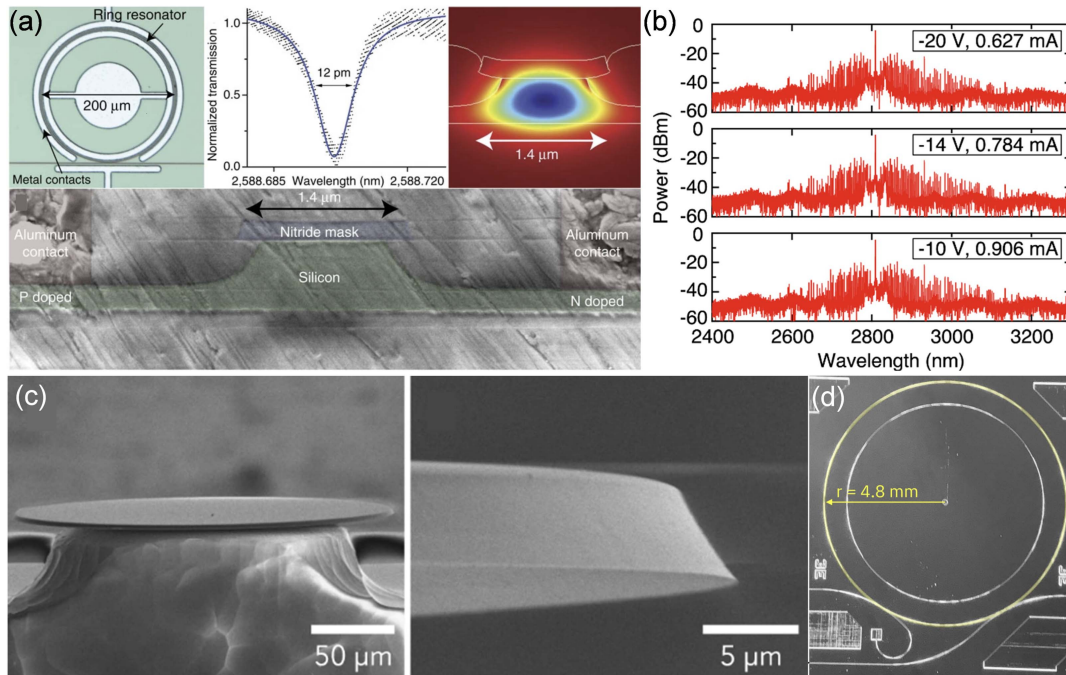


Fig. 15 Group IV semiconductor microcavities. (a) Silicon microring with PIN junction^[160]. (b) Mode-locked microcomb in silicon microrings^[123]. (c) High-quality germanium microcavity^[165]. (d) High-quality SiGe microring cavity^[197].

AlGaAs is a standout material for microcomb generation, particularly in the near-infrared range with the tuning of the material composition^[21]. It exhibits exceptionally high Kerr nonlinearity, two orders higher than that of silicon nitride, enabling efficient four-wave mixing for comb generation with ultra-low powers under moderate quality factors^[205]. Advanced fabrication processes, including the annealing process, the deposition of Al₂O₃ to reduce surface states, and integrated AlGaAs microrings with quality factors above 3×10^6 , have been demonstrated^[169,205]. Combining the high quality factor and the high Kerr coefficient, the OPO threshold down to 36 μ W and mode-locked microcomb generation with 930 μ W pump power are demonstrated^[157].

GaP is another promising material with high Kerr nonlinearity for low threshold power and a high index for tight light confinement, similar to AlGaAs. The cutoff wavelength of GaP is shorter, with the transparent windows ranging from 0.54 to 10.5 μ m, enabling the nonlinear effects from the visible bands. GaP does not suffer from nonlinear absorption loss in communication bands, making it efficient for microcomb generation.

AlN and GaN, known for their wide bandgaps, high thermal conductivity, and mechanical robustness, are excellent candidates for ultraviolet to near-infrared applications. AlN offers strong nonlinear properties like silicon nitride while being transparent over a broader spectrum from the UV to the infrared. GaN, similarly, is transparent across a wide range and has a relatively higher Kerr coefficient^[168]. In addition, the second-order nonlinearity of both materials makes it possible to realize microcomb generation and second-harmonic generation for a self-referenced frequency comb^[206]. For example, the cofunction of Kerr nonlinearity and second-order nonlinearity can excite microcombs at the telecom band and the visible band simultaneously^[115], as depicted in Fig. 16(e).

Despite their advantages, III–V semiconductors face challenges in complex fabrication processes, such as epitaxial growth and higher production costs than silicon-based platforms. However, their unique combination of strong nonlinearities, expansive transparency windows, and potential for integration with active devices like lasers and modulators makes them highly promising for advanced microcomb generation in diverse fields.

3.1.8 Electro-optical crystal

Compared to silicon nitride (SiN), lithium niobate [LiNbO₃, as depicted in Fig. 17(a)] offers similar optical properties, such as refractive index, Kerr nonlinear coefficient, and a broad transparent window suitable for Kerr microcomb generation. However, LiNbO₃ stands out due to its strong second-order nonlinearity, resulting from its non-centrosymmetric crystal structure^[23]. This feature allows for simultaneous microcomb generation and second-harmonic generation on a single chip, as depicted in Fig. 17(d). It is ideal for self-referenced microcombs—critical for producing stabilized optical frequency combs. Additionally, LiNbO₃ has a high electro-optic coefficient, which facilitates efficient interactions between optical and radio-frequency fields, as illustrated in Fig. 17(b). By applying a radio-frequency field with a frequency close to the FSR of the microcavity, the repetition rate of the generated microcomb can be locked, leveraging the interaction with the background fields^[207]. This provides precise control over the comb generation process. Moreover, the photorefractive effect of LiNbO₃ enables easier access to the bright soliton state, as depicted in Fig. 17(c). Unlike other platforms that require forward tuning, the bright soliton state in LiNbO₃ can be reached through a backward tuning process, simplifying the transition to this stable operational regime^[104].

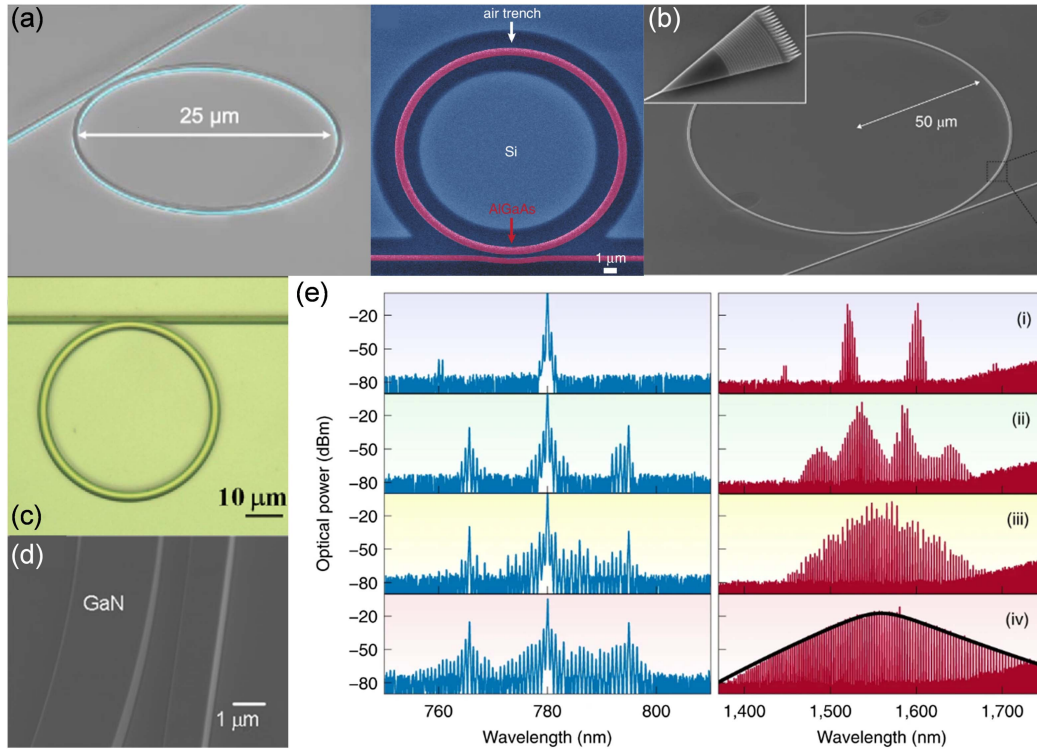


Fig. 16 III–V compound semiconductor platforms. (a) AlGaAsOI microcavities^[21,205]. (b) GaP microcavity. (c) AlN microcavity. (d) GaN microcavity^[168]. (e) Comb generation with the second-order nonlinearity in AlN^[115].

However, one drawback of LiNbO₃ of x-cut films, commonly used for electro-optic modulation, is its anisotropy. This anisotropy degenerates fabrication and induces inter-mode coupling, which can hinder microcomb generation. Recently, lithium tantalate^[88] [LiTaO₃, as shown in Fig. 17(e)], another electro-optic crystal with similar performance but weaker anisotropy, has been developed. As shown in the measured dispersion profiles in Fig. 17(f), the LiTaO₃ microcavity exhibits a smooth dispersion profile, indicating weak inter-mode coupling. With intrinsic quality factors up to 10⁷, soliton microcomb generation has already been demonstrated in LiTaO₃, positioning it as a promising alternative to LiNbO₃ for specific applications.

3.1.9 Other platforms

Except for the aforementioned material, other platforms, especially integrated platforms are also developed for different applications, such as diamond^[19], SiC^[25], and Ta₂O₅^[155].

Diamond was first proposed as a platform for OPO oscillation comb generation in 2014^[19]. It has a relatively high refractive index (2.38) and an ultra-wide transparent window (0.22–50 μm). Diamond exhibits a significant Kerr nonlinearity ($0.8 \times 10^{-19} \text{ m}^2 \text{ W}^{-1}$) in the communication band, and its large bandgap of 5.5 eV ensures immunity from TPA not only in the near-infrared but also in the visible range^[208]. Its high thermal conductivity and low thermo-optic coefficient provide high-power handling capabilities, resulting in temperature stability of microcombs across a wide wavelength range. Diamond offers unique opportunities to integrate nonlinear photonics with quantum optics, potentially merging quantum information

science^[209,210] with classical optical information processing on a single chip.

Similar to diamond, silicon carbide (SiC) has garnered significant attention due to its excellent material properties for quantum information science^[211]. Recent reports have demonstrated that 4H-silicon-carbide-on-insulator (4H-SiCOI) can achieve a quality factor Q ^[154] as high as 6.75×10^6 , and a mode-locked microcomb generation has been reported. The formation process of microcombs was observed in the quantum aspect of this platform^[79].

Recently, CMOS-compatible materials have been well-developed for microcomb generation, except for silicon and silicon nitride. One of the most successful integrated platforms is tantalum pentoxide^[155] (Ta₂O₅). It exhibits low intrinsic material stress, low optical loss, and effective Kerr nonlinearity^[155]. It has achieved quality factors as high as 3.8×10^6 and residual tensile stress of only 38 MPa. Due to its low-temperature deposition and processing requirements, Ta₂O₅ offers extensive opportunities for low-loss nonlinear photonics and heterogeneous integration.

3.2 Fabrication of High-Quality-Factor Microcavities

High- Q microcavity fabrication is essential for achieving high-performance microcombs. In this subsection, four typical fabrication processes for different types of microcavities are introduced. The first method is the fabrication of crystalline microcavities, which involves cutting and polishing^[212]. Crystals or glass materials are cut into specific shapes and then polished to achieve atomically smooth surfaces, minimizing optical scattering losses and enabling high Q factors. The second method is

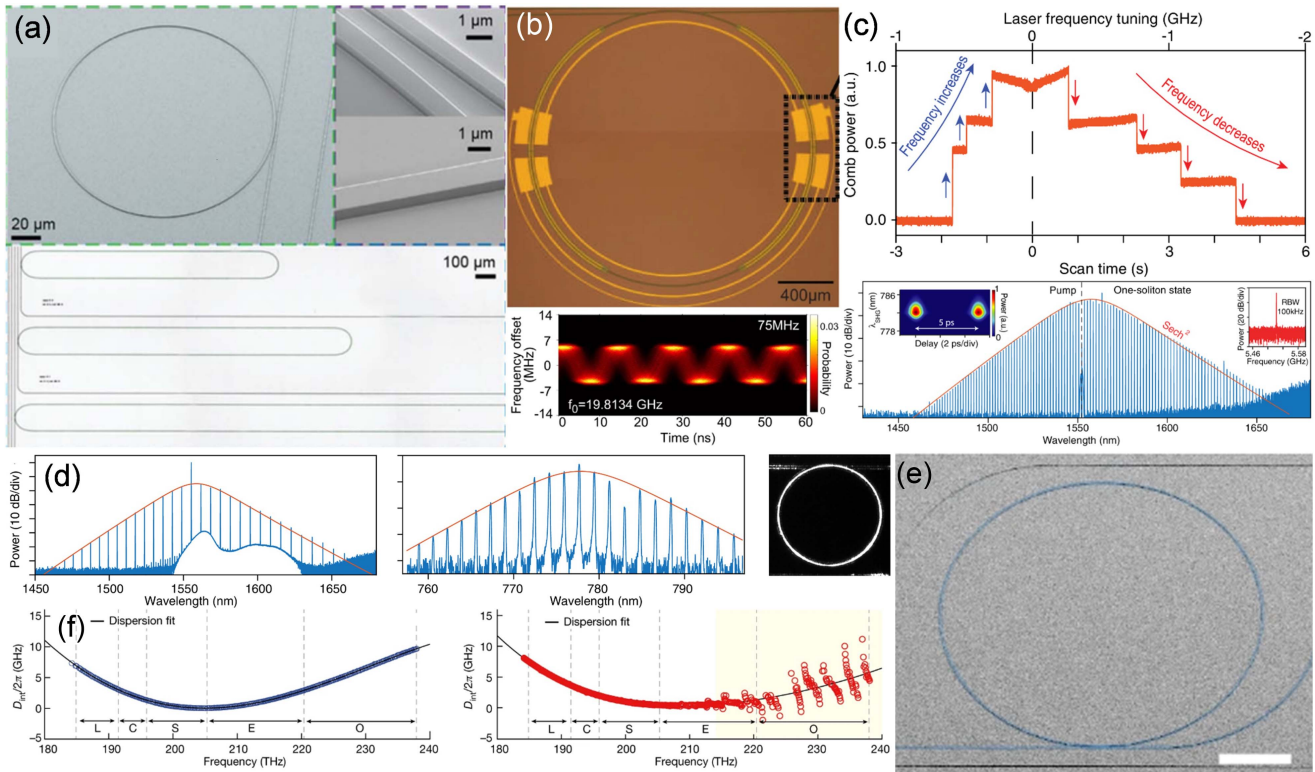


Fig. 17 Electro-optical crystal platforms. (a) LiNbO₃ microcavities^[23]. (b) LiNbO₃ microcavity with electrodes (top) and the tuned repetition rate of the generated microcomb with the applied microwave field (bottom)^[207]. (c) Self-starting solitons in LiNbO₃ microcavities^[104]. (d) Visible comb generation in LiNbO₃ microcavities with the second-order nonlinearity^[104]. (e) LiTaO₃ microcavities^[88]. (f) Comparison of the dispersion profiles of LiNbO₃ (right) and LiTaO₃ (left) microcavities^[88].

melting and solidification techniques^[213], such as laser reflow. In this process, materials like silica are locally heated until they melt and are then allowed to solidify, resulting in ultra-smooth surfaces through the natural smoothing effect of surface tension, thus reducing optical losses. The third method is the monolithic process, where films are directly deposited onto a substrate for subsequent processing. Silicon nitride fabrication^[187,214] is an example, which involves deposition, lithography, and etching steps to form microcavities on the substrate. The final method is the bonding process, where pre-prepared films are transferred onto a target chip for further patterning. The fabrication of AlGaAsOI^[169] is an example, where the film is bonded and patterned to create high- Q microcavities. Each of these methods provides distinct advantages in terms of material compatibility, scalability, and integration, contributing to the diverse landscape of high- Q microcavity fabrication.

3.2.1 Cutting and polishing

Since the inception of microcavity-based research, crystalline microcavities^[218,219] have been pivotal due to their ultrahigh quality factors^[212] (Q factors) and broad transparent windows, as discussed earlier. The initial step in the fabrication process involves cutting the bulk crystal into rough shapes^[215], as illustrated in Fig. 18(a), a procedure that must be performed with high precision to avoid introducing defects. This is typically done using diamond tools^[216] [see Fig. 18(b)] or other high-precision cutting tools, which allow for clean and controlled cuts. Following this,

the crystals undergo a meticulous polishing phase, which is crucial for achieving the atomic-level smoothness required for high- Q microcavities^[217], as depicted in Fig. 18(c). This process can involve a combination of mechanical and chemical polishing techniques. Mechanical polishing uses abrasives to

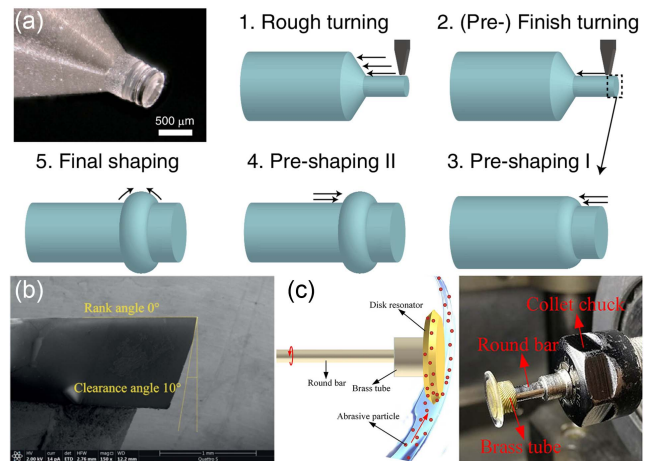


Fig. 18 Fabrication process of crystalline microcavities. (a) Cutting and shaping process^[215]. (b) The photo of a diamond tool^[216]. (c) Polishing with abrasive particles^[217].

progressively refine the surface, while chemical polishing may involve etching agents that help remove any residual surface imperfections. To further enhance surface quality, thermal annealing^[212] can be employed. This technique involves heating the polished microcavity to relieve internal stresses and further smooth out any microscopic imperfections that might remain, ensuring that the surface is ideally suited for optical applications.

Overall, the fabrication of crystalline microcavities requires a high degree of precision and control at every stage^[173]. Each step—from material selection and cutting to polishing, shaping, and coupling—plays a significant role in determining the final performance of the microcavity^[173,215].

3.2.2 Melting and solidification

Different from crystalline materials, where the fabrication process involves precise and complex mechanical processes, the fabrication of amorphous microcavities is relatively handy with the melting and solidification process, usually realized with high-power lasers^[220]. A typical one is silica. In the following, the fabrication processes of two typical microcavities, the microsphere^[221] and the microtoroid^[70] cavities, are introduced.

1) Fabrication process of microsphere cavity

Microsphere cavities are among the simplest yet most effective types of high- Q resonators^[221]. These spherical structures are usually fabricated from glass materials such as silica (SiO_2) due to their low optical absorption and high transparency over a broad wavelength range. The primary method for creating microsphere cavities involves a melting and solidification process, which is relatively straightforward but highly effective in yielding ultra-smooth surfaces, as illustrated in Fig. 19(a).

The fabrication process begins with a small glass fiber, typically silica, which is heated using a focused CO_2 laser beam. This laser precisely melts the tip of the fiber, causing it to form a spherical shape through surface tension as the glass reflows. The melting process can also be realized with a microheater^[222] or arc discharge of a fiber fusion splicer^[223]. The molten glass naturally minimizes surface imperfections, resulting in an exceptionally smooth surface critical for high- Q operation. As the melted glass cools and solidifies, a nearly perfect spherical shape is achieved with minimal optical scattering losses. This process ensures high precision and repeatability in forming microspheres with diameters ranging from a few microns to several hundred microns.

One key advantage of microsphere cavities is the absence of complex lithography or etching steps, making them a

cost-effective option for generating high- Q resonators. The smooth surface achieved through the melting process ensures minimal optical losses, which is crucial for applications requiring high light confinement. However, controlling the exact size and shape of the microsphere can be challenging, and additional care must be taken during the heating and reflow process to avoid asymmetries.

2) Fabrication process of microtoroid cavity

Microtoroid cavities^[82], on the other hand, represent a more sophisticated type of resonator that combines high- Q performance with a compact and planar form factor, making them more suitable for integration into photonic circuits. The fabrication of microtoroid cavities typically follows a multistep process that involves lithography, etching, and laser reflow techniques^[213], as shown in Fig. 19(b).

The fabrication process of microtoroid cavities begins with a planar substrate, usually silicon coated with a thermally grown silica layer. The first step involves using standard photolithography to define the toroidal shape of the silica layer. A photoresist is applied and patterned using UV light to create a mask for the subsequent etching process. Once the pattern is transferred, reactive ion etching (RIE) is used to etch away the exposed silica, forming a cylindrical pedestal structure. The dimensions of the toroid are defined during this step, including the height and width of the resonator.

Following the etching process, a CO_2 laser is used to selectively reflow the edges of the silica pedestal, converting the sharp, cylindrical profile into a smooth toroidal shape. The high heat from the CO_2 laser locally melts the silica, and as with microspheres, surface tension helps smooth out any rough edges or imperfections. The reflow process is critical for achieving the ultra-smooth surfaces necessary for minimizing optical scattering losses. By controlling the laser power and duration, the size and quality of the microtoroid can be fine-tuned. The final structure resembles a doughnut-shaped ring, with light tightly confined around the central axis of the toroid.

Microtoroid cavities offer several advantages over microspheres, particularly in terms of integration with other photonic components. Their planar geometry allows them to be fabricated directly on-chip, making them ideal for applications that require compact, integrated photonic circuits. Additionally, the precise control over the resonator dimensions provided by the lithographic process enables the fabrication of microtoroids with highly uniform characteristics, which is beneficial for scaling up production^[224].

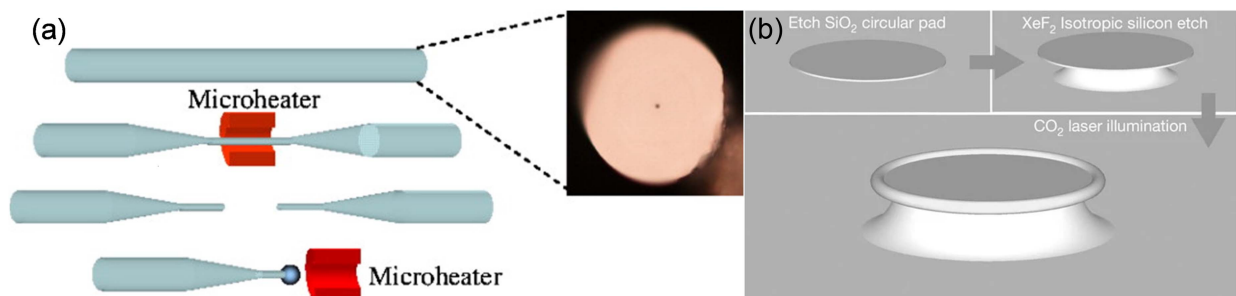


Fig. 19 Melting and solidification processes. (a) The fabrication process of microtoroid cavity^[82]. (b) Preparation process of microsphere cavities^[222].

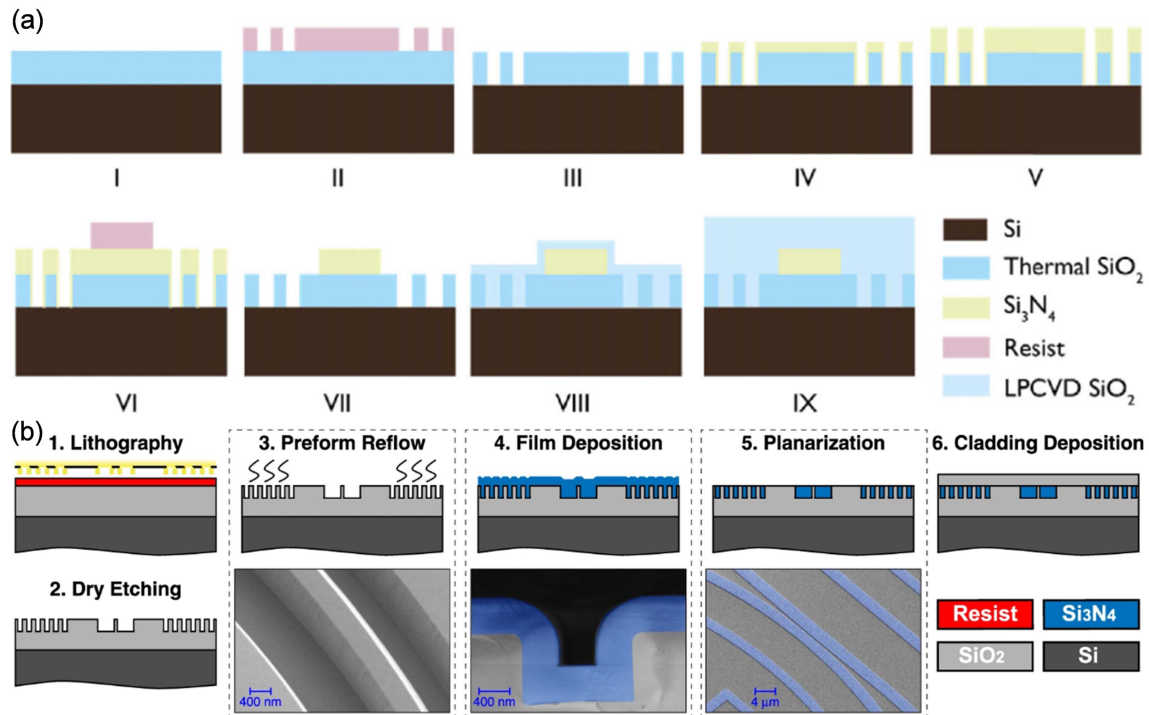


Fig. 20 Fabrication processes of thick silicon nitride microcavities. (a) The subtractive process^[187]. (b) The Damascene process^[214].

3.2.3 Monolithic process

In integrated photonic platforms, it is often more practical to directly deposit the required material onto a substrate, a process known as monolithic integration. For the platforms mentioned earlier, materials such as silicon nitride^[87], Hydrex^[183], silica^[82], chalcogenide^[22], and silicon^[16] can be directly deposited on silica, while materials like AlN^[18] and GaN^[168] can be deposited on sapphire. An example is the fabrication of thick silicon nitride^[225], where managing stress accumulation at high temperatures is a significant challenge. This issue can be addressed using the Damascene process^[83] or a multiple deposition process^[187].

1) The Damascene process

The Damascene process, initially developed for the microelectronics industry, has been adapted for high- Q photonic device fabrication. It involves patterning and filling trenches in a substrate with SiN, followed by a planarization step to achieve the desired waveguide and cavity structure, as shown in Fig. 20(a). This technique is especially well-suited for fabricating waveguides with minimal surface roughness and ultra-smooth sidewalls, which are crucial for reducing optical losses in microcavities.

The Damascene process begins with the deposition of a sacrificial layer, usually silicon dioxide (SiO₂), onto a substrate, typically silicon. Photolithography is then used to define the pattern of the waveguide or resonator in the SiO₂ layer, which is subsequently etched to create trenches. The SiN material is deposited into these trenches via chemical vapor deposition (CVD). One of the key advantages of this process is that it allows for the deposition of thick SiN layers, which is important for avoiding issues related to thin-film cracking and stress during high-temperature processing. After the SiN is deposited into

the trenches, the surface is polished using chemical mechanical polishing (CMP) to achieve a planar surface. This step is critical for removing excess SiN and ensuring that the surface of the waveguide or cavity is as smooth as possible. The planarization process helps to minimize surface roughness and defects, which are major sources of scattering loss in optical microcavities.

The Damascene process offers several advantages, including the ability to create thick waveguides with minimal stress, excellent control over geometry, and smooth sidewalls that are essential for maintaining low optical losses. The high degree of process control also allows for the fabrication of complex structures, such as microresonators and integrated photonic circuits. However, the process can be time-consuming and requires several fabrication steps, including the deposition, etching, and polishing of multiple layers.

2) The subtractive process

The subtractive process, in contrast, involves the deposition of a uniform SiN layer over the entire substrate, followed by patterning and etching to define the microcavity structure, as shown in Fig. 20(b). This method is simpler and more widely used than the Damascene process, particularly in research laboratories, due to its straightforward implementation and adaptability.

The subtractive process typically begins with the deposition of a SiN film on a silicon dioxide substrate. LPCVD is commonly used for this purpose, as it produces high-quality SiN films with low intrinsic losses. The thickness of the SiN layer is carefully controlled, as it plays a critical role in determining the optical confinement and the mode properties of the resulting microcavity. It is worth noting that for thick SiN layer deposition, two-step deposition is applied with crack barriers and a thermal cycling process to avoid the film cracking.

Once the SiN layer is deposited, photolithography is employed to define the desired pattern of the microcavity. The patterned photoresist serves as a mask for the subsequent etching step. Reactive ion etching (RIE) is then used to remove the excess SiN, leaving behind the microcavity structure. The quality of the sidewalls formed during the etching process is crucial for minimizing scattering losses. In some cases, additional surface treatment steps, such as thermal annealing, are used to further smooth the etched sidewalls and improve the optical performance of the cavity.

The subtractive process offers several advantages, including simplicity and scalability. It allows for the fabrication of a wide range of SiN-based photonic devices, including ring resonators, waveguides, and photonic crystal structures. Additionally, this process is well-suited for integration with other materials and components, making it a versatile option for creating complex photonic circuits. However, the subtractive process has some limitations, particularly in terms of sidewall roughness and material stress. Since the SiN layer is deposited as a continuous film before patterning, it can develop stress during deposition, which may lead to cracking or warping, especially for thicker films. Moreover, the etching process can introduce sidewall roughness, which increases optical scattering and degrades the Q factor of the microcavity.

3.2.4 Bonding process

Due to lattice mismatch, it is often challenging to directly deposit high-quality films on substrates made of different materials. Bonding processes have been developed to overcome this issue in integrated devices. Among the integrated platforms that rely on bonding, LNOI^[23] and AlGaAsOI^[21,157,169] are two prominent examples. In this subsection, the fabrication process of AlGaAsOI serves as a representative case for understanding the role of bonding in creating high-performance photonic devices.

As shown in Fig. 21, the fabrication of AlGaAsOI microcavities^[21,157,169] begins with the preparation of high-quality AlGaAs epitaxial layers on a GaAs (gallium arsenide) substrate. These

epitaxial layers are grown using molecular beam epitaxy (MBE) or metal-organic chemical vapor deposition (MOCVD), ensuring precise control over layer thickness and material composition. The high crystalline quality of the AlGaAs film is crucial for achieving low optical losses in the final microcavity. Once the AlGaAs layer is prepared, it is transferred onto a silicon dioxide (SiO₂) insulator layer, typically on a silicon wafer, through a process called wafer bonding. The bonding process involves bringing the AlGaAs/GaAs wafer into contact with the target SiO₂/Si substrate and applying thermal treatment or pressure to achieve a strong, permanent bond. This step is critical for creating the AlGaAsOI structure, which combines the advantageous properties of AlGaAs with the thermal and mechanical stability of the insulator platform. After bonding, the original GaAs substrate is removed through selective etching, leaving only the AlGaAs layer on the insulator. This step can be achieved using a chemical etching process that selectively removes GaAs without damaging the AlGaAs layer. Once the AlGaAsOI structure is prepared, the microcavity patterning process begins. Photolithography is used to define the microcavity design, such as microring or disk resonators, on the AlGaAs surface. After patterning, reactive ion etching (RIE) is employed to create the desired structures with high precision. This etching process is carefully controlled to achieve smooth sidewalls, which are essential for minimizing optical scattering losses and maximizing the Q factor of the resonator. Finally, the fabricated microcavities are often subjected to thermal annealing, which helps to further reduce surface imperfections and enhance the optical performance of the device.

3.3 Packaging and Integration

Microcombs have made significant advancements in generation methods and materials development, but most still rely on bulky pump lasers^[122,144,153]. Achieving fully on-chip microcombs is crucial for massive production^[146]. The operation of microcombs requires complex startup and feedback protocols, which demand optical devices that are hard to integrate and electrical

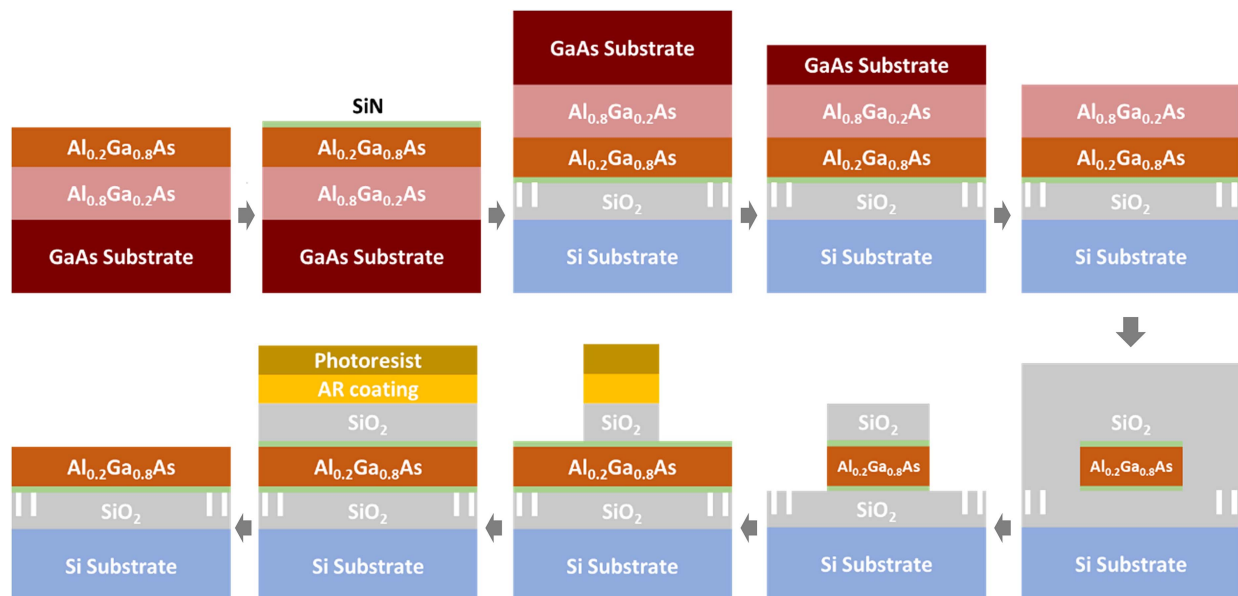


Fig. 21 Fabrication processes of AlGaAsOI microcavities^[21,157,169,205].

components. While integrated Si_3N_4 can achieve ultrahigh Q factors^[214], enabling highly efficient microcomb generation with the low pump power^[229], the lattice mismatch with III–V materials poses a significant challenge for a fully integrated schematic^[230]. Fortunately, hybrid integration or heterogenous integration approaches^[231] have been proposed for chip-level microcomb systems, as listed in Table 4.

One feasible approach to miniaturizing microcomb modules is co-packaging the pump laser chip and the microcavity chip^[77]. In 2015, the direct coupling of a laser diode with a bulk microcavity was demonstrated with prism-coupling for microcomb generation^[44]. This system relied heavily on numerous bulk devices due to the limited performance of integrated components at that time^[71]. At the same time, this scheme provides early proof of concept for fully integrated systems. In 2018, researchers introduced a chip-level microcomb generator by directly butt-coupling a semiconductor optical amplifier (SOA) chip with a silicon nitride microresonator^[62], as depicted in Fig. 22(a). The SOA, combined with mode-selection and reflection devices on SiN chips, formed an external cavity laser,

which pumped the high- Q microring to generate the microcomb. In 2019, the direct coupling of a laser diode chip with a microcavity chip was proposed for microcomb generation through self-injection locking^[138]. Then, the turnkey operation was demonstrated with this scheme^[77]. Although butt-coupling appears simple, this process requires precise alignment between the two integrated waveguides with micrometer-level feature sizes^[232]. Any misalignment can lead to significant insertion loss, severely hindering microcomb generation. To address these challenges, different optical packaging technologies have been developed. One example is the microlens-assisted coupling scheme^[233–235], designed to match the optical modes of the laser chip and the microring chip. More recently, photonic wire bonding^[236,237] has been proposed for coupling between different platforms. Similar to electrical wire bonding, an optical waveguide is fabricated between the chips, with connection ports tailored to each platform. This method provides a reliable solution for inter-chip coupling. Using this packaging approach, chip-level external cavity lasers have been realized and employed for microcomb generation^[226].

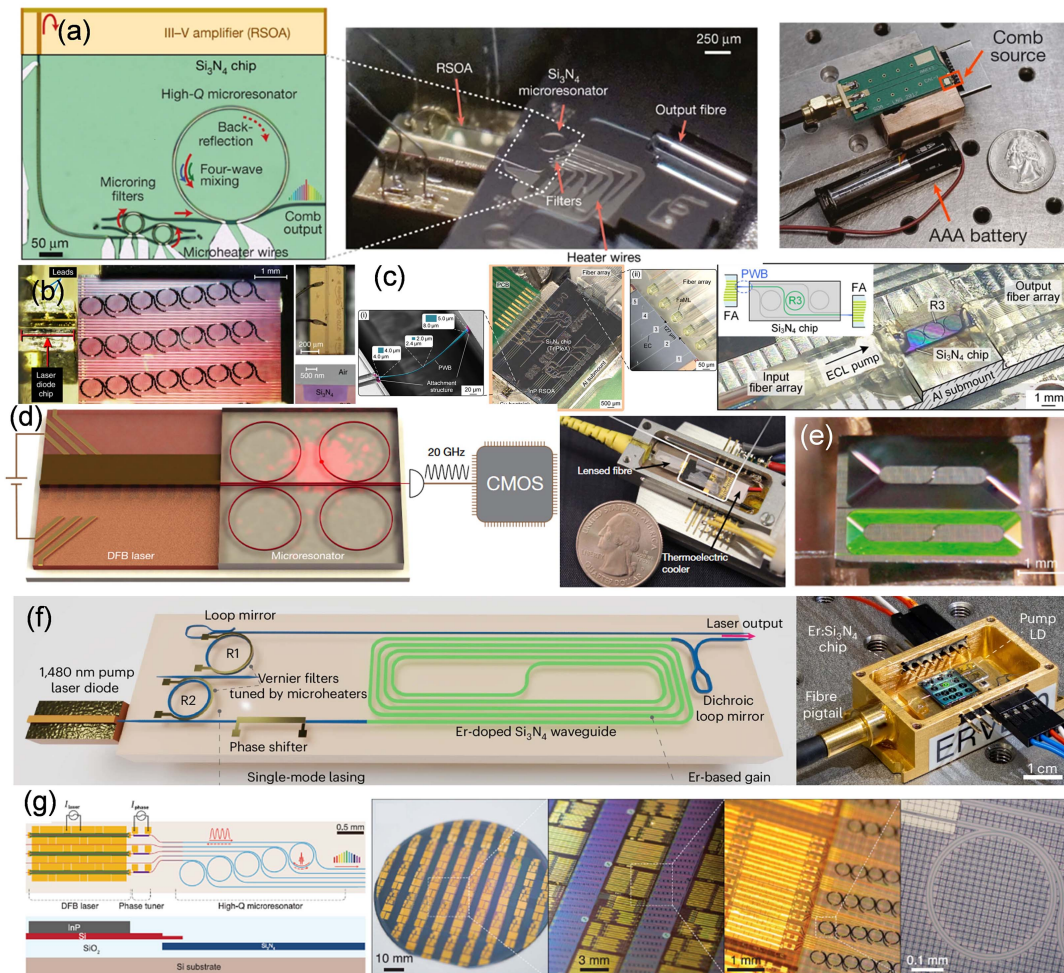


Fig. 22 Recent advances in packaging and integration technologies for microcombs. (a) Hybrid integrated amplifiers with microcavities for microcomb generation^[62]. (b) Direct butt-coupling of the laser diode with the microcavity chip for self-injection locking^[138]. (c) Photonics wire bonding^[226]. (d) Packaged microcomb module with a laser diode butt-coupled with a microcavity chip^[77]. (e) The integrated Er-doped amplifier chip^[227]. (f) The schematic (left) and the packaged (right) Er-doped laser chip^[228]. (g) Single-chip microcomb generators^[66].

Despite these packaging technologies having facilitated the hybrid integration of microcombs, they remain expensive and time-consuming. For large-scale production, fully on-chip microcomb generation, where lasers and microcavities are patterned on a single chip^[86], is more practical. III–V metrical integration has long been a hot topic of interest in integrated photonics. Recent advancements in heterogeneous integration^[238–240] have enabled co-integration of lasers, microcavities, and even more devices. The mode-locked microcomb generation on both normal^[241] and anomalous dispersion^[86] cavities has been demonstrated on a single chip. In addition to heterogeneous integration, micro-transfer printing^[242,243] has been proposed, where prefabricated devices including lasers are transferred onto the chip. Compared with heterogeneous integration where a III–V wafer or die^[244] is bonding to the target wafer, this method features highly efficient material usage and low cost^[242]. However, the output power of the integrated laser is too low for mode-locked microcomb generation. Apart from the bonding process, the directly grown lasers^[245] on different platforms are feasible with the development of quantum dot materials^[246] and lasers^[247–249], as they do not require precise lattice matching. However, their use in microcomb generation is yet to be demonstrated. Additionally, extending to longer wavelengths remains a challenge due to material limitations.

To achieve fully integrated systems, on-chip amplification^[243], alongside the integration of lasers and microresonators, has become increasingly important. Erbium ions are a key enabler of efficient optical amplification in photonic circuits. Erbium-doped amplifiers^[250] hold significant promise, but their development has historically been hindered by limited gain and the absence of suitable platforms for integration. With the development of CMOS-compatible platforms such as Si₃N₄, significant progress has been made. Recently, a photonic integrated erbium amplifier demonstrated a small signal gain exceeding 30 dB and output power of 145 mW using ultra-low-loss Si₃N₄ waveguides with multiple injection processes of erbium ions, as shown in Fig. 22(e)^[227]. A hybrid erbium-doped waveguide laser based on erbium-doped Si₃N₄ has also been realized, providing a net gain of over 30 dB and an output power of more than 100 mW, with a narrow linewidth and high integration, as depicted in Fig. 22(f)^[228]. The development of high-performance optical amplifiers not only enhances laser output but also enables the creation of more complex designs.

4 Characteristic and Design

4.1 Spectral Shape

The spectrum of the microcomb plays a critical role in applications ranging from spectroscopy and optical clocks to communications. With a broad spectrum, the feasible optical band and the number of comb lines increase significantly. For metrology applications, such as optical clocks, it is especially desirable for the microcomb to cover an octave to enable f-2f self-referencing^[251]. In addition to the spectral span, the spectral shape is also important. For applications where the microcomb is used as a multi-tap carrier, a flat spectrum is essential for inter-channel balance.

4.1.1 Influence of dispersion on spectral shape

The dispersion properties of the cavity fundamentally determine the spectrum's characteristics^[179], as summarized in Table 5. In most cases, anomalous dispersion is necessary for the

generation of microcombs^[11]. In an anomalous dispersion cavity, the mode-locked state is the so-called “bright soliton”, as discussed in previous sections, shown in Fig. 23(a). These mode-locked microcombs exhibit a sech² shape in both the optical spectrum and time pulses^[174]. Generally, the relationship between the spectrum 3 dB bandwidth $\Delta\omega_{\text{comb}}$ and the second-order dispersion β_2 can be described by^[253]

$$\Delta\omega_{\text{comb}} \sim 0.63 \sqrt{\frac{2\pi P_{\text{pump}} F_{\text{cavity}}}{\beta_2}}, \quad (16)$$

where P_{pump} is the pump power and F_{cavity} is the finesse of the cavity. A broader spectrum is expected with a weak second-order dispersion.

Apart from the second-order dispersion, higher-order dispersion also plays a significant role. The dispersion wave due to high-order dispersion is investigated^[173,225], showing that a cluster of comb lines with relatively high power is excited due to the local wave packet's match with the soliton pulses in the cavity. The excitation of dispersion waves is the most common method for generating microcombs with over-octave spectra, depicted in Fig. 23(c). Recently, octave-spanning microcombs have been demonstrated on various platforms through the excitation of dispersion waves, aided by delicate dispersion engineering^[206,225,254,255].

As discussed, weak second-order dispersion can be beneficial for achieving a wide spectrum. When second-order dispersion approaches zero, higher-order dispersion factors begin to dominate the mode-locking process, resulting in distinct and diverse mode-locked pulses^[256]. Such dispersion conditions are called near-zero dispersion. Generally speaking, mode-locked microcombs exhibit flatter central spectra when even higher-order dispersion is dominant^[257]. For example, under pure fourth-order dispersion, mode-locked pulses present a Gaussian shape in both optical spectra and time pulses, showing a flatter central part compared to bright solitons supported by anomalous dispersion^[64,258,259]. These mode-locked states are often referred to as quartic solitons^[64], as shown in Fig. 23(d). The mode-locked states have also been studied in theory and simulation under sixth- and eighth-order dispersion^[257,260]. When odd higher-order dispersion dominates, mode-locked pulses present complex finger-like shapes where multiple tips are confined in a cluster, illustrated in Fig. 23(e). The parameter regions for the existence of different pulses overlap^[252,261], leading to a phenomenon known as snake-collapse soliton trace. Mode-locked state generation and characterization have been demonstrated in both fiber cavities^[262] and integrated microcavities^[263].

The aforementioned mode-locked pulses all appear as bright pulses, characterized by high peak pulses supported by a relatively low continuous wave background. In contrast, under normal dispersion, the mode-locked pulse features anti-pulses or dark pulses, where dips are located on a relatively high continuous wave background, as shown in Fig. 23(b)^[72]. These dark pulses are mode-locked due to the interaction of switching waves with opposite directionalities, where one wave connects from a high-power state to a low-power state and vice versa. In the optical spectrum, dark pulses exhibit rapid power drops near the central part, followed by flat “wings” away from the center^[264]. Typically, the optical bandwidth of dark pulses is narrower compared to bright solitons, while it can cover over

Table 4 Integrated Solutions for Microcomb Generation

Ref.	Method	Integrated Solution	Hybrid/Heterogeneous
[62]	Edge coupling	RSOA-MRR	Hybrid
[77]	Self-injection locking/edge coupling	DFB-MRR	Hybrid
[86]	Wafer bonding	DFB-phase tuners-MMR	Heterogeneous
[138]	Self-injection locking/edge coupling	Laser diode-MRR	Hybrid
[226]	Photonic wire bond	External cavity laser	Hybrid
[227]	Fiber connection	Er:Si ₃ N ₄	Heterogeneous
[228]	Edge coupling	Laser diode-optical amplifier	Hybrid

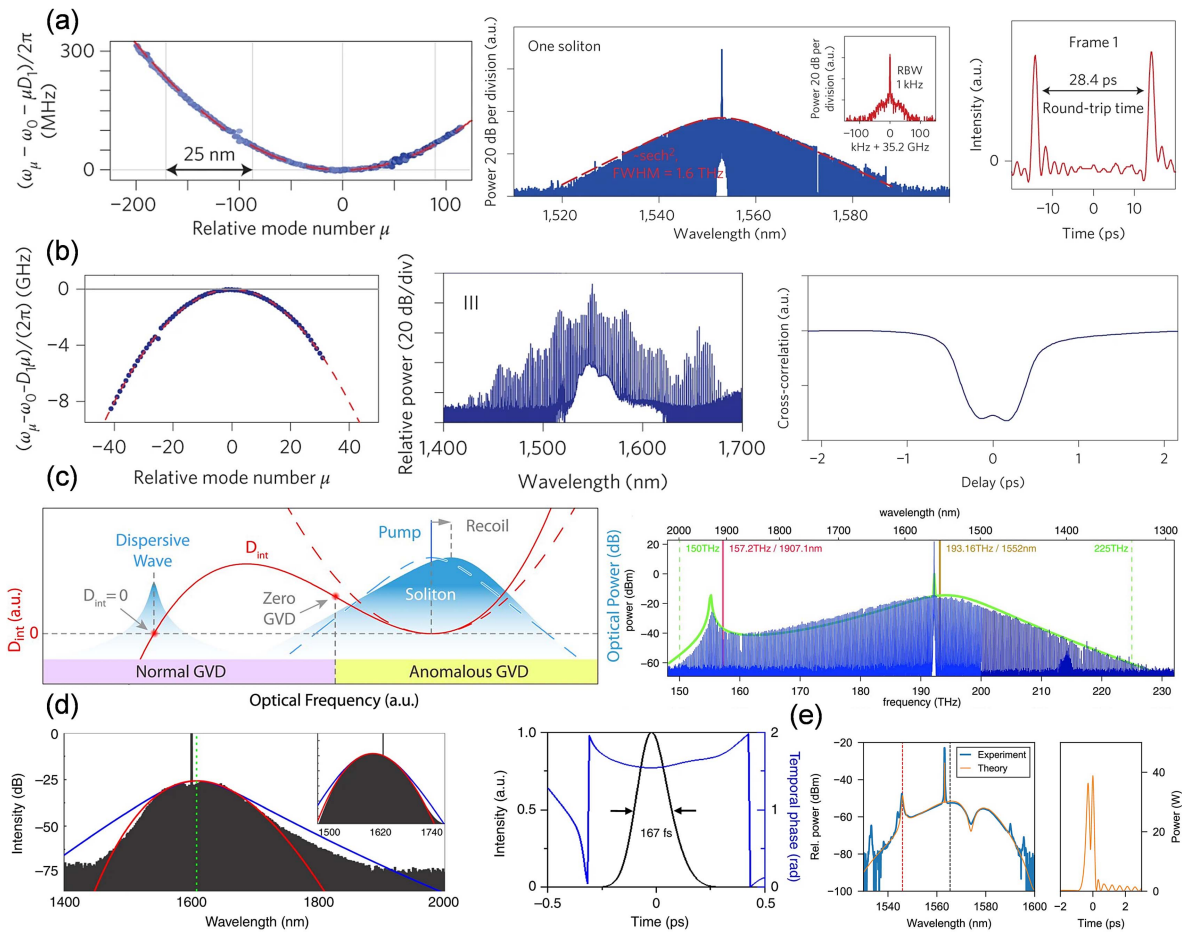


Fig. 23 Microcombs under different dispersion conditions. (a) Bright soliton under anomalous dispersion^[11]. (b) Dark pulse under normal dispersion^[72]. (c) Dispersion wave due to high-order dispersion^[73]. (d) Quartic soliton supported by fourth dispersion^[64]. (e) Bright pulse under near-zero dispersion^[252].

300 nm under relatively weak second-order dispersion factors^[264].

4.1.2 Dispersion engineering for microcombs

As discussed above, the core aspect of designing the spectrum is dispersion engineering, a long-standing topic in the field of microcombs^[179], as summarized in Table 6. In earlier research,

dispersion engineering was primarily based on tuning the waveguide structure, such as the height and width of the waveguide^[225]. In addition, complex waveguide structures are proposed to meet specific dispersion design requirements^[259]. For example, a concentric microring^[61] is designed to provide wide-band anomalous dispersion, as depicted in Fig. 24(a). In addition, the waveguide structure of the microcavity can be tapered^[64] to tune the dispersion of the whole cavity.

Table 5 Comb State in Different Dispersion Conditions in an Experiment

Ref.	Dispersion Condition	Pulse Type	Platform
[11]	Anomalous dispersion	Bright soliton	MgF ₂
[72]	Normal dispersion	Dark pulse	SiN
[73]	Anomalous dispersion with high-order dispersion	Bright soliton with dispersion wave	SiN
[252]	Third-order dispersion	Bright pulse	Fiber
[256]	Third-order dispersion	Bright pulse	SiN
[64]	Fourth-order dispersion	Quartic soliton	SiN
[263]	Fifth-order dispersion	Bright pulse	SiO ₂

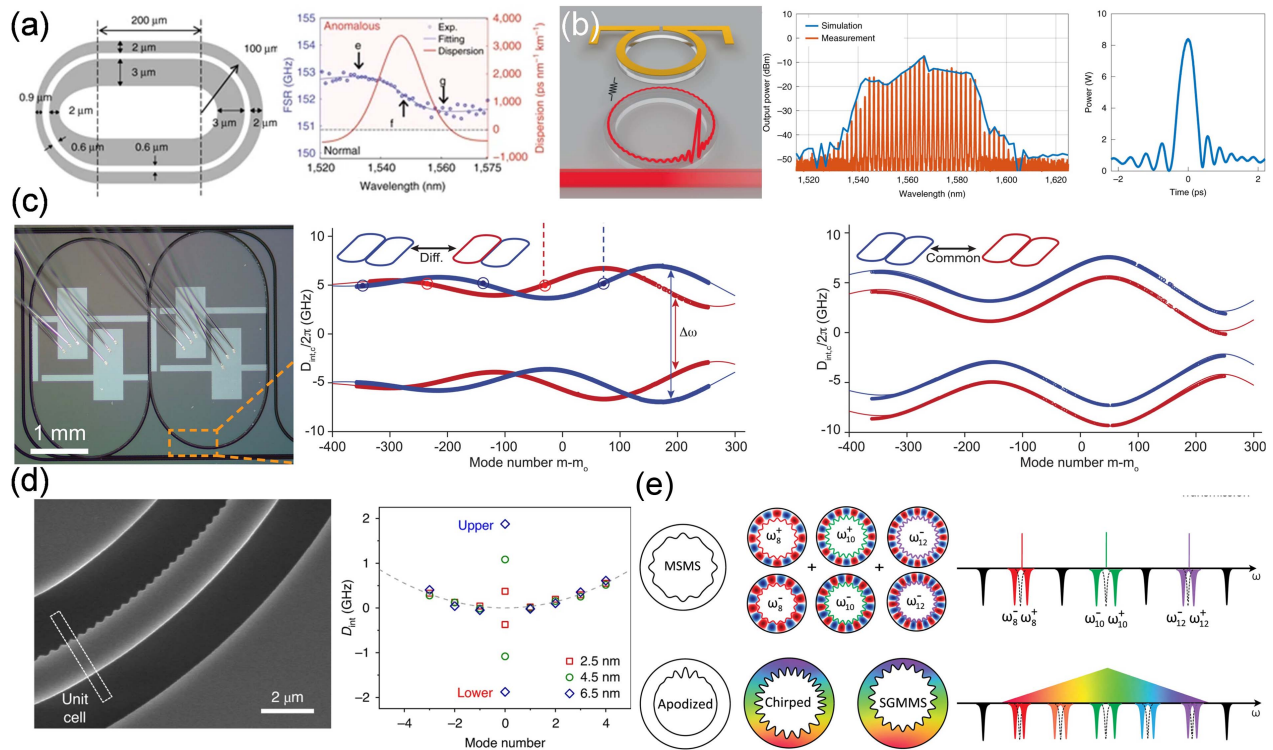


Fig. 24 Different dispersion engineering methods. (a) Concentric microring^[61]. (b) Coupled rings for single-point dispersion changing^[78]. (c) Coupled rings for wideband dispersion changing^[68]. (d) PhCR for single-point dispersion changing^[65]. (e) PhCR for multiple-point dispersion changing^[265].

For flexible dispersion design, inter-mode interaction^[132,266] is utilized for dispersion engineering. As the microcavity supports multiple mode families, anti-crossing resonance splitting caused by inter-mode coupling can be employed for dispersion engineering. When the group velocity difference between two modes is large, inter-mode coupling induces localized dispersion changes as the resonant frequencies converge^[266]. These localized changes can introduce effective anomalous dispersion in a normal dispersion cavity, providing modulation instability (MI) gain for microcomb generation with the forward sweeping process. In 2014, researchers demonstrated microcomb generation in normal dispersion cavities assisted by coupling between different modes^[58]. In 2015, dark pulse microcombs were demonstrated^[72]. These dispersion changes can also

introduce dispersion waves in bright soliton microcombs within anomalous dispersion cavities^[74]. In another scenario, where the group velocity difference is quite small and the coupling between different modes is strong, wideband dispersion changes are possible^[267]. Such properties have been used to generate bright solitons in normal dispersion cavities. However, this method requires the existence and inter-mode coupling of multiple modes, which is undesired for high-*Q* operation. In addition, the design for wideband dispersion changing is challenging for integrated platforms. The robust design and tunability challenges remain significant obstacles.

Similarly, the coupled ring scheme can function as two modes for dispersion engineering^[59,78], illustrated in Figs. 24(b) and 24(c). The coupling can be distinctly induced by the

interaction between different rings, and the coupling state can be tuned by adjusting the resonant frequency difference between the rings. When a microring is coupled with a microring with a large FSR difference, localized dispersion changes can be induced^[59,67], similar to the coupling between different mode families in a single cavity. This scheme has been used for the tunable generation of dark pulses in normal dispersion cavities^[59,268] and the controllable dispersion wave of bright solitons in anomalous dispersion cavities^[269]. When the two microrings feature closely matched FSRs and strong intra-cavity coupling, wideband dispersion changes are induced^[270,271]. Tunable nonlinear processes including soliton generation and Brillouin lasers have been demonstrated^[68].

Recently, advancements in fabrication have enabled the coupling between forward-backward fields within a single microring using intracavity gratings, known as photonic crystal microrings [PhCRs, shown in Fig. 24(d)]^[272,273], for flexible dispersion profile design. In the design of the intracavity grating, the periodic structure is usually positioned on the inner side of the waveguide to reduce the interaction of the optical field with the etched side. When both the resonant condition and the Bragg condition are satisfied, the corresponding resonance splits into two due to the coupling between the forward and backward fields^[273]. The split frequency is determined by the coupling coefficient, which is designed based on the grating shape. Using PhCRs, the continuous evolution of dark pulses in normal dispersion cavities^[264] and self-excitation of bright solitons in anomalous dispersion cavities^[65] have been illustrated. Theoretically, if the grating structure is synthesized from periodic structures with different periods, as shown in Fig. 24(e), it is possible to separately regulate multiple resonances within a single ring^[265,274]. This has been proven in recent works. Researchers propose a reverse design method where the grating structure can be produced according to the required spectrum shape. For demonstration verification, a flat microcomb is generated using a dispersion-engineered PhCR^[69].

Beyond dispersion engineering, new intracavity dynamics are also being researched. For wideband spectra, it is possible to cover different bands by injecting another pump laser to excite and coherently combine the generated microcombs^[275,276]. For flat spectra, a new type of soliton, the Nyquist soliton, has been proposed to produce flat microcombs driven by the bandpass response^[116].

In conclusion, the development of microcombs with tailored spectra involves delicate dispersion engineering processes. Each approach has its unique challenges and advantages, and ongoing research continues to refine these methods. The integration of these advanced techniques into scalable platforms will be crucial for applications such as telecommunications, spectroscopy, and metrology.

4.2 Conversion Efficiency

Assisting with the enhancement of power density in high-quality-factor cavities, microcombs are an efficient method for broadband optical comb generation^[225]. As integrated cavities reach quality factors of 10^7 – 10^8 , microcombs can be excited using integrated laser sources^[62,138]. However, the low power conversion efficiency of mode-locked microcombs hinders their broader application^[280]. Conversion efficiency is typically defined as the ratio between the generated comb power and the input pump power^[281,282]. In anomalous dispersion cavities, the conversion efficiency of single bright solitons in a cavity with a few hundred GHz FSR is typically limited within a single-digit percentage range^[283]. Such low conversion efficiency indicates low comb line powers, necessitating optical amplification for subsequent systems. This amplification process introduces amplifier noise, which degrades the entire system's performance. Therefore, improving power efficiency or increasing the power of comb lines is crucial for the practical applications of microcombs. Thus, we compared the microcomb conversion efficiency across different schemes, as listed in Table 7.

In anomalous dispersion cavities, multi-soliton states exist, presenting multiple bright pulses within one period. Compared to single-soliton states, the conversion efficiency increases with the number of solitons^[284]. However, coherent interference between different solitons causes significant fluctuations in the spectral envelope. Under certain conditions, such as a background field induced by mode-crossing or an assisting laser, multiple solitons can form soliton crystals, where the time spacing between solitons is equal^[102]. In the optical spectrum, equally spaced comb lines will be significantly strengthened while other comb lines are weakened or even completely canceled. Thus, a few comb lines contribute to most of the comb power, making them unsuitable for applications requiring a flat spectrum. Similarly, dark pulse microcombs in

Table 6 Design Methods for Dispersion Engineering

Ref.	Method	Functionality	Reconfigurability	Fabrication Challenge
[225]	Waveguide design	Wideband dispersion tuning	N	N
[64]	Tapered waveguide	Wideband dispersion tuning	N	N
[61]	Concentric microresonator	Wideband dispersion tuning	N	N
[266]	Inter-mode coupling	Local dispersion tuning	Y	N
[267]	Inter-mode coupling	Wideband dispersion tuning	Y	N
[65]	Photonic crystal microring	Local dispersion tuning	N	Y
[69]	Photonic crystal microring	Wideband dispersion tuning	N	Y
[59]	Coupled rings	Local dispersion tuning	Y	N
[68]	Coupled rings	Wideband dispersion tuning	Y	N

normal dispersion cavities exhibit high conversion efficiency ($\sim 50\%$), but most of the power is concentrated in the central part of the comb^[277]. With the aid of dispersion engineering using coupled rings, the flatness of the spectrum can be improved^[78].

Compared to dark pulses, the low conversion efficiency of single solitons can be attributed to the low power overlap between the continuous pump wave and the mode-locked pulse, as depicted in Fig. 25(a)^[277]. The continuous wave pump is not

efficiently transferred to the soliton, resulting in low conversion efficiency. Therefore, high conversion efficiency can be achieved with pulse pumping^[130]. Pulse pumping involves using short pulses to pump the microcavity, which can more effectively transfer energy to the solitons. Gain switched to a laser or continuous wave laser with intensity modulation can be used as the pulse pump^[130]. Figure 25(b) shows the typical spectrum of the pulse-pumped solution. With optimized pulse shape and detuning, a maximum efficiency of 34% can be achieved^[66].

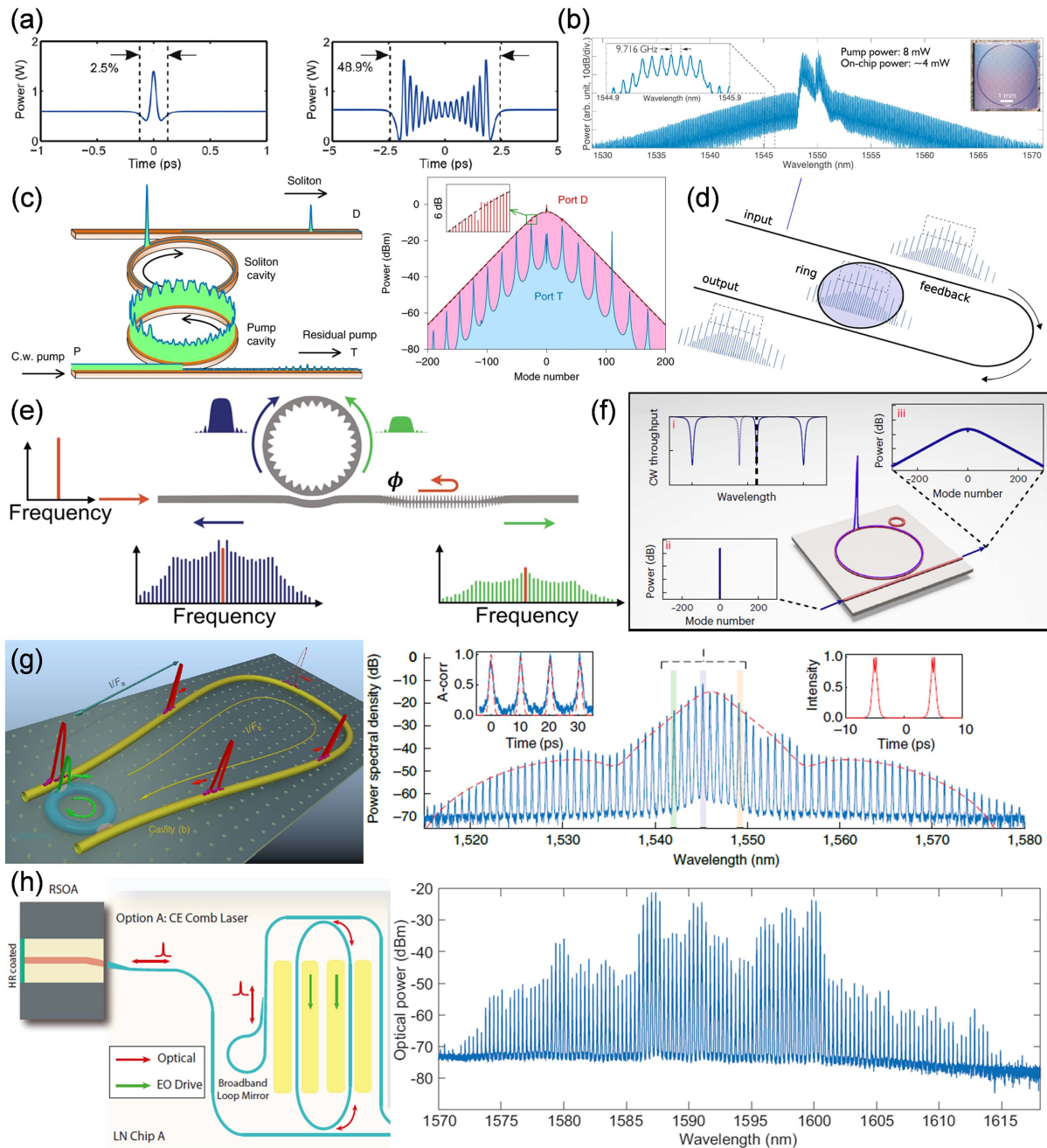


Fig. 25 Schemes for high-efficiency microcombs. (a) The comparison between the soliton and the dark pulse^[277]. (b) The pulse pumped soliton^[130]. (c) Pump recycling for high efficiency with dual rings^[63]. (d) Interferometric back-coupling for high-efficiency solitons^[278]. (e) Interferometric back-coupling for high-efficiency dark pulses^[279]. (f) Dispersion engineering for high-efficiency solitons^[67]. (g) Soliton laser for high-efficiency microcombs. (h) The electrically empowered microcomb laser^[81].

However, generating pulse pumps is much more complex than continuous pumps, and the repetition rate of the pump pulses must be finely tuned and locked to match the resonance of the microcavity accurately.

Since most of the pump power is not on resonance, researchers have proposed recycling^[63] or reinjecting^[278] the pump into the microcavity to increase efficiency. Figure 25(c) shows a coupled ring scheme, where one ring functions for power recycling and the other for comb generation^[63]. Theoretically, this approach can achieve a conversion efficiency of up to 98%, and the principle has been demonstrated in fiber cavities. However, this scheme is challenging to implement on an integrated platform due to the precision required to align the coupled rings. As shown in Fig. 25(d), two-point coupling structures are developed, where the pump is coherently coupled into the cavity at the second coupler^[278]. Thanks to the interferometric back-coupling strategy, the conversion efficiency increased to 55% in experiments and 80% in simulations for soliton crystal combs. However, achieving single-soliton states with this method has not yet been demonstrated. A similar scheme for the dark pulse is proposed, as depicted in Fig. 25(e). A reflector is positioned after a PhCR for pump reinjection, resulting in a conversion efficiency of 65%^[279,285]. The input and output are separated through the circulator, which is challenging for integration.

Recently, studies on new soliton dynamics have enabled soliton microcombs with high conversion efficiency. In coupled ring systems [Fig. 25(f)], single-point splitting facilitates the generation of high-efficiency single solitons. By precisely tuning the pump power, coupled rings, and detuning, single-soliton microcombs with conversion efficiencies up to 50% have been demonstrated with a 10 mW pump^[67]. However, the tuning process is quite complex. This complexity arises from the need to balance various parameters precisely to maintain a stable single soliton. As shown in Fig. 25(g), a hybrid cavity structure is proposed, where a high- Q microring resonator (MRR) is nested within an active fiber ring cavity. With the excitation of the gain medium under proper conditions, the mode-locked microcomb can be excited by turnkey operation, achieving a conversion efficiency of 75%^[76]. A fully on-chip hybrid cavity is developed, as shown in Fig. 25(h), hybridizing lasing, Kerr nonlinearity, and modulation processes in a single hybrid cavity^[81]. Although the simple excitation method and high conversion efficiency of such hybrid cavities are promising, this scheme requires precise alignment of the two cavities' resonances. The alignment for the integrated platform is difficult.

Overall, while substantial progress has been made, challenges remain in achieving microcombs with simple excitation, integration for wafer-scale production, and high conversion efficiency.

4.3 Noise

Noise in microcombs is a critical factor affecting their performance in various applications, including spectroscopy, optical clocks, telecommunications, and quantum information processing. Understanding^[287] and suppressing^[45] noises are essential for optimizing the functionality and reliability of microcombs. This section will review these two aspects, respectively.

4.3.1 Noise source

The noise in microcombs can be attributed to the following factors.

Technical noise: this includes various environmental factors such as temperature fluctuations, mechanical vibrations, and acoustic noise. For example, when coupling the pump laser from a fiber to the microcomb chip, relative vibration between the fiber and the chip can cause pump fluctuations on the chip, inducing noise in the output microcomb.

Pump laser noise: since the microcomb is excited by the pump laser, the noise of the pump directly affects the noise of the generated microcomb. The impact of the pump laser's intensity noise and phase noise on the microcomb can be studied separately to understand their contributions.

Thermal noise: according to thermodynamics, there will be random fluctuations in temperature-related variables, which contribute to noise. Due to the thermo-optical effect and thermal expansion, the cavity is affected by temperature changes, leading to vibrations in the resonant frequency. These vibrations contribute to the noise in the generated microcomb.

Quantum noise: fundamental quantum fluctuations, such as shot noise and spontaneous emission noise, also contribute to the noise in microcombs. These are particularly relevant in low-power regimes where quantum effects become significant.

Similar to the pump laser, the noise of the microcomb can be divided into intensity noise and frequency noise. In most cases, the research on microcomb noise is focused on the frequency noise or phase noise. According to the numerical relationship, phase noise and frequency noise can be converted into each other:

$$S_\nu(f) = f^2 S_\phi(f), \quad (17)$$

where ν and ϕ are the frequency and phase of the detected source, S_ν and S_ϕ are the power spectrum densities of ν and ϕ , and f is the Fourier frequency. As a multiplex frequency source, the frequency of each comb line can be expressed as

$$f_n = f_{\text{ceo}} + n \cdot f_{\text{rep}}, \quad (18)$$

where f_{ceo} and f_{rep} are the CEO frequency and the repetition rate, n is the index of the comb line counted from f_{ceo} , and f_n is the frequency of the comb line. Thus, the fluctuation of f_{ceo} and f_{rep} can be used to characterize the noise of the whole microcomb. In another case, the comb equation can be expressed as

$$f_m = f_{\text{pump}} + m \cdot f_{\text{rep}}, \quad (19)$$

where f_{pump} is the frequency of the pump laser, m is the index counted from the pump laser, and f_m is the frequency of the comb line. In this equation, it is clear that the pump noise contributes to the frequency fluctuation of the microcomb. Ideally, the noise of each comb line would match that of the pump laser. However, the repetition rate changes with the detuning between the pump laser and the resonant frequency of the microcavity. This is caused by the pulse recoiling with the dispersive wave and the Raman self-frequency shift. In general, f_{rep} can be expressed as^[291]

$$f_{\text{rep}} = \frac{1}{2\pi} \left[D_1 + \frac{D_2}{D_1} \cdot (\Omega_{\text{Raman}} + \Omega_{\text{Recoil}}) \right], \quad (20)$$

where the Raman term Ω_{Raman} and the recoil term Ω_{Recoil} are functions of the detuning. Due to the fluctuation of f_{rep} relative

Table 7 Conversion Efficiency of Mode-Locked Microcomb

Ref.	Strategy	Pulse type	Efficiency
[283]	—	Bright soliton	~1% ^a
[277]	—	Dark pulse	31.8%
[60]	Dual-cavity coupling	Dark pulse	40.6%
[66]	Pulse pumping	Bright soliton	34%
[63]	Pump recycling	Bright soliton	94.2% ^a
[278]	Interferometric back-coupling	Soliton crystal	55%
[279]	Interferometric back-coupling	Dark pulse	65%
[67]	Dispersion engineering	Bright soliton	54%
[286]	Dispersion engineering	Dark pulse	51%
[76]	Hybrid cavity	Soliton laser	75%
[81]	Hybrid cavity	—	100% ^b

^aIn simulation.

^bClaimed optical power conversion.

to the pump frequency, the frequency noise of each comb line can be written as

$$S_{f_m}(f) = S_{f_{\text{pump}}}(f) + m \cdot S_{f_{\text{rep}}}(f). \quad (21)$$

Thus, the frequency noise of comb lines will increase apart from the pump mode. As shown in Fig. 26(a), the intrinsic linewidth Δf_m of each comb line can be given by^[288]

$$\Delta f_m = \Delta f_{\text{pump}} \cdot \left(1 - \frac{m}{m_{\text{fix}}}\right)^2 + m^2 \cdot (\Delta f_{\text{RIN}} + \Delta f_Q), \quad (22)$$

where Δf_{pump} is the intrinsic linewidth of the pump laser, Δf_{RIN} and Δf_Q are contributions of pump laser intensity noise and shot noise, and $m_{\text{fix}} = -(df_{\text{rep}}/df_{\text{pump}})^{-1}$ is the pump phase noise fixed point. With the balance between different factors, the minimum intrinsic linewidth is not at the pump mode^[288].

Aside from pump noise, the thermal noise [shown in Fig. 26(b)] of the cavity imposes a limitation on the noise of the microcomb. The thermal noise of a variable X can be expressed as

$$\langle \delta X^2 \rangle = \eta_X^2 \frac{k_B T^2}{\rho C V}, \quad (23)$$

where $\eta_X = dX/dT$ is the thermal coupling coefficient, k_B is the Boltzmann constant, ρ is the mass density, C is the specific heat, and V is the volume. This indicates the increased noise with the decrease of the cavity volume. This indicates that the noise increases as the cavity volume decreases. For microcombs, compact cavities are used to achieve large repetition rates, which leads to a high thermal noise level. The noise $\langle \delta f_{\text{rep}}^2 \rangle$ of f_{rep} can be given as

$$\langle \delta f_{\text{rep}}^2 \rangle = \eta_{f_{\text{rep}}}^2 \frac{k_B T^2}{\rho C V}. \quad (24)$$

Due to the thermal noise, the effective linewidth will increase as the comb line apart from the pump mode, depicted in

Fig. 26(c). This feature has been widely observed in experiments^[287,289]. In conclusion, the phase noise $S_{f_{\text{rep}}}^\phi$ of the repetition rate can be written as^[229]

$$S_{f_{\text{rep}}}^\phi = \beta^2 S_{f_{\text{pump}}}^\phi + \frac{\alpha^2}{f^2} S_{\text{RIN,pump}} + D_1^2 S_{\text{TRN}} + S_Q, \quad (25)$$

where S_Q is the quantum jitter, $S_{f_{\text{pump}}}$ and $S_{\text{RIN,pump}}$ are frequency noise and the relative intensity noise of the pump laser, and S_{TRN} is the cavity thermal noise.

4.3.2 Noise suppression method

Different methods have been proposed to suppress different noise sources for high-coherence optical microcombs. The most straightforward method to enhance the coherence is to reduce the noise of the pump laser. Different laser sources exhibit different noise levels. For example, fiber lasers^[292] typically have lower noise compared to semiconductor lasers^[293]. In addition, locking schemes such as the well-known Pound-Drever-Hall (PDH) locking loop^[294] can be used to suppress the noise of the pump laser. With the detection of f_{ceo} and f_{rep} , the noise of microcombs can be greatly reduced by locking these two essential frequencies^[45,295]. The intensity noise of the pump laser can also be suppressed by employing the power control devices with feedback loops^[296]. Despite the high coherence achieved through these locking processes, the overall systems are too complex and challenging to integrate. Recently, the self-injection locking methods have been proposed to provide high coherence with integrated lasers, illustrated in Fig. 26(d). By locking the semiconductor laser to the high- Q microcavity, the phase noise of the hybrid laser can be suppressed to the level of advanced fiber lasers^[140]. Combining the turnkey operation of self-injection locking with heterogeneous integration, fully on-chip high-coherence microcombs can be achieved^[86].

In addition, it is feasible to enhance the coherence by reducing thermal noise. As expressed in Eq. (24), cavity thermal noise is related to the cavity volume. Thus, thermal noise can be reduced using large cavities. A large cavity requires high pump power. The large cavity size and high pump power requirement contradicts the need for integration. Also, the cavity size is

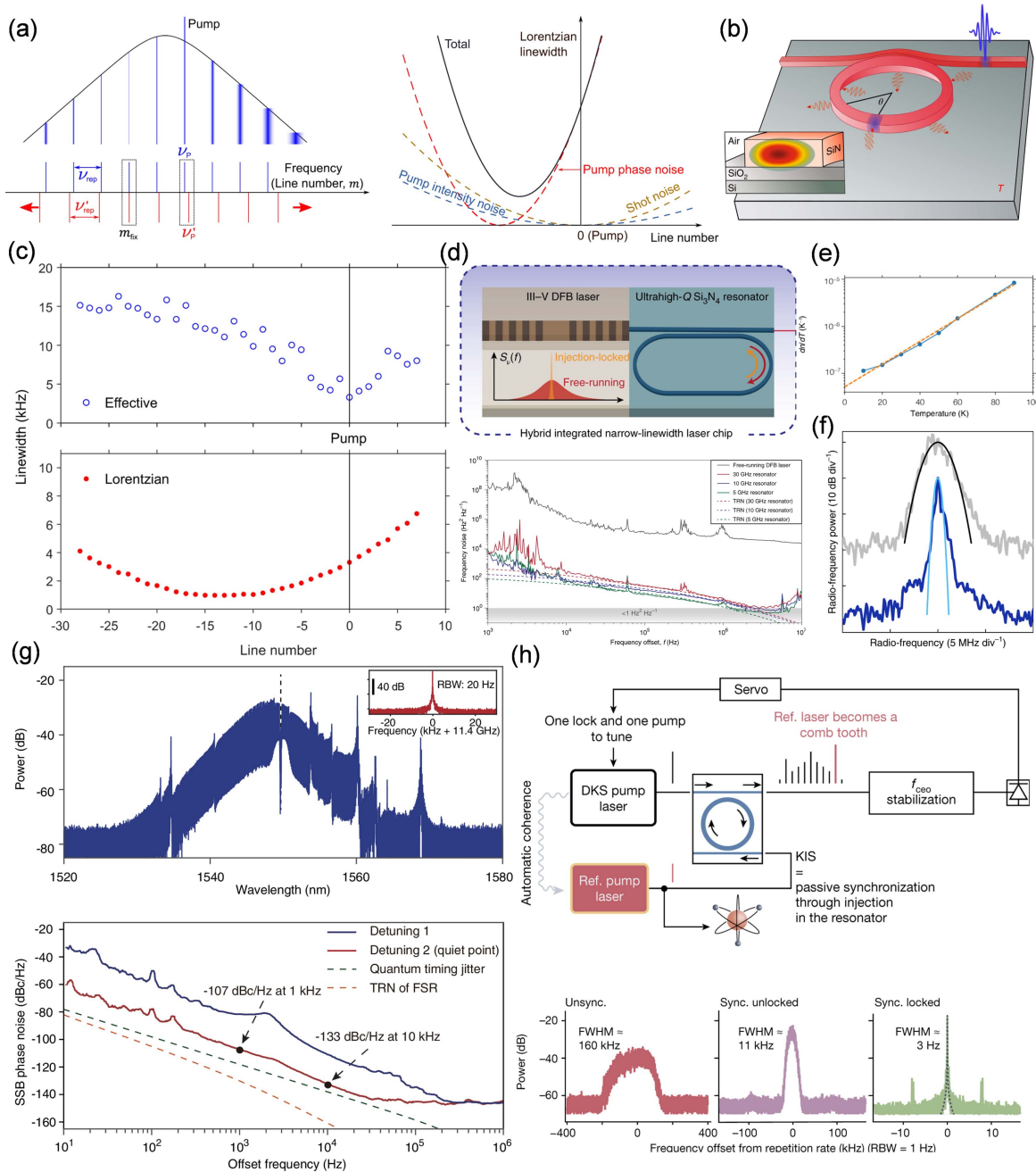


Fig. 26 Noise sources and suppression methods. (a) Different noise sources for the intrinsic linewidth of comb lines^[288]. (b) The influence of thermal noise^[289]. (c) Intrinsic (top) and effective (bottom) linewidth distribution of comb lines^[288]. (d) Self-injection locking for high-coherence lasers^[140]. (e) Reduced thermal-optical effect under low temperature^[290]. (f) Suppressed thermal noise with laser cooling^[289]. (g) Low-noise soliton microcomb operating at the quiet point^[176]. Top: spectrum; bottom: phase noise of the repetition rate. (h) KIS for reducing the repetition rate fluctuation^[80].

usually determined by the desired f_{rep} of the microcomb. Since the influence of cavity thermal noise on the microcomb is partially from the thermal-optical effect^[289], reducing the thermo-optical coefficient can mitigate this influence. Composite waveguide structures with positive and negative thermo-optical coefficients are proposed^[297]. However, such waveguides require costly multiple depositions of different thin film materials. The quality factor is too low at present steps, obstructing mode-locking comb generation. High pump laser power may

also increase thermal noise due to heating by the pump laser. The thermal-optical coefficient can be reduced by decreasing the temperature. For instance, researchers from NIST have proposed thermal effect suppression at cryogenic temperatures^[290], as depicted in Fig. 26(e). However, low-temperature environments require expensive cooling and temperature control equipment. As mentioned in the comb generation section, an assistance laser could be used to balance intracavity temperature changes during the transition from chaotic to soliton states.

Similarly, an assistance laser can be injected into the cavity to cool the cavity after carefully tuning the frequency of the assistance laser [Fig. 26(f)]^[289]. A lower effective temperature can be obtained with higher assistance laser power within a reasonable pump power range.

Except for directly suppressing pump laser noise and cavity thermal noise, the phase noise of microcombs can be reduced by leveraging the nature of mode-locked microcombs. As shown in Eq. (20), both the Raman effect and the dispersion wave can cause the shift of f_{rep} with the detuning. In certain cases, the shift directions are opposite, leading to the reduced fluctuation in f_{rep} ^[298]. Ideally, these two shifts can be completely canceled out at a working condition known as the quiet point^[291], resulting in suppressed noise. Operating at the quiet point can reduce the phase noise of f_{rep} by 20 dB^[176], as depicted in Fig. 26(g). However, this scheme requires the proper position of the dispersion wave. The dual-ring scheme has been proposed to introduce the controllable dispersion wave^[299]. As for dark pulses, recent research indicates a lower noise floor limited by the shot noise compared with the bright solitons^[300].

In most cases, the mode-locked microcombs are generated with a single continuous wave pump. Recent studies reveal that the mode-locked microcomb can be locked to the background field induced by additional fields^[107]. By modulating the pump with a radio frequency close to the FSR of the microcavity, deterministic single-soliton generation can be achieved^[131]. The modulated wave can also lock the generated soliton. In the optical spectral domain, the modulated pump can be viewed as the injection of two or more continuous waves with spacing equal to the cavity FSR^[301,302]. The injection of another laser far away from the pump is also demonstrated to lock mode-locked pulses. In 2023, a laser locked to the Rb reference was directly injected into the microcavity, resulting in the stabilization of the soliton^[80]. Such injection locking process is called Kerr-induced synchronization (KIS), shown in Fig. 26(h). With KIS, the full-width-half-max of f_{rep} is reduced from 160 to 11 kHz. Combined the locking of f_{ceo} with f-2f self-referencing, the FWHM of f_{rep} is locked to 3 Hz. On platforms with electro-optical effects, a microwave signal with a frequency close to f_{rep} of solitons can be directly applied to the microcavity. The generated solitons will be locked to the applied microwave signal^[207]. Besides the injection from an external source, the self-injection of one comb line can also stabilize the microcomb^[303]. Viewed as an oscillator, the phase noise of the self-injected comb line can be suppressed by 30 dB.

Suppressing noise in microcombs is crucial for their performance in various high-precision applications. By employing methods such as reducing pump laser noise, managing thermal noise, leveraging the intrinsic properties of mode-locked microcombs, and using advanced locking techniques, researchers continue to improve the coherence and stability of microcombs. These advancements pave the way for more reliable and integrated microcomb systems, expanding their potential in scientific and technological applications.

5 Applications

Optical frequency combs serve as a powerful tool for spectroscopy and metrology (i.e., the precision measurement of various physical quantities, including frequency, time, and velocity, as well as broadband spectrum information analysis, such as gas sensing and molecular fingerprinting). Over the past decade, microcombs have driven a significant shift in these techniques

towards integrated photonics by enabling more compact, efficient, and versatile optical systems. Moreover, benefiting from its extended frequency repetition, the microcomb finds new opportunities in the fields of wavelength division multiplexing (WDM) communications, LiDAR, computing, and microwave photonics. The unique dynamics during the nonlinear process, including the chaotic state, also facilitate the development of novel applications for anti-interference ranging and random-bit generation. Very recently, research efforts targeting highly integrated microcomb-based systems have been initiated, marking a significant step toward achieving monolithic optical frequency comb systems. In this section, we review the recent progress in microcomb-based applications, covering areas such as high-precision metrology and spectroscopy, large bandwidth signal generation, transmission, and processing, newly emerging chaotic-based applications, and ongoing efforts toward the miniaturization and integration of these systems.

5.1 High-Precision Metrology and Sensing

5.1.1 Frequency standard

With strictly equal-distant frequency spacing, optical frequency combs serve as the clockwork of an optical atomic clock, which is analogous to a gear set, transferring stability between optical and radio frequencies. Such systems leverage stable atomic transitions as a reference, providing a set of referenced optical lines covering tens to hundreds of THz bandwidth while offering precise and accurate optical or microwave standards with the aid of phase-coherent multiplication or optical frequency division (OFD) techniques. An optical frequency synthesizer refers to a phase-coherent microwave-to-optical link that transfers the stability of a microwave oscillator to a referenced laser and vice versa to an optical clock.

In order to construct a reliable bridge across the entire electromagnetic spectrum, the “optical frequency ruler” must be fully stabilized. This process requires accessing two parameters: the frequency spacing of the comb lines f_{rep} and the CEO frequency f_{ceo} . As introduced in Sec. 2, the absolute frequency of each comb line can be described as $f_m = f_{\text{ceo}} + mf_{\text{rep}}$ (m is the mode number). Among f_m , f_{ceo} , and f_{rep} one frequency parameter could be determined or stabilized once the other two are known or locked to the reference. The repetition rate could be directly accessed from the beat note of the adjacent comb line, while the CEO frequency stabilization usually relies on the well-known f-2f self-reference technique.

Here we briefly introduce relative works, as illustrated in Fig. 27. The stabilization techniques of microcombs at early stages mainly focus on the locking of mode spacing and one of the comb modes. In contrast to mode-locked lasers, the pump mode can be directly accessed since it is part of the microcomb itself. Thus, the power and frequency detuning of the pump laser provides two degrees of freedom for stabilization. Specifically, f_{rep} can be tuned through the power-dependent refractive index change of the microresonator. In this way, Del’Haye *et al.* perform a complete microcomb stabilization in fused silica toroids with 86 GHz mode spacing^[306]. All-optical stabilization could be realized by locking two comb lines to separate laser references. A microcomb generated from a silica disk resonator is stabilized to two distributed feedback (DFB) lasers^[42], as shown in Fig. 27(b), which are frequency-doubled and stabilized to D1 and D2 Rb transitions, respectively. The synthesized microwave output at a precise subdivision of the Rb reference performs a

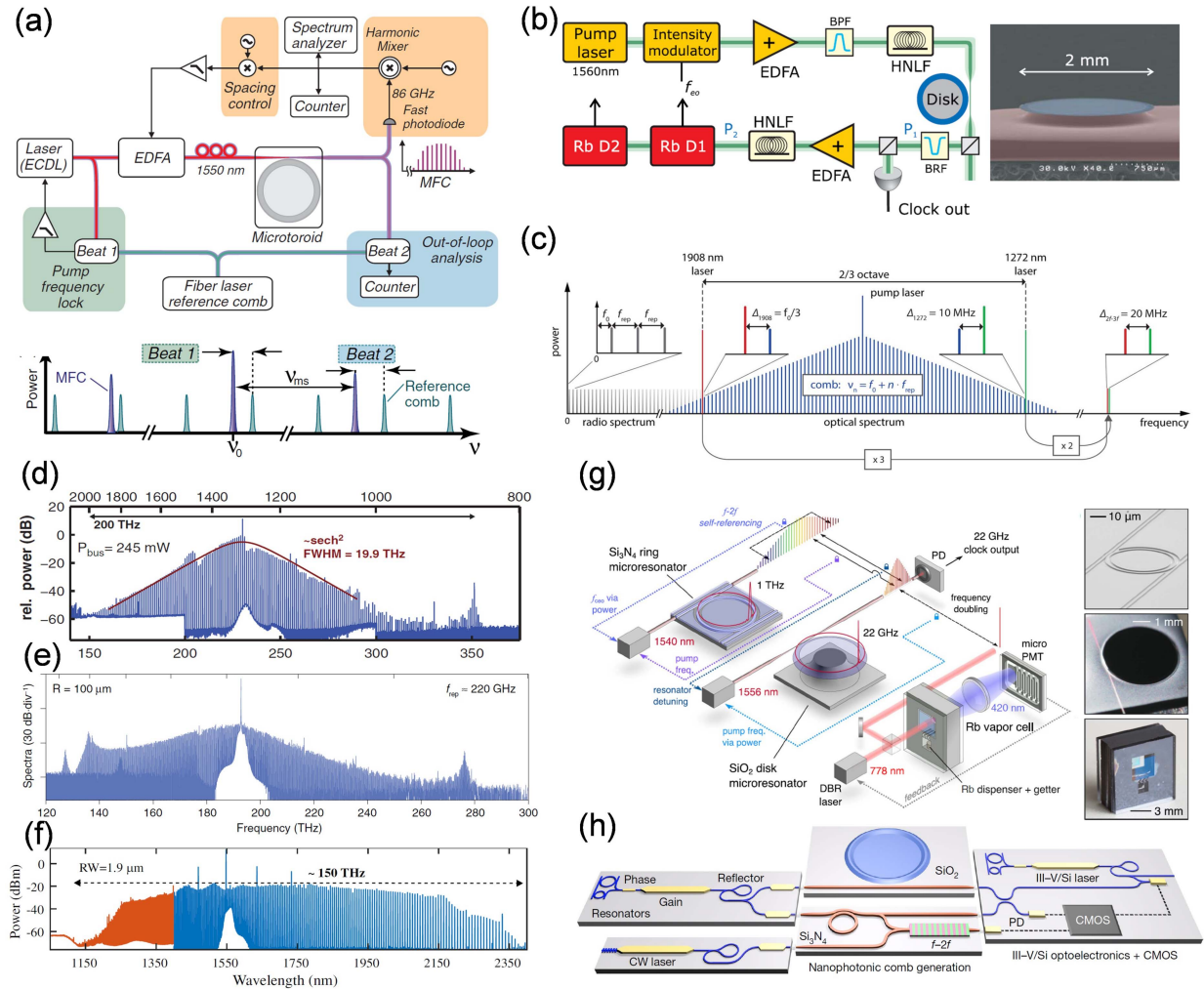


Fig. 27 Microcomb-based frequency standard. The stabilization of the microcomb could be achieved by locking (a) one optical mode and repetition frequency^[67], (b) two separate optical modes^[42], and (c) repetition frequency and CEO frequency via the f-2f technique^[304]. First demonstrations of octave-spanning microcomb on (d) SiN^[225], (e) AlN^[206], and (f) 4H-SiC^[305] platforms. The highly integrated (g) optical clock^[34] and (h) optical frequency synthesizer^[46] based on dual-comb frequency clockwork.

5×10^{-9} Allan deviation for 1 s averaging, which is improved by a factor of ~ 100 over the DFB lasers determined by the fluctuations of the Rb reference.

Moreover, the demonstration of a self-referenced microcomb system is of particular importance since it provides a direct microwave-to-optical link by measuring and controlling the offset frequency of the microcomb. Direct octave-spanning broadband coherent microcomb generation necessitates rigorous dispersion engineering and relatively large mode spacing. One way to broaden the microcomb spectrum in the dielectric platform is supercontinuum generation by injection of the soliton pulse into the highly nonlinear fiber. A spectrum exceeding two-thirds of an octave is realized in a MgF₂ microresonator with this solution^[304], as shown in Fig. 27(c). With a 2f-3f self-reference interferometer, the system phase coherently links a 190 THz optical carrier directly to a 14 GHz microwave frequency. Direct f-2f referencing was demonstrated in a fused-silica microdisk resonator at a repetition rate of 16.4 GHz^[45]. The CEO frequency is stabilized to a sub-hertz level, and the absolute pump laser

stability has a standard deviation of 620 Hz at a 100 ms gate time. To further simplify the self-referencing system, an external broadening-free microcomb spanning two-thirds of an octave was demonstrated in a SiN microresonator at a repetition rate of ~ 190 GHz, using temporal DKS formation and soliton Cherenkov radiation^[307]. The stabilized pump laser exhibits a 172 Hz distribution shift for the 160 s measurement. So far, octave-spanning microcombs have been realized on SiN, SiC, and AlN platforms^[144,206,225,305,308], with their free spectral ranges set at 1 THz or sub-THz levels, as shown in Figs. 27(d)–27(f).

The large repetition rate in octave-spanning microcombs leads to challenges in f_{rep} and f_{ceo} detection since those frequencies are too large for detection with present electric equipment. Two solutions are proposed to overcome this challenge. In one way, a second microcomb with detectable microwave repetition is employed to serve as the frequency gearbox between THz and microwave signals^[34]. Another approach is frequency down-mixing by electro-optic modulation. Through the electro-optic modulation, modulated sidebands are

generated around the original comb teeth, with the spacing equal to the applied microwave frequency. In this way, a terahertz signal with 0.01 mHz accuracy and precision^[309] resulting from the perfect division of an optical reference is presented, with the absolute frequency noise to one part in 10^{17} .

For the next-generation optical clockwork system, integration level has always been a hot topic. The integrated architectures for both optical frequency synthesizers and optical atomic clocks have been proposed^[34,46], as shown in Figs. 27(g) and 27(h), respectively. The highly integrated synthesizer shows the combination of a heterogeneously III–V/silicon laser whose frequency is stabilized to a microwave standard, guided by a cascaded frequency chain enabled by separated microcombs. The output laser can be programmed by a microwave clock across 4 THz with 1 Hz resolution^[46], with a synthesis error of 7.7×10^{-15} . As for the optical clock, a pair of interlocked microcombs helps the stability transition from a locked semiconductor laser to its repetition rate. The generated 22 GHz electrical clock shows a fractional frequency instability of one part in 10^{13} . Although the performance needs to be further optimized, the hybrid system, with several silicon-chip devices playing the core function, has already shown its advantages in cost, size, and power consumptions^[34].

More recently, a novel method for high-frequency f_{ceo} and f_{rep} detection has been proposed by a pair of Vernier microcombs with slightly different repetition rates^[310]. Such a strategy offers the ability to simultaneously detect 900 GHz repetition rate and 97 GHz CEO frequency, indicating its large potential in self-referencing techniques and optical clock applications.

5.1.2 Spectroscopy

Frequency comb technology has revolutionized precision measurements in spectroscopy since its first application in

the 1970s^[315]. When it comes to microcomb-based spectroscopy, it mainly focuses on molecular fingerprinting measurement^[316]. With the efficient optical nonlinear process, microcombs can span a broader range of frequencies compared to other integrated counterparts like integrated mode-locked lasers and electro-optical combs. This capability allows microcombs to cover a richer spectrum of spectral information. By injecting the frequency comb into the environment to be detected, the spectral information is loaded on the comb in different manners, such as absorption. Two different methods have been proposed to extract the loaded spectral information: direct frequency comb spectroscopy and dual-comb spectroscopy, as illustrated in Fig. 28.

Direct frequency comb spectroscopy (DFCS) is the simplest approach. By directly detecting the loaded information, the spectral information of the environment is obtained. A pump-laser-free scheme is utilized to directly perform the gas-phase spectroscopy^[312], where the microcomb is generated with a dual-resonance configuration^[317]. To measure broadband molecular absorption spectra of acetylene, the microcomb is tuned by the on-chip micro heater for spectra interleaving. More concisely, to achieve megahertz-linewidth molecular spectroscopy, Stern *et al.* decouple the control of repetition frequency and offset frequency with a phase modulation scheme^[318], therefore allowing substantial scanning and stabilization. The DFCS of the cascaded transition of around 10 MHz linewidth atomic transition in Rb at 1529.37 nm is demonstrated, indicating absolute optical frequency fluctuations at the kilohertz level over a few seconds and <1 MHz day-to-day accuracy. Moreover, by coupling microcombs with plasmonic systems, Zano *et al.* recently proposed a plasmonic-cavity-enhanced platform for high sensitivity and multidimensionality spectroscopy^[313]. By projecting the microcomb to a water-cladded prism-based plasmonic

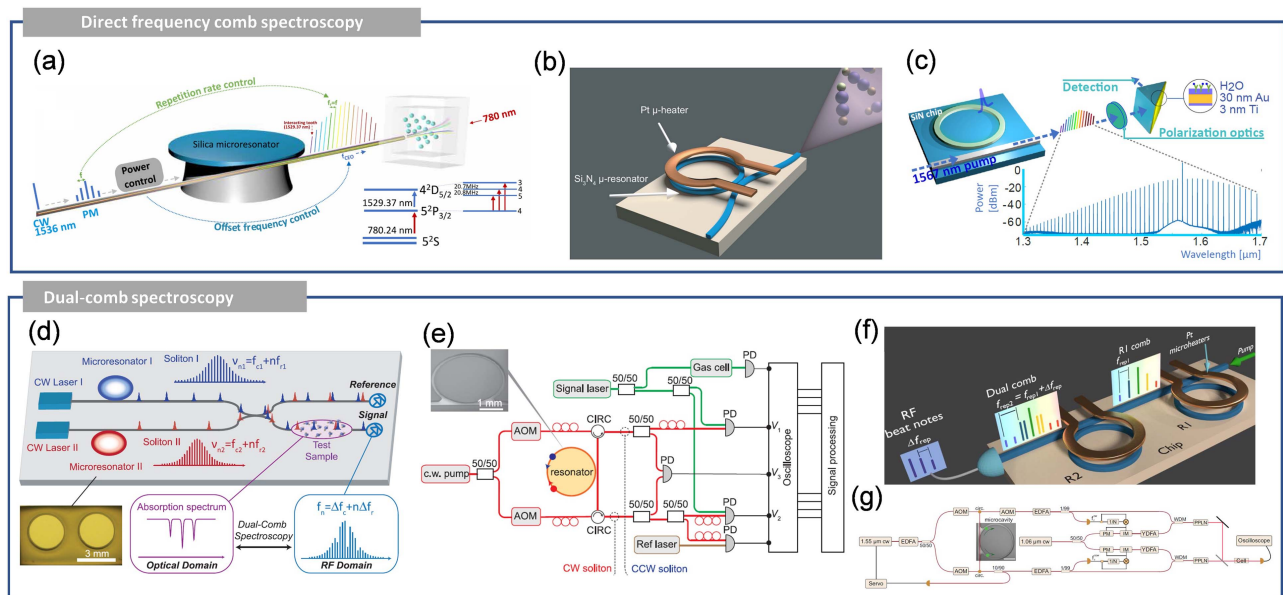


Fig. 28 Microcomb-based spectroscopy. The direct frequency comb spectroscopy (DFCS) utilizes a single frequency comb for molecular fingerprint recognition, which can measure (a) atomic transition^[311] and (b) gas phase^[312]. (c) The plasmonic-enhanced DFCS systems^[313]. Dual-frequency spectroscopy (DCS) is enabled by a pair of microcombs, which can be generated simultaneously by (d) separately pumping^[36], (e) counterpropagating stimulation, and (f) single-pump driving^[314]. (g) The microcomb densification via iDFG scheme^[50].

resonator, the approach offers insights into the analyte's concentration, dispersion, and resonance characteristics.

Dual-comb spectroscopy (DCS) offers a non-invasive method for Fourier transform interferometry without moving parts^[319]. It works by mapping an optical comb into radio frequency by multiheterodyne beat with a second comb featuring a slightly different repetition rate. For microcomb-based DCS compared with previous mode-locked lasers, it holds the advantage of a higher FSR, which allows a higher δf_{rep} between the two combs, requiring a shorter minimum acquisition time to resolve the beat notes. In 2016, Suh *et al.* demonstrated the first microcomb-based DCS^[36], where a microcomb pair with frequency repetition of approximately 22 GHz and δf_{rep} of 2.6 MHz was employed. The microcombs used here were pumped separately with different lasers; thus, the coherence and stability of the heterodyne beats were limited. To further enhance the coherence time, highly coherent dual-comb pairs were generated monolithically. Dutt *et al.* proposed a single-laser-pumped DCS system on the SiN platform^[320], leading to a long mutual coherence time of 100 μs via on-chip micro-heater tuning. Absorption spectroscopy of dichloromethane was obtained, spanning a 170 nm wavelength range over a fast acquisition time of 20 ms. Meanwhile, by utilizing a dual-locked counterpropagating soliton generated from a single microresonator, Yang *et al.* demonstrated a Vernier spectrometer^[314]. The counterpropagating microcomb is inherently phase-locked at two spectral points, which offers an exceptionally stable radio-frequency grid^[321]. To extend the spectral detection range, a silicon-chip-based DCS system was proposed^[322], with a single-laser-pumped dual-comb configuration spanning across 2.6 to 4.1 μm . Absorption DCS in the liquid phase is realized by acquiring spectra of acetone spanning from 2900 to 3100 nm at 127 GHz resolution. To further densify the comb lines in mid-infrared, Bao *et al.* proposed an architecture for GHz microcomb DCS using interleaved difference-frequency-generation (iDFG)^[50]. Four combs consisting of two counterpropagating

microcombs at 1550 nm and two EO combs at 1064 nm are generated in a highly locked form, where the repetition frequency of the EO comb is driven and divided from the repetition rates of the microcombs. With the iDFG process, a pair of mid-IR combs with dense spectra could be generated. Meanwhile, the common-mode fluctuations can be canceled out during the multiheterodyne DCS detection process, leading to a normalized DCS precision as high as $1.0 \text{ ppm} \cdot \text{m} \cdot \text{s}^{1/2}$. With highly inherent coherence and multidimensional tunability, the microcomb-based DCS holds great potential for integrated spectroscopy with high signal-to-noise ratios and fast acquisition rates.

5.1.3 Light detection and ranging

LiDAR has been extensively studied and commercially equipped for various applications such as geology, atmospheric physics, and autonomous navigations^[325]. Primarily, there are two types of LiDAR detection schemes: time-of-flight (ToF) and frequency-modulated continuous wave (FMCW). ToF measures distance by directly calculating the time it takes for a light signal to travel to the target and back, while FMCW LiDAR measures distance and velocity by analyzing frequency shifts of the beating signal between the reflected signal and the emitted signal. The former scheme requires a pulsed light source, and the latter one needs a frequency-tunable laser. By replacing conventional laser sources with microcombs (shown in Fig. 29), a microcomb-based LiDAR system can achieve faster and more accurate ranging with a compact form^[326]. This improvement stems from the parallel characteristics and inherent inter-channel consistency of microcombs.

For the ToF scheme, a dual-comb configuration is employed, which utilizes multi-heterodyne detection between a pair of coherent soliton combs with a slight difference in repetition frequency. This setup combines delay-time measurement with coherent interference, enhancing the precision and accuracy of distance measurements by leveraging the stability and

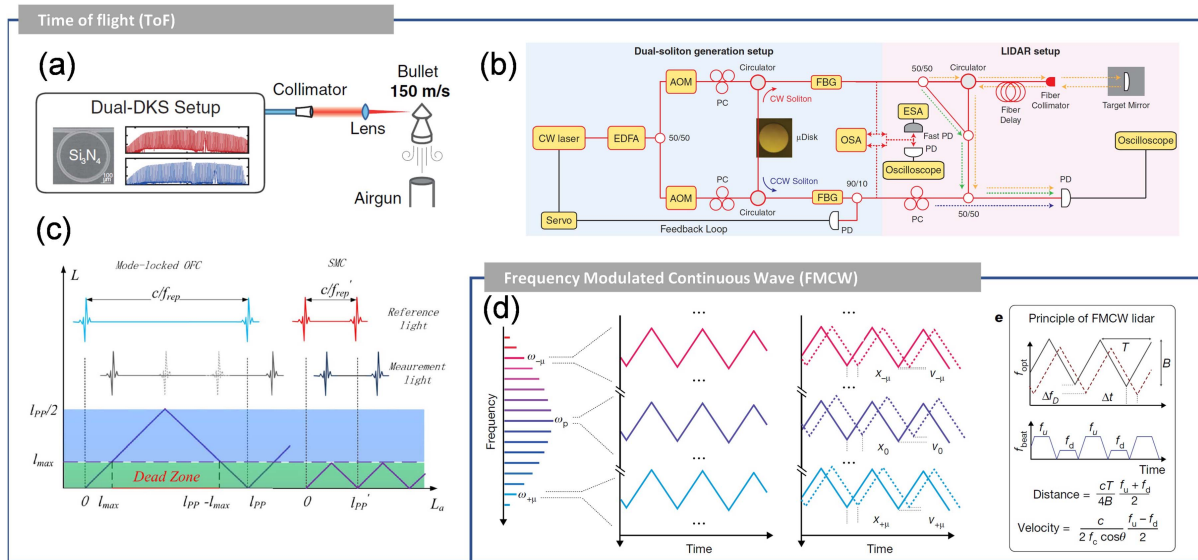


Fig. 29 Microcomb based LiDAR. Two kinds of LiDAR schemes, ToF and FMCW, are implemented in microcomb-based LiDAR systems. (a) A pair of separated microcombs^[35] and (b) a pair of counter-propagating microcombs^[323] are employed for ToF schemes. (c) Microcomb-based dispersive interferometry^[324] for accurate ranging under long distances. (d) Principle of parallel FMCW LiDAR^[49].

coherence of the soliton combs. In Ref. [35], dual-comb distance measurements have been demonstrated with impressive precision, achieving Allan deviations as low as 12 nm at averaging times of just 13 μ s. This high degree of accuracy enables ultrafast ranging with acquisition rates up to 100 MHz. Such capabilities are particularly useful in dynamic environments, allowing for the in-flight sampling of fast-moving objects like gun projectiles traveling at speeds around 150 m per second. In the meantime, Suh *et al.* performed dual-comb measurements by generating clockwise and counterclockwise soliton microcombs within a single microresonator^[323]. With a more compact system configuration, 200 nm precision with a range ambiguity of 16 mm was demonstrated, with an extendable range ambiguity of 26 km by means of the Vernier effect^[327]. More recently, a dual-comb with a shared pump has been generated for extended ambiguity distance, which enhances the coherence without additional control^[328]. To further exploit the spectrum information, microcomb-based dispersive interferometry was demonstrated^[324], where the distance information is demodulated from the interference spectrum envelope. Utilizing a high-repetition-rate microcomb matched well with a linear array image sensor, a long distance of 1179 m is real-time measured in an actual outdoor baseline field, with a minimum Allan deviation of 27 nm at an average time of 1.8 s.

The massively parallel characteristic of microcombs could also benefit the acquisition speed of the LiDAR, which is of great importance in terms of coherent ranging. A microcomb

provides a simplified parallel FMCW generator with a single-frequency-chirped pump laser, with great consistency. In Ref. [49], a microcomb-based coherent LiDAR was demonstrated with 30-channel distance and velocity measurement at an equivalent rate of 3 megapixels per second. With the optimized dual-comb configuration, a hardware-efficient microcomb-based FMCW LiDAR is demonstrated by multiheterodyne two synchronously frequency-modulated microcombs^[329]. Information for all individual ranging channels can be extracted on a single receiver, which further simplifies the system for individual separation, detection, and digitization.

Range ambiguity, a common limitation in both ToF and FMCW LiDAR systems, restricts the maximum detectable distance. Recently, a novel parallel LiDAR system utilizing a chaotic microcomb has gained extensive attention. This system circumvents traditional interference issues by emitting parallel physical random light, effectively removing the typical range limitations imposed by the period of the light signal. In Sec. 5.3, we will introduce this special LiDAR system in more detail.

5.1.4 Optical tomography

Fourier-domain optical coherence tomography (FD-OCT) provides noninvasive optical imaging for medical diagnosis and art conservation with micron-level resolution and millimeters of imaging depth. Conventionally, a commercial super-luminescent diode with continuous spectrum is employed as the light source for the FD-OCT system, in which a wider

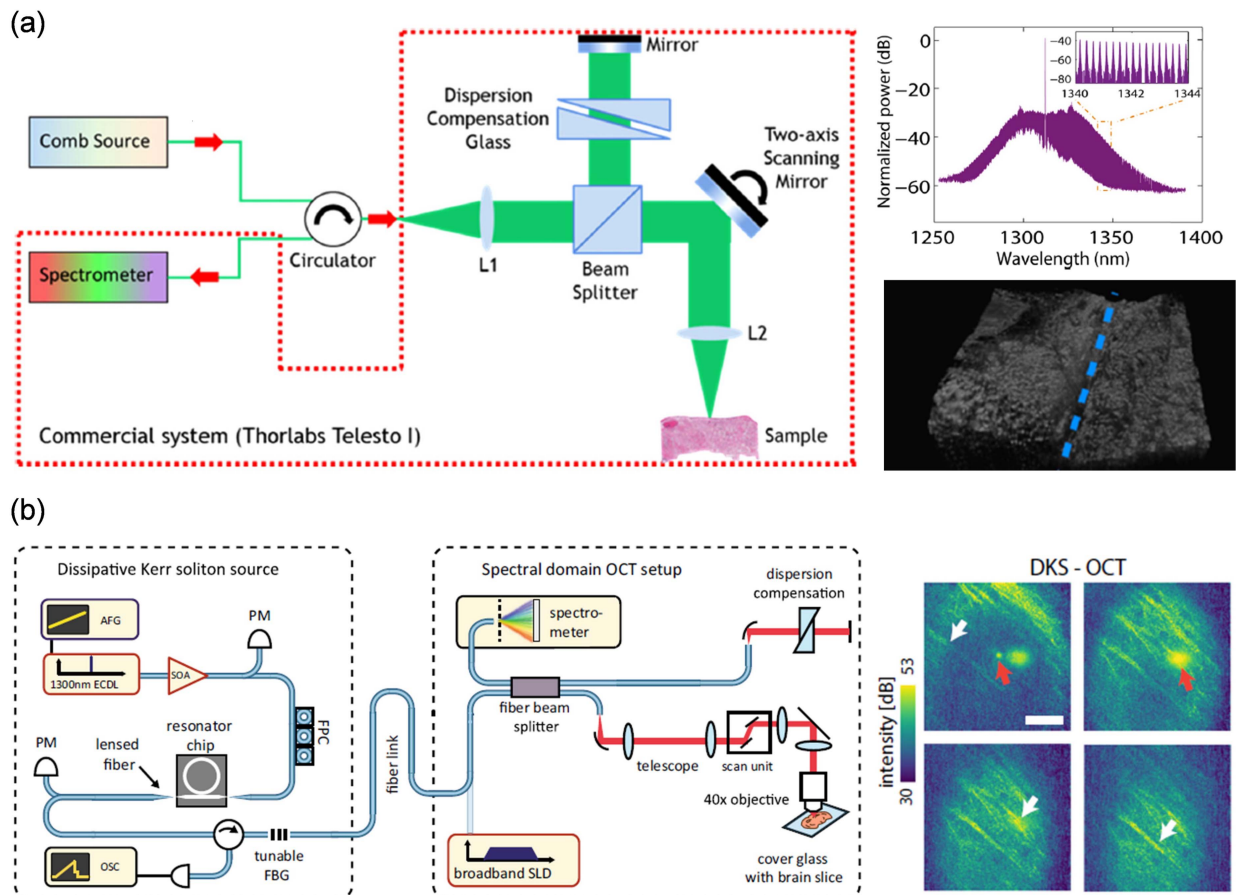


Fig. 30 Microcomb-based OCT. (a) Chaotic microcomb^[448] and (b) soliton-microcomb^[330]-based OCT setups and their scan results.

light spectrum is preferred since the axial resolution in air δz is defined by its spectral bandwidth $\Delta\lambda_{\text{FWHM}}$ ^[298]:

$$\delta z = l_c = \frac{2 \ln 2}{\pi} \cdot \frac{\lambda_0^2}{\Delta\lambda_{\text{FWHM}}} \quad (26)$$

Although it is commercially mature, the FD-OCT, especially spectral-domain OCT (SD-OCT), still suffers limitations from the depth-dependent sensitivity drop together with mirror-conjugate images, which reduces the total image range and results in performance decay^[331]. Interestingly, the optical frequency comb effectively reduces the depth-dependent drop of sensitivity, meanwhile allowing reduced interpixel crosstalk due to its discrete frequency characteristic^[332]. The chip-based frequency comb source for SD-OCT has been demonstrated recently, both in chaotic^[48] and soliton^[330] microcomb states, as separately illustrated in Figs. 30(a) and 30(b). Ji *et al.* demonstrate a SiN-based SD-OCT chaotic microcomb source, pumped at around 1310 nm with a 120 nm comb spanning bandwidth^[48]. The FSR is set at 38 GHz to avoid artifacts. The system could horizontally cover a range of 4 and 2.52 mm in depth, with an axial resolution of 16.3 μm . A soliton-state microcomb-driven SD-OCT system is proposed to further mitigate the performance impact of relatively intense noise from the light source^[330]. The chaotic nature results in a 20 dB increase factor for relative intensity noise, lowering its ultimate performance limit. The highly correlated RIN between comb lines in the soliton state is verified to have a limited effect on the background signal-to-noise ratio and imaging dynamic range. The system, therefore, exhibits a residual intensity noise floor at a high offset with 3 dB lower than the traditional incoherent OCT source, showing an axial resolution of 6 μm . By taking multiple scans and average tomograms together, the effects of individual comb line fluctuations can be nearly eliminated. In Ref. [333], 10 scans per tomogram are taken. After the software data process, the axial resolution is 5.65 μm , which is already comparable to that in a soliton microcomb.

Despite the aforementioned progress, frequency-comb-based OCT systems still face a major limitation due to the trade-off between axial resolution and imaging depth, which, until now, can only be addressed by reconstructing the data^[334]. Nonetheless, this chip-based OCT source holds promise for

portable clinical devices in low-resource settings, enabling flexible diagnostics by replacing bulky and power-consuming components.

5.1.5 Astrocomb

A microcomb could provide a precise spectral reference for exoplanet searching via radial velocity (RV) shift. The radial velocity method, also known as Doppler spectroscopy, determines the presence of exoplanets by measuring the Doppler shift in a star's spectral lines^[337]. This technique calculates the component of the star's velocity along the line of sight to the observer. Variations in the radial velocity over time, indicative of periodic shifts towards the red and blue ends of the spectrum, suggest the gravitational influence of an orbiting planet. By analyzing the amplitude and periodicity of these velocity changes, the existence, mass, and orbital characteristics of the exoplanet can be inferred with a high degree of precision. For terrestrial planet exploration, the precision must reach 10 cm/s level. Although the mode-locked laser has achieved ultrahigh velocity precision^[335], the relatively dense spectral line down to several hundreds of MHz level is not resolvable by astronomical spectrographs. Extra spectral filters are required to coarsen the line spacing to 10–30 GHz, which adds system complexity. The chip-based microcomb coincidentally fits well with this mode spacing due to its compact resonance diameter, therefore holding promise for a small footprint and low-cost system.

Two proof-of-concept works have been demonstrated for calibration of astronomical spectrographs, with either silica [Fig. 31(a)] or SiN microcombs [Fig. 31(b)], respectively. A silica micro-resonator with 22.1 GHz soliton comb line spacing is employed, with its repetition rate and one comb line locked to the Rb clock and hydrogen cyanide absorption line. This comb exhibits a frequency imprecision of 1 MHz, equivalent to about 1 m/s of RV imprecision. Eight echelle orders ranging from 1471 to 1731 nm within the astronomical H band are measured, and an actual 3–5 m/s precision is obtained^[336]. Another SiN-based astrocomb is adapted to calibrate the GIANO-B high-resolution spectrometer at the Telescopio Nazionale Galileo. To stabilize the comb, the CW pump laser was locked to a self-referenced mode-locked laser stabilized to a GPS-disciplined rubidium atomic clock. Meanwhile, the repetition rate is microwave injection-locked by referenced

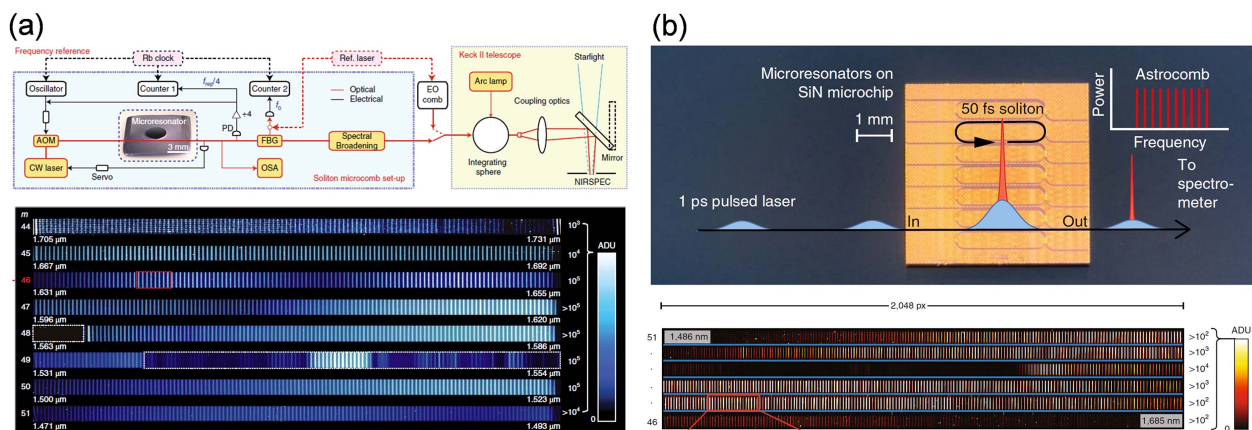


Fig. 31 Microphotonic astrocomb. (a) Silica microcomb applied to Keck II telescope^[335]. (b) SiN soliton microcomb adapted to calibrate GIANO-B high-resolution spectrometer^[336].

electro-optical modulation^[47]. Ideally, this astrocomb can support an RV precision of 1 cm/s with exposure times longer than 1 s. Compared with a traditional calibration light source, the uranium-neon (U–Ne) hollow cathode lamp, the microcomb provides a much denser grid of calibration lines with only 10 s, which is much quicker than 120 s exposure in U–Ne standard due to its stability. The calculated wavelength solution is around 25 cm/s, which is mainly limited by fundamental photon noise resulting from the analog-to-digital conversion.

Although significant progress has been made in the miniaturization of astronomical calibration standards, further research is required to optimize astrocombs for critical applications. Specifically, challenges remain in achieving astrocombs that can span the visible spectrum and offer wavelength resolution precision below 1 cm/s. Nonetheless, the microcomb, as a new class of astronomical calibration tool, offers promising opportunities for lightweight solutions, particularly in space-borne astronomical applications.

5.2 Parallel Data Transmission and Signal Processing

5.2.1 Data transmission

The parallel characteristics, combined with its compact footprint, enable the microcomb to serve as a stable multi-wavelength light source, which is crucial for scaling data transmission capacity. The microcomb integrates seamlessly with modern fiber-based WDM techniques for several key reasons:

Firstly, the mode spacing of a chip-scale microcomb naturally falls within several tens of GHz or larger, which aligns well with the current dense wavelength division multiplexing (DWDM) channel spacing standards, therefore supporting the high-capacity data transmission. Additionally, compared to commercial laser banks, the frequency spacing between optical carriers in a microcomb is significantly more stable, with deviations typically below 1%. This enhanced stability allows for more efficient use of the spectral resources (at least 10% increased bandwidth) by reducing the need for guard bands, which are usually employed to prevent inter-channel crosstalk. More importantly, the simplicity of the system is greatly enhanced by advanced microcomb generation techniques or heterogeneous integration with a pump laser. These innovations eliminate the need for external feedback control circuits for laser arrays, significantly reducing power consumption and enabling

a more compact design. This streamlined configuration not only conserves power but also paves the way for fully integrated systems, further advancing the miniaturization and efficiency of photonic devices.

A microcomb for ultrahigh data capacity, particularly for coherent communications, has been studied for over a decade, as listed in Table 8. The first demonstration for data transmission utilizing microcombs was performed in 2014^[37], where 20-channel QPSK signals at a symbol rate of 18 Gbaud were transmitted through a fiber link up to 300 km. The comb noise at this stage was reduced by a pump-controlled feedback loop. The high coherence and wide spectrum of a DKS state could further boost the data capacity. Afterward, data transmission using different coherent states of microcombs^[338–341] was intensively studied. In Ref. [338], two interleaved DKS state combs are employed to transmit an aggregate data rate of over 50 Tbps. A total of 179 channels across the entire telecommunication C- and L-bands are used at a channel symbol rate of 40 Gbaud in 16-QAM format. More interestingly, no additional penalty is observed in this case for the soliton microcomb when compared with the high-quality ECL, resulting from its highly coherent behavior. The dark-pulse soliton, characterized by a pump-to-signal conversion efficiency that is several times higher than that of a bright soliton, offers significant advantages in data encoding. Its relatively high carrier-to-noise ratio makes it particularly well-suited for encoding data in more complex formats. A high modulation format, 64-QAM, was therefore first demonstrated in a dark-pulse microcomb, which enables a transmitted OSNR above 33 dB^[339]. In this 80 km data transmission configuration, 20 channels with an aggregate data rate of 4.4 Tbps is demonstrated. Moreover, by utilizing frequency comb distillation techniques^[343] for wideband noise reduction, the required optical signal-to-noise ratio could also be reduced. To fully utilize spectrum resources in a soliton crystal microcomb, the initial 80 comb lines with 49 GHz FSR were doubled to 160 using a single-sideband modulation scheme^[340]. The dense channels therefore carried high-order-format 64-QAM signals at a 23 Gbaud symbol rate, resulting in a total data capacity of 44.2 Tbps and an ultrahigh spectrum efficiency of 10.4 bits/s/Hz. More recently, a record-breaking high microcomb parallel data transmission was demonstrated, achieving an aggregate data rate of 1.84 Pbps^[341]. This remarkable feat was accomplished using both WDM and space division multiplexing (SDM). The system employed 223 wavelength channels across

Table 8 Comparative Analysis of Parallel Data Transmission in Microcomb Systems

Ref.	Transmission Medium	Carrier Comb Type	Parallel Channel	Data Capacity	Distance
[37]	Fiber	—	20λ	1.44 Tbps	300 km
[338]	Fiber	Bright soliton	179λ	55.0 Tbps	75 km
[339]	Fiber	Dark pulse	20λ	4.4 Tbps	80 km
[340]	Fiber	Soliton crystal	160λ	44.2 Tbps	75 km
[341]	Fiber	Dark pulse	$223\lambda + 37$ core	1.84 Pbps	7.9 km
[75]	Fiber	Bright soliton	20λ	1.68 Tbps	50 km
[56]	Fiber	Dark pulse	$34\lambda + 6$ core	61.2 Tbit/s	1 km
[52]	Free-space optical	Soliton laser	42λ	1.02 Tbps	1 km
[342]	Wireless THz	—	—	60 Gbps	50 cm

a 37-core fiber, showcasing the immense potential of microcomb technologies in scaling up data transmission capacities in optical communication networks.

In addition to increasing capacity, parallelized data transmission in systems utilizing microcombs imposes a significant burden on the receiving end due to the substantial amount of digital signal processing (DSP) required for coherent communications. This complexity arises because each of the numerous parallel channels must be individually processed, decoded, and synchronized, which demands extensive computational resources. As the number of channels and the data rate per channel increase, the DSP tasks become more challenging, potentially leading to higher latency and power consumption at the receiver. The synchronization of two individual microcombs^[75] could alleviate such resource deficiency by means of cloning a microcomb for local oscillation, which is highly coherent with the carrier-microcomb. By coupling a small fraction of one microcomb to the input of the other microresonator, two silicon nitride microcombs on separate chips could be synchronized. Therefore, DSP-based electrical frequency offset estimation (FOE) and carrier phase estimation (CPE) can be significantly simplified during coherent data retrieval. Such a scheme enabled three orders of magnitude lower CPE rate than the free-running independent carrier and LO lasers within a proof-of-concept 1.68 Tbps data transmission system^[344]. More recently, by utilizing a self-injection locking scheme in an ultra-low-loss

100 nm SiN resonator, Zhang *et al.* achieved an over 60 Tbps data transmission with nearly no CPE expenditure^[56].

Microcomb sources can also drive advancements in free space optical (FSO) communications and wireless communications. A Tbps-level parallel FSO communication system was demonstrated using 102 comb lines modulated by 10 Gbps DQPSK signals over a 1 km straight-line air transmission^[52]. Besides, using a microcomb for carrier generation in wireless communications could benefit from its inherent low noise. With both data stream and LO wirelessly transferred, a wireless communication link at 300 GHz was demonstrated. The transfer rate is 60 Gbps under 15 Gbaud 16-QAM modulation format^[342]. These applications demonstrate the versatility of microcombs in various communication platforms beyond traditional fiber optics.

5.2.2 Optical computing

Optical computing, compared with its electronic counterpart, holds the promise of “compute as it propagates”, which breaks the bottleneck of operation speed limited by capacitance meanwhile providing considerable parallelism capabilities^[347]. Very recently, optical neural networks (ONNs) have attracted significant attention due to their high throughput and energy efficiency in neuromorphic computing tasks^[348,349]. One of the natural advantages of performing matrix operation in the optical domain is

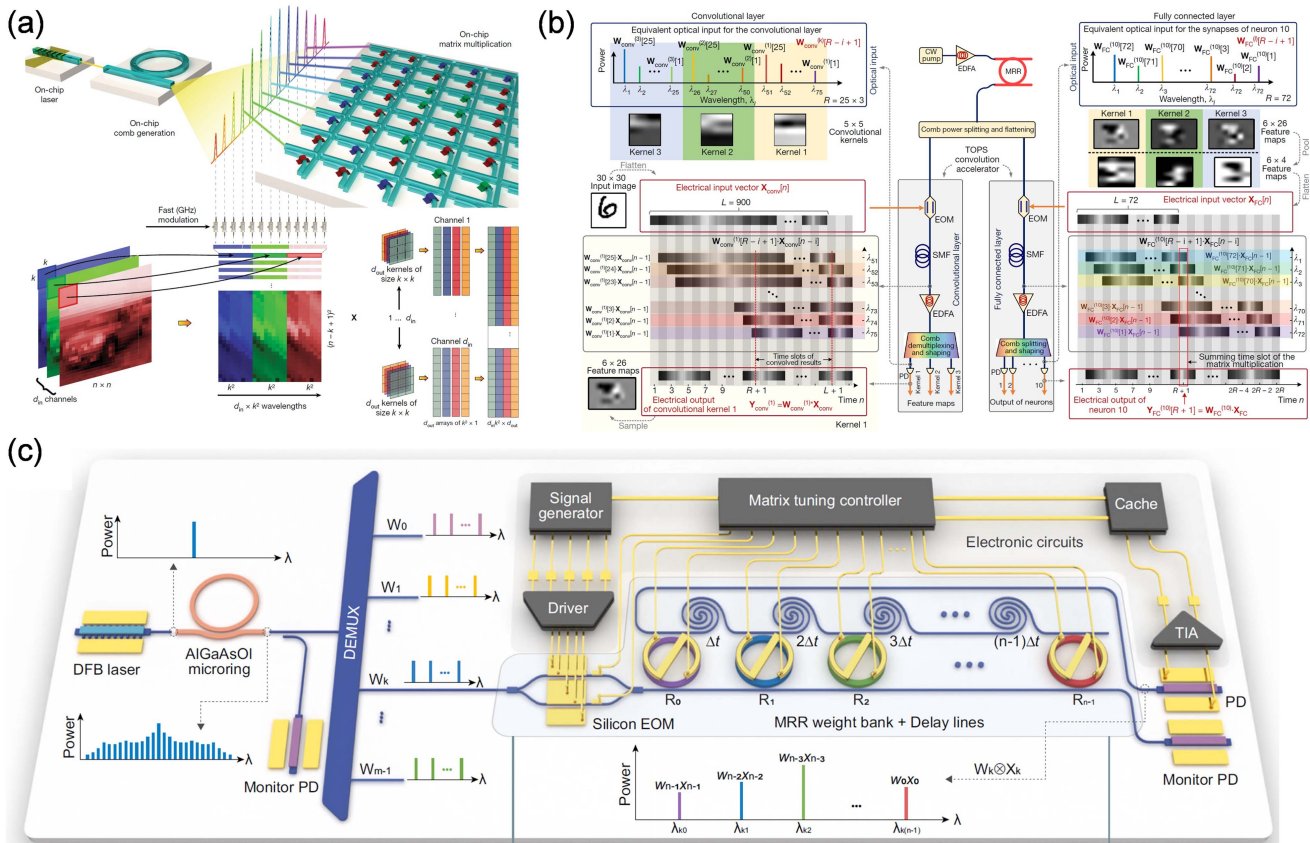


Fig. 32 Microcomb-based optical computing. (a) A SiN soliton microcomb combined with a phase-change material attached to an on-chip waveguide array for tensor core operation^[345]. (b) A time-stretch strategy for both the convolution layer and fully connected layer in the optical neural network^[51]. (c) Silicon-photonic-assisted highly integrated optical computing processor based on a microcomb^[346].

Table 9 Low-Noise Radio Frequency Generation Based on Microcombs

Ref.	Method	Generated Frequency	Platform	SSB Phase Noise
[229]	Direct generation	20 GHz	SiN	-110 dBc/Hz@10 kHz
[44]	Direct generation	9.9 GHz	MgF ₂	-130 dBc/Hz@10 kHz
[353]	Direct generation	100 GHz	SiN	-80 dBc/Hz@10 kHz
[301]	Microwave injection locking	14.09 GHz	MgF ₂	-130 dBc/Hz@10 kHz
[140]	Optical self-injection locking	5 GHz	SiN	-114 dBc/Hz@10 kHz
[295]	Fiber-photonics stabilization	22 GHz	Silica	-130 dBc/Hz@10 kHz
[80]	Kerr-induced synchronization	1 THz	SiN	-75 dBc/Hz@10 kHz
[354]	Optical frequency division	14 GHz	SiN	-135 dBc/Hz@10 kHz
[355]	Optical frequency division	100 GHz	SiN	-114 dBc/Hz@10 kHz
[356]	Optical frequency division	20 GHz	SiN	-130 dBc/Hz@10 kHz
[357]	All-optical frequency division	16 GHz	SiN	-128 dBc/Hz@10 kHz
[42]	Optical frequency division	33 GHz	Silica	—

the ultra-large frequency bandwidth. Wavelength, as a new degree of freedom for parallel computing, isolates different channels by its intrinsic orthogonality so that each individual comb line could serve as an element in the matrix. Using traditional multi-wavelength laser arrays, small-scale ONNs have been demonstrated^[350,351]. However, further increasing the number of individual lasers significantly adds to the power consumption and system complexity. Interestingly, the massively parallel nature of microcombs can be leveraged to handle the complexity of large models in optical neural networks, making them well-suited for scaling up.

To verify this, two proof-of-concept demonstrations have been proposed, as shown in Figs. 32(a) and 32(b). A “photonic tensor core” consists of a silicon nitride microcomb and a phase-change material (PCM) attached to waveguide networks^[345]. This processor implements parallel MVM operation using multiple wavelengths, while the 16×16 PCM cell matrix serves as a weight vector, attenuating matrix elements based on their phase configurations. Both sequential and parallel MVM operations are performed to accelerate the image edge highlighting, including more than 63000 inner-product operations with the entire convolution processed at a speed of 1 kHz. Also, a CNN digital recognition task is performed to sort 10000 test images with an accuracy of 95.3%. At the same time, another microcomb-based convolutional accelerator was realized by employing a time-stretch scheme^[51], where a fiber-based dispersion delay line was used to align the multiplication results at different wavelengths. This setup enabled the completion of a full multiply-accumulate (MAC) operation within the proper sampling interval. Thanks to the large optical bandwidth and quick electro-optical conversion, the vector computing speed can be as high as 11.3 TOPS. Serving as the building block of a convolutional ONN, such a processor accelerates calculations both in convolutional and fully connected layers for a handwritten digit recognition benchmark, showing an accuracy of 88%.

More recently, a highly integrated photonic processor has been proposed for the aforementioned time-stretch optical convolution operation by employing a microcomb and a silicon photonic processing unit, as illustrated in Fig. 32(c). Key functions such as the input vector loading, weight bank loading, and

the true time delay are all integrated monolithically on a silicon chip, therefore greatly simplifying the system size^[346]. Based on this system, a high compute density of over 1 TOPS/mm² is demonstrated, accelerating both image edge detection and handwritten digit recognition tasks. Demonstrating the highest level of integration in a microcomb-based optical computing system, this work has shown great promise for achieving high packing density and scalability in integrated optical computing.

5.2.3 Microwave photonics

The utilization of the optical domain for microwave generation, manipulation, and measurement, which is known as microwave photonics, has attracted extensive research interests due to the inherent abundance of bandwidth optical devices^[352]. Microcomb-based microwave photonic applications mainly focus on two functions: low noise microwave generation and multi-tap signal processing.

1) Low-noise microwave generation

By direct detection of a free-running microcomb, a high-purity microwave can be generated from a soliton pulse. Such pure-optical solution has been demonstrated in several platforms, with the repetition rate ranging from tens to hundreds of GHz level^[44,229,353], as shown in Table 9. Despite the absence of a locking regime, these high- Q microresonators enable a low-noise microwave generation with absolute single-sideband (SSB) phase noise power spectra density lower than -110 dBc/Hz at 10 kHz. On top of that, Yi *et al.* find that the nonlinear behavior of single-mode dispersive waves can be used to further suppress the repetition rate noise^[74]. With adequate pump detuning, the coupling of pump-laser frequency noise into the repetition rate could be minimized.

Achieving a low-noise microwave oscillation with higher performance requires external active feedback for thermal drift and actuation correction. Approaches including microwave injection locking^[301], optical self-injection locking^[140], fiber-photonics stabilization^[295], Kerr-induced synchronization^[80], and optical frequency division (OFD)^[42,354] are proposed for the microwave purification. Microwave injection locking is adapted in a 14 GHz-MgF₂ microcomb to discipline the soliton by creating an intracavity potential gradient^[301]. The self-purifying mechanism in a soliton pulse reduces the RF tone phase noise by

nearly 30 dB at 10 kHz offset frequency. A mode-locked Kerr comb in an ultra-low-loss 5 GHz SiN microresonator exhibits phase noise of -114 dBc/Hz^[140]. A DFB laser is injection-locked to this high- Q ($>10^8$) resonator, resulting in an extraordinarily narrowed linewidth. This leads to generating a dark-pulse-shaped coherent comb generated with excellent stability. Repetition rate stabilization could also be achieved by fiber photonics. The generation of a low-phase-noise 22 GHz microwave signal is demonstrated using a kilometers-long fiber delay line as a timing reference^[295]. The phase noise PSD of this fiber-stabilized microcomb is around -125 dBc/Hz, which shows one of the best noise performances without atomic locking.

With the optical frequency division technique, the stability of an ultra-low-noise laser could be transferred to the repetition rate. Recently, such an approach has been adopted in soliton microcombs, with the division operation performed in either the electrical^[354] or optical^[42] domain. A simplified OFD on a microcomb is performed via electrically canceling the comb phase noise and providing division of the ultrastable pump laser frequency to the microwave domain, with an adequate manipulation and combination of signals^[354]. The phase noise of the 14 GHz repetition rate output is below -135 dBc/Hz at 10 kHz Fourier frequency. A more common approach to achieve optical frequency division is locking two comb lines to precise optical references and reading out the output frequency from the repetition rate beat note^[42,355]. In Ref. [42], two comb lines, including the pump laser, are stabilized to rubidium frequency references separated by 3.5 THz, with a division factor of 108. More recently, microcomb OFD in highly integrated form has been demonstrated^[355,356]. Employing a 4 mm long ultra-low-loss SiN coil cavity as an optical reference, two lasers are stabilized and thereafter locked to a SiN soliton microcomb. Optically-electrically converted by a high-speed flip-chip bonded charge-compensated modified uni-travelling carrier photodiode, a record low 100 GHz phase noise of -114 dBc/Hz at 10 kHz offset frequency has been reached^[355]. In the meantime, stabilized self-injection-locked integrated lasers are used to lock the dark soliton microcomb in thin-film SiN. Such a system achieved a purified 20 GHz microwave with unprecedented absolute phase noise of -135 dBc/Hz at 10 kHz offset in integrated photonics^[355]. To reduce the system cost and complexity, a single-laser-based all-optical OFD is proposed by synchronizing two distinct nonlinear states, optical parameter oscillator (OPO) and soliton microcomb^[357]. The inherent stability of OPO is therefore transferred to a microwave state with -114 and -128 dBc/Hz at 10 kHz offset for the 227 and 16 GHz. These works, co-published recently, show the state-of-the-art performance in integrated-photonics-assisted microwave generation.

Moreover, Kerr-induced synchronization offers passive and electronics-free stabilization of a microcomb soliton to an external reference laser^[80]. The joint injection of the pump and reference laser leads to an optically captured comb line during the Kerr nonlinear dynamic so that the repetition rate can be tuned and its stability can be inherited from the reference through the OFD process. This novel approach marks an important step toward achieving power-efficient and architecturally simplified ultra-stable microwave generation.

2) Multi-tap signal processing

In addition to microwave generation, the parallel nature of microcombs allows for multi-tap signal processing, also known as the transversal filtering method, and relevant research

has been initiated in various areas. These include signal integration^[363], differentiation^[362], Hilbert transformation^[361,365], arbitrary waveform generation^[364,366], channelizing^[359,367], reconfigurable filtering^[43,53,358,368], beam forming^[360,369], and frequency conversion^[370], as shown in Fig. 33. Each application takes advantage of the microcomb's ability to process wideband RF signals simultaneously, thereafter processing each carrier's intensity, phase, or time delay for a specific function, opening up possibilities for more complex and versatile signal processing architectures.

One of the earliest demonstrations of microwave photonic processing using a microcomb involved the implementation of radio-frequency filters. In 2014, Xue *et al.* conducted a study on a programmable microwave photonic filter using a multi-tap delay line scheme^[43], where the RF signal is replicated across each comb-based optical carrier and subsequently manipulated in both the frequency and time domains to achieve the desired frequency response. Using a silicon nitride (SiN) microcomb paired with a commercial Waveshaper for spectral shaping, the optical carriers with a 230 GHz channel spacing are programmatically adjusted. This setup results in an RF transfer function that offers flexible frequency tunability and a flat-top characteristic, enhancing the performance and adaptability of the system for various applications. A tighter FSR can provide more taps, with a Hydex microcomb achieving up to 80 taps within the C-band. This configuration has demonstrated a high out-of-band rejection of up to 48.9 dB, featuring a tunable center frequency and 3 dB bandwidth^[358]. With advanced silicon photonic techniques, it is possible to implement not only microcombs but also other essential components such as modulators, true-time delay lines, and line-by-line shapers monolithically^[53]. This integration demonstrates the potential for achieving a high level of integration in RF processing for complex signal manipulation. Besides, one alternative for line-by-line shaping-free RF filters can be achieved by directly controlling the soliton state of the microcomb^[368]. By adjusting the pump power and frequency detuning, the mode spacing and spectral profile of the microcomb can be altered. This adjustment results in a tunable filter with variable frequency repetition and center frequency.

Mathematical operations can also be realized in this multi-tap delay line configuration, since its transfer function is given by

$$H(\omega) = \sum_{n=0}^{N-1} h(n)e^{-j\omega nT}. \quad (27)$$

Therefore, any arbitrary desired operation can be tailored by setting the appropriate time delay T and tap coefficients $h(n)$, enabling precise customization of signal processing tasks. For signal integration, the operation can be imitated via a discrete time-spectrum convolution operation between the RF input and the flattened microcomb^[363]. A large integration time window of 6.8 ns with time resolution as fast as 84 ps is realized. For the signal differentiator, the corresponding tap coefficient could be calculated based on the Remez algorithm^[362], in which way the first-, second-, and third-order intensity differentiator could be realized. Similarly, a band-limited Hilbert transformer can be realized using a transversal filtering method, where the tap coefficients are set to a hyperbolic function^[365]. Further, a fractional Hilbert transformer with tunable fractional order can be obtained with an operation bandwidth of ~ 16 GHz with root

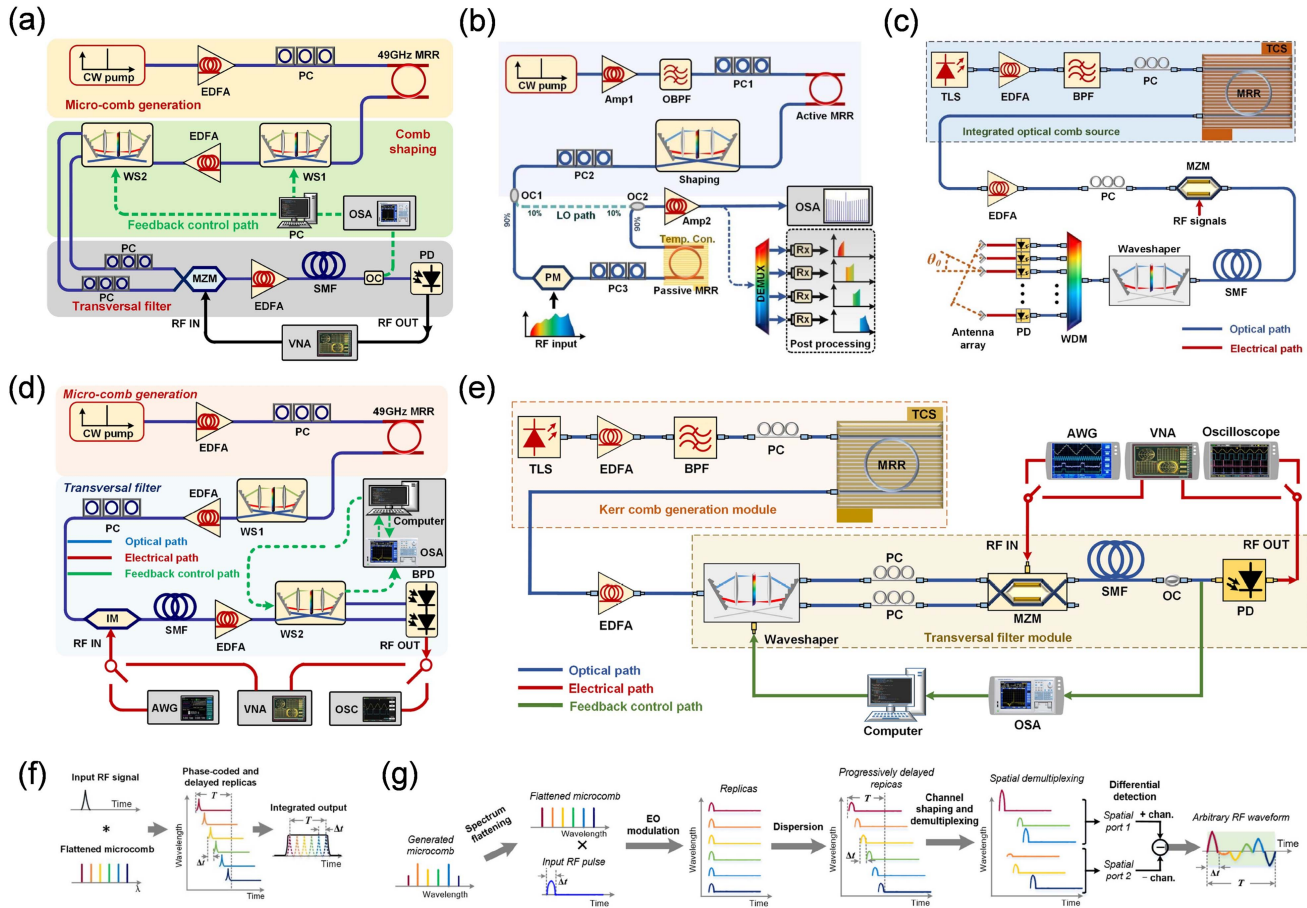


Fig. 33 Microcomb-based microwave processing. (a) Reconfigurable filter^[358]. (b) Channelizer^[359]. (c) Beam former^[360]. (d) Hilbert transformer^[361]. (e) Differentiator^[362]. (f) Integrator^[363]. (g) Arbitrary waveform generator^[364].

mean square errors (RMSEs) under 3%^[361]. The number of taps, which corresponds to up to 17 usable comb lines, is crucial for the accuracy of the computation results.

Photonic RF arbitrary waveform generation could offer high-bandwidth signals with low noise that are difficult to obtain with pure electronic devices. Utilizing a microcomb, arbitrary waveforms can be synthesized both in time and frequency domains^[364,366]. In Ref. [364], Tan *et al.* achieved square waveforms with tunable duty cycles from 10% to 90% and a sawtooth waveform with tunable slope ratios from 10% to 90%. The seed signal is an RF pulse signal whose duration time is related to the dispersive time delay between the comb lines. In Ref. [366], Wang *et al.* demonstrated a microcomb-based Fourier synthesis AWG. The frequency domain of the desired signal is imitated at the optical domain and then down-converted to the baseband via a dual-comb photo mixing configuration. The system is more portable to be integrated since there is no need for the deployment of a long dispersive delay line, which is lossy on-chip.

Microwave beamforming interferes with electromagnetic waves from multi-paths to control the beam patterns in free space, where microcombs are promising candidates. A microcomb acts as the multiwavelength source in a true time delay technique of beamforming, where a dispersive medium offers a time delay between adjacent channels. Therefore, beam steering could be achieved either by changing the physical length of

the dispersive medium^[369] or just by selecting the specific channels with a separation index of m ^[360]. Both of the solutions have been demonstrated. With over 80 comb lines available, the m is able to vary from 1 to 15. Therefore, a large tuning range from -69.7° to 72.9° can be achieved^[360]. In Ref. [369], a programmable dispersive element is built with commercial 2×2 optical switches and standard single-mode fibers. Within 21 comb lines, a 16-step dispersive delay line could offer a beam scanning range of $\pm 60^\circ$. Such a delay scheme is also free of the beam-squint problem within tens of GHz operation bandwidth, where the system holds a consistent beam direction.

RF channelization splits broadband microwave signals into narrow slices for parallel baseband processing. In Ref. [359], a microcomb-based RF channelizer consists of an active microcomb generator and a passive microring filter connected serially. The mode difference between the two devices, namely, the Vernier effect, determines the sequential frequency shift of each channel. A spectral slice resolution of 1.04 GHz was experimentally demonstrated with about 19 GHz operation bandwidth. Moreover, by utilizing dual-polarization states, the channelized spectral segments and the RF instantaneous bandwidth could be doubled^[367].

Besides, a microwave frequency converter could be performed by utilizing the frequency relationship between microcomb mode spacing and the applied RF frequency:

$$\omega_{\text{IF}} = \omega_{\text{LO}} \pm \omega_{\text{RF}}. \quad (28)$$

Such configuration achieves a ratio of -6.8 dB between output radio-frequency power and intermediate frequency power and a spurious suppression ratio of >43.5 dB^[370], showing the ability to realize a low-cost, compact footprint frequency converter.

5.3 Chaotic-Based Applications

Chaos, for its random behavior, has exhibited various applications in the field of safety communications, sensing, and high-performance computation during decision-making. Just as parallel coherence in solitons, a microcomb can also offer parallel chaos in the optical domain. This well-known chaotic comb regime is located within the blue detuning of the microresonator resonance, showing relatively high conversion efficiency and thermal stability. To validate the availability for real-world applications of chaotic microcombs, Shen *et al.* first characterize the intra and inter-channel chaotic properties. The results show considerable chaotic independence except for the comb pair symmetrically located to the pump laser, which verified that half a side of the microcomb could serve as an ideal parallel optical chaotic source.

This newly emerging technique has been implemented in a series of novel scenarios including random-bit generation (RBG)^[55,372], decision-making, and chaotic LiDAR^[54,371,373,374], as illustrated in Fig. 34. Compared to its electronic and optical counterparts, such as nonlinear ASICs and chaotic lasers with feedback loops, a chaotic microcomb offers a larger chaotic bandwidth while maintaining a simpler system architecture. The system only includes a pump laser and a nonlinear microresonator, and the chaotic bandwidth of the signal is highly related to the material nonlinearity. Employing a high-nonlinearity AlGaAsOI platform, a chaotic comb with 10 dB bandwidth of up to 5.6 GHz is demonstrated, which supports single-channel random bit generation rate of up to 120 Gbps and aggregation

rate of 3.84 Tbps by a dual-comb configuration^[55]. To achieve a higher signal channel rate, Li *et al.* performed 16-bit ADC sampling after injecting multiple comb lines, rather than just a single comb line, into the detection channel, resulting in a 320 Gbps generation rate in each channel^[372]. Moreover, such a strategy has shown its strength in optical computation by accelerating the decision-making of multi-armed bandit problems.

Recently, parallel chaos has also been used to enable random modulation continuous wave (RMCW) LiDAR^[54], benefiting from its inherent immunity to inter- and intra-interference. For multi-channel LiDAR systems, a critical challenge is channel congestion, which occurs when light channels overlap in the time or frequency domain, making it difficult to extract the corresponding echo signals from interference. A parallel chaotic microcomb solves this problem naturally since every comb line has its special temporal features. Thereby, a particular channel can be selected via cross-correlation. Such parallel chaotic LiDAR demonstrates centimeter-scale resolution and millimeter accuracy in both SiN^[371] and AlGaAsOI^[54] platforms. Further performance improvements have been studied for higher frame rates and longer detection ranges in parallel chaotic LiDAR. By adopting 2D spatial dispersion with a virtually imaged phased array and a diffraction grating, inertia-free ranging has been demonstrated^[373]. The continuous wave chaotic microcomb can also be transformed into a pulsed microcomb through an acousto-optic modulator, enabling a changeable duty cycle for higher peak power amplification^[374]. Such a scheme creates a great balance between human-eye safety requirements and ranging distance.

5.4 Advanced Minimized Systems

Despite the tremendous progress in microcomb-based applications mentioned above, most of these system-level demonstrations still rely on large amounts of bulky components. In this context, even though an integrated microcomb or heterogeneous laser soliton is used for light source generation, the rest of the

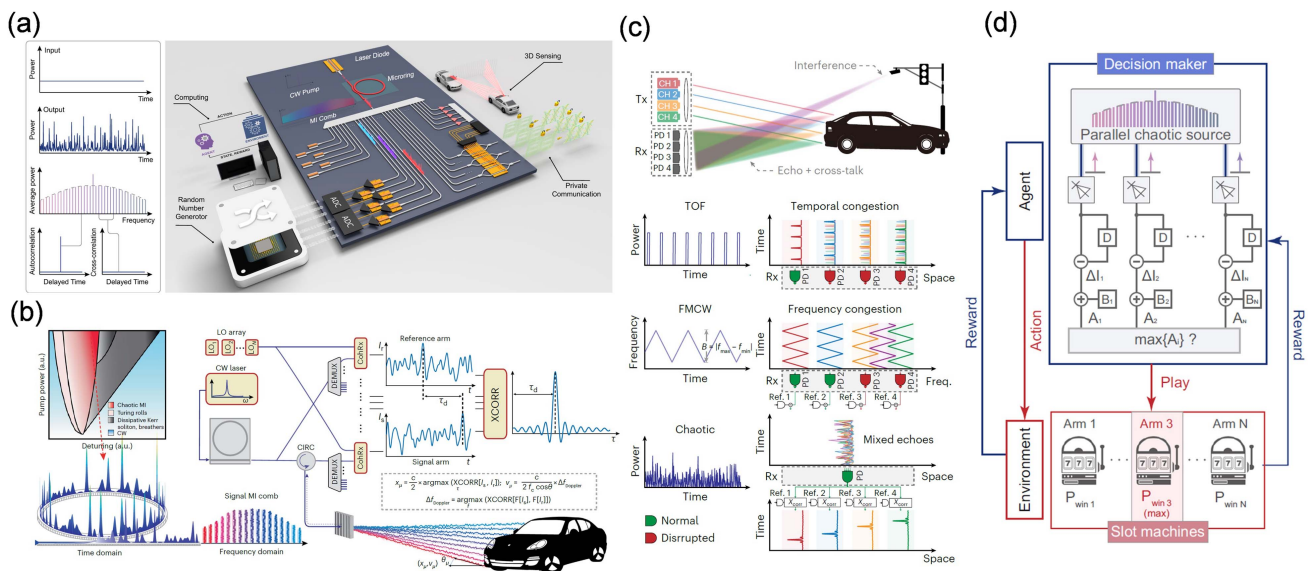


Fig. 34 Microcomb-based chaotic applications. (a) Schematic of chaotic microcomb and its applications. (b) Chaotic heterodyne LiDAR^[371]. (c) Chaotic direct-detection LiDAR for interference-free^[54]. (d) Chaotic microcomb-based decision maker^[55].

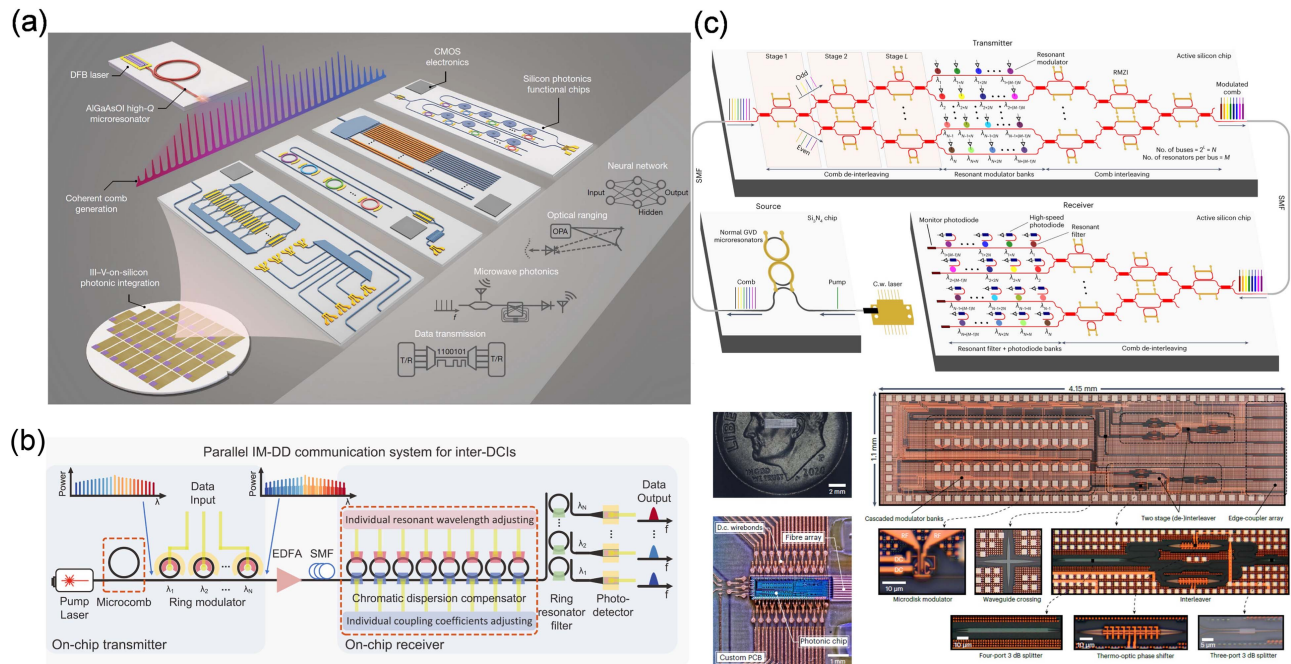


Fig. 35 Highly integrated microcomb-based on-chip systems. (a) Schematic of microcomb-driven silicon photonic systems^[53]. (b) Integrated chromatic dispersion compensator^[375]. (c) 32-channel microcomb-enabled silicon photonic transmitter^[376].

system remains large and power-hungry, which undermines the potential benefits of integrated photonics.

To solve this problem, one alternative is combining silicon photonics, which can provide almost all essential optoelectronic functions (e.g. modulation, photodetection, wavelength, and polarization division multiplexing) monolithically with a standard commercialized fabrication process, as shown in Fig. 35. The first demonstration of bridging these two fields was presented in our previous work, where a dark-pulse microcomb served as a multi-wavelength light source, separately driving a silicon photonic data link and a multi-tap microwave photonic filtering system^[53]. An aggregation transmission rate of 2 Tbps is achieved, and the configurable microwave photonic filter exhibits tens of microsecond level tunability. To further leverage the integration level, the on-chip wavelength (de) multiplexing devices were demonstrated, consisting of two-stage (i.e. coarse and fine) wavelength selective elements enabling 32-channel 16 Gbps error-free parallel data transmission where silicon-microresonator-based electro-optical modulators are employed for system size reduction^[376]. More recently, with a silicon photonic configurable microring-resonator-based chromatic dispersion compensator, the distance of soliton-based data transmission could reach over 20 km with an aggregate line rate of 1.68 Tbps^[375]. The passive equalization on-chip also decreases the power consumption of microcomb-driven data links by around six times. Apart from communication-related systems, other applications such as optical computing^[346] and optical frequency synthesizers^[46], as mentioned in the previous section, demonstrate efforts toward system miniaturization through the hybrid integration of multiple functional photonic circuits. The recent emergence of those minimized microcomb systems marks a significant step toward achieving highly scalable and multifunctional systems on a chip.

6 Discussion and Conclusion

The concept of microcombs originated from the idea of a miniaturized optical frequency comb for the optical atomic clock^[42]. Since the first observation of the microcomb in a toroid microcavity in 2007^[70], the goal of achieving a fully integrated optical frequency comb system on-chip has driven significant advances in integrated photonics^[86]. With improved fabrication techniques, various integrated platforms^[17,19,158,177,377], featuring diverse properties, have been developed to cover different optical bands. The quality factor of an integrated microcavity^[85,140] can now exceed 10^8 , nearing the material absorption limit. Lasers, the critical devices for microcomb generation, can also be integrated with microcavities on a single chip^[86,238]. Based on these advanced chips, mode-locked microcombs can be generated under different conditions, with the development of theory and design methods^[11,71,72,262], even under turnkey operation^[77]. These breakthroughs bring us closer to realizing a fully integrated microcomb system where both the repetition rate and the CEO frequency are detected and stabilized^[206,307]. Beyond optical atomic clocks^[34], microcomb technology has found applications in numerous fields, including metrology^[42], precision sensing^[36,323], biological imaging^[330], high-capacity communications^[338], and high-speed data processing^[51]. The original vision is now becoming a reality—and more.

For the fabrication of microcombs, it is fundamental to develop integrated devices, especially the microcavity and the pump laser. Since the realization of microcombs, the microcavity structures have been gradually miniaturized—from microspheres^[139] and microtoroids^[82] to microrings^[225], which are fabricated with standard planar processes. Microcomb generation has expanded into a variety of material platforms, ranging from the initial silicon dioxide^[70], metal fluoride^[378] to silicon

nitride^[17], lithium niobate^[23], and other material platforms. This has extended the operational bandwidth of microcombs beyond the traditional communication band, spanning from the visible^[159] to mid-infrared regions^[123], enabling various applications. Looking through different platforms, it is interesting to find that materials with higher nonlinearity tend to feature a larger cut-off wavelength, limiting their application for short-wavelength bands. For most cases, silicon nitride^[214] is the most common integrated optical nonlinear platform for visible or telecom bands, largely due to its mature fabrication process with high quality factor^[85,87]. While for long-wavelength bands, it is hard to identify a definitive platform, especially considering the absorption in these bands of silica^[201], which is commonly used as a cladding material in integrated optics. The development of high-quality-factor microcavities and different material platforms never stops, as for the integration of pump lasers, semiconductor laser diodes with moderate output power^[138] can be used as the pump light for microcavities with ultrahigh quality factors^[85] or high optical nonlinearity^[266]. Hybrid integrated microcomb modules have been demonstrated with butt coupling^[77], photonics wire bonding^[226], or other advanced packaging methods. Further, single-chip microcombs have been demonstrated by integrating the III–V laser diodes with the high-quality-factor microcavity through the heterogenous integration technology^[86,241]. Looking forward, monolithic integration of laser diodes with the microcavity is expected for microcomb generation, driven by advancements in quantum dot laser diode fabrication^[248]. The pursuit of higher-power integrated lasers remains a key objective, especially for achieving microcombs with broader spectral bandwidths and a greater number of comb lines^[156,206,305].

For the theory of microcombs, most research is based on the nonlinear Schrödinger equation^[91], which is widely used to describe optical field evolution in nonlinear media. Several equations, such as the coupled mode equations^[111], the Ikeda map^[120], and the LLE^[93], have been developed for the explanation and simulation of microcombs. Extended models with additional factors, such as photon-phonon interaction^[32], inter-mode interaction^[98], and thermal-optic interaction^[122], provide a more comprehensive description of the complex multi-field evolution processes in microcavities. Assisted with mature numerical methods such as split-step Fourier methods^[91] and Runge–Kutta method^[122], researchers can now obtain accurate and computational-friendly solutions to these complex equations. These theoretical models and numerical tools enable not only the explanation of experimental results but also the prediction of new phenomena. For example, the bright soliton in a microcavity was first predicted in theory and then proved in experiment^[11]. Over the last decade, significant progress has been made in uncovering intracavity dynamics under various conditions, leading to the discovery of several microcomb states, such as bright solitons^[11], dark pulses^[72], soliton crystals^[102], soliton breathers^[100], and Stokes solitons^[31]. The noise sources in microcomb systems are now well understood^[71,288,289]. Recently, microcombs in hybrid cavities and coupled cavity systems have gained attention for their unique properties, such as turnkey generation^[77], super-high conversion efficiency^[76], etc. In general, theoretical advancements continue to illuminate microcomb dynamics and guide the future development of microcomb technology.

For the design of microcombs, an ideal microcomb should simultaneously exhibit high conversion efficiency^[76], a flat^[116]

and broad^[225] spectrum, and low noise^[140]. However, these objectives often conflict with one another. For example, among different microcomb states, dark pulses theoretically offer a high conversion efficiency of over 50%^[277], while their spectra are narrow and irregular. In contrast, bright solitons produce flat and broad spectra. The conversion efficiency is limited to around 1% and decreases as the number of comb lines increases^[283]. Fortunately, diverse design methods have been developed to approach the ideal microcomb. Dispersion engineering including waveguide structure designing^[225], inter-mode coupling^[267], coupled microrings^[68], and photonic crystal microrings^[65] has enabled flexible spectrum design. Flat microcombs have been realized in experiments with the joint design of dissipation and dispersion conditions^[116]. Based on different pumping strategies and dispersion designs, the conversion efficiency of the single soliton has reached 54%^[67] in experiment and 94%^[63] in theory, which would have been unimaginable just five years ago. High-coherence microcombs can be obtained with a self-injection locking process^[140] or operation at the quiet point^[176]. Stabilized microcombs are now widely applied in optical clocks^[34] and spectroscopy^[314]. While the ideal microcomb remains out of reach, significant progress has been made toward its realization.

For the application of microcombs, the special time-frequency characteristic makes microcombs powerful tools for precise detection^[323] and stable signal generation^[44] in both the time domain and frequency domain. Inspired by previous research based on traditional optical frequency combs^[1], microcomb technology has been employed in applications such as optical atomic clocks^[42], optical frequency synthesizers^[46], astrocombs^[47], and microwave^[229] generation, where stable time and frequency properties are critical. In addition, the microcomb can serve as broadband multiwavelength sources, making them ideal for applications like optical coherence tomography^[48] and spectroscopy^[36]. By utilizing individual comb lines as signal carriers, microcombs enable parallel optical communication^[338] and multi-tap microwave signal processing^[43]. The aforementioned applications all require the high coherence of microcombs, where the mode-locked states are preferred. Recently, a chaotic microcomb^[55], another common microcomb state, has been explored for its potential in parallel optical chaotic signal distribution. Chaotic microcombs have already been employed in applications like parallel chaotic LiDAR^[54,371], random number generation^[55,372], and large-scale optical decision-making^[55]. It is important to note that for a fully integrated or miniaturized microcomb-based system^[53], all components must be integrated on a chip. In addition to advancements in microcomb fabrication, platforms such as silicon photonics^[198] and integrated III–V technologies^[231] have been enhanced with diverse functionalities like wavelength division^[346], amplitude and phase tuning^[86], and optical signal detection^[53]. The integration of these technologies paves the way for the development of fully integrated optoelectronic systems in the future.

Acknowledgments

This work was supported by the National Key Research and Development Program of China (No. 2022YFB2803700), the National Natural Science Foundation of China (Nos. 62001010, 62322501, 12204021, and 62327811), and the China National Postdoctoral Program for Innovative Talents (No. BX20240014).

References

1. T. Fortier and E. Baumann, "20 years of developments in optical frequency comb technology and applications," *Commun. Phys.* **2**, 153 (2019).
2. F. R. Giorgetta *et al.*, "Optical two-way time and frequency transfer over free space," *Nat. Photonics* **7**, 434 (2013).
3. T. M. Fortier *et al.*, "Carrier-envelope phase-controlled quantum interference of injected photocurrents in semiconductors," *Phys. Rev. Lett.* **92**, 147403 (2004).
4. T. Rosenband *et al.*, "Frequency ratio of Al⁺ and Hg⁺ single-ion optical clocks; metrology at the 17th decimal place," *Science* **319**, 1808 (2008).
5. S. A. Diddams, L. Hollberg, and V. Mbele, "Molecular fingerprinting with the resolved modes of a femtosecond laser frequency comb," *Nature* **445**, 627 (2007).
6. M. T. Murphy *et al.*, "High-precision wavelength calibration of astronomical spectrographs with laser frequency combs," *Mon. Not. R. Astron. Soc.* **380**, 839 (2007).
7. K. J. Vahala, "Optical microcavities," *Nature* **424**, 839 (2003).
8. T. Kippenberg, S. Spillane, and K. Vahala, "Kerr-nonlinearity optical parametric oscillation in an ultrahigh-Q toroid microcavity," *Phys. Rev. Lett.* **93**, 083904 (2004).
9. T. J. Kippenberg *et al.*, "Dissipative Kerr solitons in optical microresonators," *Science* **361**, eaan8083 (2018).
10. Y. K. Chembo and C. R. Menyuk, "Spatiotemporal Lugiato-Lefever formalism for Kerr-comb generation in whispering-gallery-mode resonators," *Phys. Rev. A* **87**, 053852 (2013).
11. T. Herr *et al.*, "Temporal solitons in optical microresonators," *Nat. Photonics* **8**, 145 (2014).
12. M. W. Puckett *et al.*, "422 million intrinsic quality factor planar integrated all-waveguide resonator with sub-MHz linewidth," *Nat. Commun.* **12**, 934 (2021).
13. D. K. Armani *et al.*, "Ultra-high-Q toroid microcavity on a chip," *Nature* **421**, 925 (2003).
14. I. S. Grudinin, L. Baumgartel, and N. Yu, "Frequency comb from a microresonator with engineered spectrum," *Opt. Express* **20**, 6604 (2012).
15. M. Ferrera *et al.*, "Low-power continuous-wave nonlinear optics in doped silica glass integrated waveguide structures," *Nat. Photonics* **2**, 737 (2008).
16. A. C. Turner *et al.*, "Ultra-low power parametric frequency conversion in a silicon microring resonator," *Opt. Express* **16**, 4881 (2008).
17. J. S. Levy *et al.*, "CMOS-compatible multiple-wavelength oscillator for on-chip optical interconnects," *Nat. Photonics* **4**, 37 (2010).
18. H. Jung *et al.*, "Optical frequency comb generation from aluminum nitride microring resonator," *Opt. Lett.* **38**, 2810 (2013).
19. B. J. M. Hausmann *et al.*, "Diamond nonlinear photonics," *Nat. Photonics* **8**, 369 (2014).
20. C.-L. Wu *et al.*, "Low-loss and high-Q Ta₂O₅ based micro-ring resonator with inverse taper structure," *Opt. Express* **23**, 26268 (2015).
21. M. Pu *et al.*, "Efficient frequency comb generation in AlGaAs-on-insulator," *Optica* **3**, 823 (2016).
22. Q. Du *et al.*, "Low-loss photonic device in Ge-Sb-S chalcogenide glass," *Opt. Lett.* **41**, 3090 (2016).
23. M. Zhang *et al.*, "Monolithic ultra-high-Q lithium niobate microring resonator," *Optica* **4**, 1536 (2017).
24. D. J. Wilson *et al.*, "Integrated gallium phosphide nonlinear photonics," *Nat. Photonics* **14**, 57 (2020).
25. M. A. Guidry *et al.*, "Optical parametric oscillation in silicon carbide nanophotonics," *Optica* **7**, 1139 (2020).
26. C. Wang *et al.*, "Lithium tantalate photonic integrated circuits for volume manufacturing," *Nature* **629**, 784 (2024).
27. X. Xue *et al.*, "Mode-locked dark pulse Kerr combs in normal-dispersion microresonators," *Nat. Photonics* **9**, 594 (2015).
28. M. Yu *et al.*, "Breather soliton dynamics in microresonators," *Nat. Commun.* **8**, 14569 (2017).
29. D. C. Cole *et al.*, "Soliton crystals in Kerr resonators," *Nat. Photonics* **11**, 671 (2017).
30. W. Weng *et al.*, "Heteronuclear soliton molecules in optical microresonators," *Nat. Commun.* **11**, 2402 (2020).
31. Q.-F. Yang *et al.*, "Stokes solitons in optical microcavities," *Nat. Phys.* **13**, 53 (2017).
32. Y. Bai *et al.*, "Brillouin-Kerr soliton frequency combs in an optical microresonator," *Phys. Rev. Lett.* **126**, 063901 (2021).
33. H. Bao *et al.*, "Laser cavity-soliton microcombs," *Nat. Photonics* **13**, 384 (2019).
34. Z. L. Newman *et al.*, "Architecture for the photonic integration of an optical atomic clock," *Optica* **6**, 680 (2019).
35. P. Trocha *et al.*, "Ultrafast optical ranging using microresonator soliton frequency combs," *Science* **359**, 887 (2018).
36. M.-G. Suh *et al.*, "Microresonator soliton dual-comb spectroscopy," *Science* **354**, 600 (2016).
37. J. Pfeifle *et al.*, "Coherent terabit communications with microresonator Kerr frequency combs," *Nat. Photonics* **8**, 375 (2014).
38. J. Riemensberger *et al.*, "Massively parallel coherent laser ranging using a soliton microcomb," *Nature* **581**, 164 (2020).
39. J. Feldmann *et al.*, "Parallel convolutional processing using an integrated photonic tensor core," *Nature* **589**, 52 (2021).
40. B. Shen *et al.*, "Harnessing microcomb-based parallel chaos for random number generation and optical decision making," *Nat. Commun.* **14**, 4590 (2023).
41. H. Shu *et al.*, "Microcomb-driven silicon photonic systems," *Nature* **605**, 457 (2022).
42. S. B. Papp *et al.*, "Microresonator frequency comb optical clock," *Optica* **1**, 10 (2014).
43. X. Xue *et al.*, "Programmable single-bandpass photonic RF filter based on Kerr comb from a microring," *J. Lightwave Technol.* **32**, 3557 (2014).
44. W. Liang *et al.*, "High spectral purity Kerr frequency comb radio frequency photonic oscillator," *Nat. Commun.* **6**, 7957 (2015).
45. P. Del'Haye *et al.*, "Phase-coherent microwave-to-optical link with a self-referenced microcomb," *Nat. Photonics* **10**, 516 (2016).
46. D. T. Spencer *et al.*, "An optical-frequency synthesizer using integrated photonics," *Nature* **557**, 81 (2018).
47. M.-G. Suh *et al.*, "Searching for exoplanets using a microresonator astrocomb," *Nat. Photonics* **13**, 25 (2019).
48. X. Ji *et al.*, "Chip-based frequency comb sources for optical coherence tomography," *Opt. Express* **27**, 19896 (2019).
49. J. Riemensberger *et al.*, "Massively parallel coherent laser ranging using a soliton microcomb," *Nature* **581**, 164 (2020).
50. C. Bao *et al.*, "Architecture for microcomb-based GHz-mid-infrared dual-comb spectroscopy," *Nat. Commun.* **12**, 6573 (2021).
51. X. Xu *et al.*, "11 TOPS photonic convolutional accelerator for optical neural networks," *Nature* **589**, 44 (2021).
52. W. Shao *et al.*, "Terabit FSO communication based on a soliton microcomb," *Photonics Res.* **10**, 2802 (2022).
53. H. Shu *et al.*, "Microcomb-driven silicon photonic systems," *Nature* **605**, 457 (2022).
54. R. Chen *et al.*, "Breaking the temporal and frequency congestion of LiDAR by parallel chaos," *Nat. Photonics* **17**, 306 (2023).
55. B. Shen *et al.*, "Harnessing microcomb-based parallel chaos for random number generation and optical decision making," *Nat. Commun.* **14**, 4592 (2023).
56. X. Zhang *et al.*, "High-coherence parallelization in integrated photonics," *Nat. Commun.* **15**, 7892 (2024).
57. P. Del'Haye *et al.*, "Octave spanning tunable frequency comb from a microresonator," *Phys. Rev. Lett.* **107**, 063901 (2011).
58. Y. Liu *et al.*, "Investigation of mode coupling in normal-dispersion silicon nitride microresonators for Kerr frequency comb generation," *Optica* **1**, 137 (2014).

59. X. Xue *et al.*, “Normal-dispersion microcombs enabled by controllable mode interactions,” *Laser Photonics Rev.* **9**, L23 (2015).
60. B. Y. Kim *et al.*, “Turn-key, high-efficiency Kerr comb source,” *Opt. Lett.* **44**, 4475 (2019).
61. S. Kim *et al.*, “Dispersion engineering and frequency comb generation in thin silicon nitride concentric microresonators,” *Nat. Commun.* **8**, 372 (2017).
62. B. Stern *et al.*, “Battery-operated integrated frequency comb generator,” *Nature* **562**, 401 (2018).
63. X. Xue, X. Zheng, and B. Zhou, “Super-efficient temporal solitons in mutually coupled optical cavities,” *Nat. Photonics* **13**, 616 (2019).
64. Y. Li *et al.*, “Real-time transition dynamics and stability of chip-scale dispersion-managed frequency microcombs,” *Light Sci. Appl.* **9**, 52 (2020).
65. S.-P. Yu *et al.*, “Spontaneous pulse formation in edgeless photonic crystal resonators,” *Nat. Photonics* **15**, 461 (2021).
66. J. Li *et al.*, “The efficiency of pulse pumped soliton microcombs,” *Optica* **9**, 231 (2022).
67. O. B. Helgason *et al.*, “Surpassing the nonlinear conversion efficiency of soliton microcombs,” *Nat. Photonics* **17**, 992 (2023).
68. Q.-X. Ji *et al.*, “Multimodality integrated microresonators using the moiré speedup effect,” *Science* **383**, 1080 (2024).
69. E. Lucas *et al.*, “Tailoring microcombs with inverse-designed, meta-dispersion microresonators,” *Nat. Photonics* **17**, 943 (2023).
70. P. Del’Haye *et al.*, “Optical frequency comb generation from a monolithic microresonator,” *Nature* **450**, 1214 (2007).
71. T. Herr *et al.*, “Universal formation dynamics and noise of Kerr-frequency combs in microresonators,” *Nat. Photonics* **6**, 480 (2012).
72. X. Xue *et al.*, “Mode-locked dark pulse Kerr combs in normal-dispersion microresonators,” *Nat. Photonics* **9**, 594 (2015).
73. V. Brasch *et al.*, “Photonic chip-based optical frequency comb using soliton Cherenkov radiation,” *Science* **351**, 357 (2016).
74. X. Yi *et al.*, “Single-mode dispersive waves and soliton microcomb dynamics,” *Nat. Commun.* **8**, 14869 (2017).
75. J. K. Jang *et al.*, “Synchronization of coupled optical microresonators,” *Nat. Photonics* **12**, 688 (2018).
76. H. Bao *et al.*, “Laser cavity-soliton microcombs,” *Nat. Photonics* **13**, 384 (2019).
77. B. Shen *et al.*, “Integrated turnkey soliton microcombs,” *Nature* **582**, 365 (2020).
78. O. B. Helgason *et al.*, “Dissipative solitons in photonic molecules,” *Nat. Photonics* **15**, 305 (2021).
79. M. A. Guidry *et al.*, “Quantum optics of soliton microcombs,” *Nat. Photonics* **16**, 52 (2022).
80. G. Moille *et al.*, “Kerr-induced synchronization of a cavity soliton to an optical reference,” *Nature* **624**, 267 (2023).
81. J. Ling *et al.*, “Electrically empowered microcomb laser,” *Nat. Commun.* **15**, 4192 (2024).
82. D. K. Armani *et al.*, “Ultra-high-Q toroid microcavity on a chip,” *Nature* **421**, 925 (2003).
83. M. H. P. Pfeiffer *et al.*, “Ultra-smooth silicon nitride waveguides based on the Damascene reflow process: fabrication and loss origins,” *Optica* **5**, 884 (2018).
84. D. J. Wilson *et al.*, “Integrated gallium phosphide nonlinear photonics,” *Nat. Photonics* **14**, 57 (2020).
85. M. W. Puckett *et al.*, “422 Million intrinsic quality factor planar integrated all-waveguide resonator with sub-MHz linewidth,” *Nat. Commun.* **12**, 934 (2021).
86. C. Xiang *et al.*, “Laser soliton microcombs heterogeneously integrated on silicon,” *Science* **373**, 99 (2021).
87. Z. Ye *et al.*, “Foundry manufacturing of tight-confinement, dispersion-engineered, ultralow-loss silicon nitride photonic integrated circuits,” *Photonics Res.* **11**, 558 (2023).
88. C. Wang *et al.*, “Lithium tantalate photonic integrated circuits for volume manufacturing,” *Nature* **629**, 784 (2024).
89. T. J. Kippenberg, R. Holzwarth, and S. A. Diddams, “Microresonator-based optical frequency combs,” *Science* **332**, 555 (2011).
90. S. A. Diddams, K. Vahala, and T. Udem, “Optical frequency combs: coherently uniting the electromagnetic spectrum,” *Science* **369**, eaay3676 (2020).
91. G. P. Agrawal, *Nonlinear Science at the Dawn of the 21st Century 195-211* (Springer, 2000).
92. A. L. Gaeta, M. Lipson, and T. J. Kippenberg, “Photonic-chip-based frequency combs,” *Nat. Photonics* **13**, 158 (2019).
93. M. Haelterman, S. Trillo, and S. Wabnitz, “Dissipative modulation instability in a nonlinear dispersive ring cavity,” *Opt. Commun.* **91**, 401 (1992).
94. T. Hansson, D. Modotto, and S. Wabnitz, “Dynamics of the modulational instability in microresonator frequency combs,” *Phys. Rev. A* **88**, 023819 (2013).
95. M. Anderson *et al.*, “Observations of spatiotemporal instabilities of temporal cavity solitons,” *Optica* **3**, 1071 (2016).
96. T. Herr, M. L. Gorodetsky, and T. J. Kippenberg, “Dissipative Kerr solitons in optical microresonators,” in *Nonlinear optical cavity dynamics: from microresonators to fiber lasers* (2016), p. 129.
97. C. Bao *et al.*, “Observation of Fermi-Pasta-Ulam recurrence induced by breather solitons in an optical microresonator,” *Phys. Rev. Lett.* **117**, 163901 (2016).
98. H. Guo *et al.*, “Intermode breather solitons in optical microresonators,” *Phys. Rev. X* **7**, 041055 (2017).
99. E. Lucas *et al.*, “Breathing dissipative solitons in optical microresonators,” *Nat. Commun.* **8**, 736 (2017).
100. M. Yu *et al.*, “Breather soliton dynamics in microresonators,” *Nat. Commun.* **8**, 14569 (2017).
101. C. Bao *et al.*, “Observation of breathing dark pulses in normal dispersion optical microresonators,” *Phys. Rev. Lett.* **121**, 257401 (2018).
102. D. C. Cole *et al.*, “Soliton crystals in Kerr resonators,” *Nat. Photonics* **11**, 671 (2017).
103. B. C. Yao *et al.*, “Gate-tunable frequency combs in graphene-nitride microresonators,” *Nature* **558**, 410 (2018).
104. Y. He *et al.*, “Self-starting bi-chromatic LiNbO₃ soliton microcomb,” *Optica* **6**, 1138 (2019).
105. M. Karpov *et al.*, “Dynamics of soliton crystals in optical microresonators,” *Nat. Phys.* **15**, 1071 (2019).
106. Y. He *et al.*, “Perfect soliton crystals on demand,” *Laser Photonics Rev.* **14**, 1900339 (2020).
107. Z. Z. Lu *et al.*, “Synthesized soliton crystals,” *Nat. Commun.* **12**, 3179 (2021).
108. W. Weng *et al.*, “Heteronuclear soliton molecules in optical microresonators,” *Nat. Commun.* **11**, 2402 (2020).
109. M. Zhang *et al.*, “Strong interactions between solitons and background light in Brillouin-Kerr microcombs,” *Nat. Commun.* **15**, 1661 (2024).
110. M. Rowley *et al.*, “Self-emergence of robust solitons in a microcavity,” *Nature* **608**, 303 (2022).
111. Y. K. Chembo and N. Yu, “Modal expansion approach to optical-frequency-comb generation with monolithic whispering-gallery-mode resonators,” *Phys. Rev. A* **82**, 033801 (2010).
112. F. Leo *et al.*, “Dynamics of one-dimensional Kerr cavity solitons,” *Opt. Express* **21**, 9180 (2013).
113. N. Englebert *et al.*, “Parametrically driven Kerr cavity solitons,” *Nat. Photonics* **15**, 857 (2021).
114. G. Moille *et al.*, “Parametrically driven pure-Kerr temporal solitons in a chip-integrated microcavity,” *Nat. Photonics* **18**, 617 (2024).
115. A. W. Bruch *et al.*, “Pockels soliton microcomb,” *Nat. Photonics* **15**, 21 (2021).
116. X. Xue *et al.*, “Dispersion-less Kerr solitons in spectrally confined optical cavities,” *Light Sci. Appl.* **12**, 19 (2023).

117. I. H. Agha, Y. Okawachi, and A. L. Gaeta, "Theoretical and experimental investigation of broadband cascaded four-wave mixing in high-Q microspheres," *Opt. Express* **17**, 16209 (2009).
118. S. W. Huang *et al.*, "Mode-locked ultrashort pulse generation from on-chip normal dispersion microresonators," *Phys. Rev. Lett.* **114**, 053901 (2015).
119. Y. K. Chembo, D. V. Strekalov, and N. Yu, "Spectrum and dynamics of optical frequency combs generated with monolithic whispering gallery mode resonators," *Phys. Rev. Lett.* **104**, 103902 (2010).
120. T. Hansson and S. Wabnitz, "Dynamics of microresonator frequency comb generation: models and stability," *Nanophotonics* **5**, 231 (2016).
121. S. Coen *et al.*, "Modeling of octave-spanning Kerr frequency combs using a generalized mean-field Lugiato–Lefever model," *Opt. Lett.* **38**, 37 (2012).
122. H. Guo *et al.*, "Universal dynamics and deterministic switching of dissipative Kerr solitons in optical microresonators," *Nat. Phys.* **13**, 94 (2017).
123. M. Yu *et al.*, "Mode-locked mid-infrared frequency combs in a silicon microresonator," *Optica* **3**, 854 (2016).
124. V. Brasch *et al.*, "Bringing short-lived dissipative Kerr soliton states in microresonators into a steady state," *Opt. Express* **24**, 29312 (2016).
125. C. Bao *et al.*, "Direct soliton generation in microresonators," *Opt. Lett.* **42**, 2519 (2017).
126. J. R. Stone *et al.*, "Thermal and nonlinear dissipative-soliton dynamics in Kerr-microresonator frequency combs," *Phys. Rev. Lett.* **121**, 063902 (2018).
127. K. Liu *et al.*, "Mitigating fast thermal instability by engineered laser sweep in AlN soliton microcomb generation," *Photonics Res.* **11**, A10 (2023).
128. Z. Gong *et al.*, "High-fidelity cavity soliton generation in crystalline AlN micro-ring resonators," *Opt. Lett.* **43**, 4366 (2018).
129. M. H. Anderson *et al.*, "Photonic chip-based resonant supercontinuum via pulse-driven Kerr microresonator solitons," *Optica* **8**, 771 (2021).
130. W. Weng *et al.*, "Gain-switched semiconductor laser driven soliton microcombs," *Nat. Commun.* **12**, 1425 (2021).
131. E. Obrzud, S. Lecomte, and T. Herr, "Temporal solitons in microresonators driven by optical pulses," *Nat. Photonics* **11**, 600 (2017).
132. H. Zhou *et al.*, "Soliton bursts and deterministic dissipative Kerr soliton generation in auxiliary-assisted microcavities," *Light Sci. Appl.* **8**, 50 (2019).
133. Y. Geng *et al.*, "Enhancing the long-term stability of dissipative Kerr soliton microcomb," *Opt. Lett.* **45**, 5073 (2020).
134. H. Zheng *et al.*, "Programmable access to microresonator solitons with modulational sideband heating," *APL Photonics* **8**, 126110 (2023).
135. S. Zhang *et al.*, "Sub-milliwatt-level microresonator solitons with extended access range using an auxiliary laser," *Optica* **6**, 206 (2019).
136. Y. Zhao *et al.*, "Soliton burst and bi-directional switching in the platform with positive thermal-refractive coefficient using an auxiliary laser," *Laser Photonics Rev.* **15**, 2100264 (2021).
137. C. Joshi *et al.*, "Thermally controlled comb generation and soliton modelocking in microresonators," *Opt. Lett.* **41**, 2565 (2016).
138. A. S. Raja *et al.*, "Electrically pumped photonic integrated soliton microcomb," *Nat. Commun.* **10**, 680 (2019).
139. M. L. Gorodetsky, A. D. Pryamikov, and V. S. Ilchenko, "Rayleigh scattering in high-Q microspheres," *J. Opt. Soc. Am. B* **17**, 1051 (2000).
140. W. Jin *et al.*, "Hertz-linewidth semiconductor lasers using CMOS-ready ultra-high-Q microresonators," *Nat. Photonics* **15**, 346 (2021).
141. G. Lihachev *et al.*, "Platicon microcomb generation using laser self-injection locking," *Nat. Commun.* **13**, 1771 (2022).
142. B. Shen *et al.*, "Reliable intracavity reflection for self-injection locking lasers and microcomb generation," *Photonics Res.* **12**, A41 (2024).
143. X. Yi *et al.*, "Active capture and stabilization of temporal solitons in microresonators," *Opt. Lett.* **41**, 2037 (2016).
144. Q. Li *et al.*, "Stably accessing octave-spanning microresonator frequency combs in the soliton regime," *Optica* **4**, 193 (2017).
145. N. G. Pavlov *et al.*, "Narrow-linewidth lasing and soliton Kerr microcombs with ordinary laser diodes," *Nat. Photonics* **12**, 694 (2018).
146. A. Kovach *et al.*, "Emerging material systems for integrated optical Kerr frequency combs," *Adv. Opt. Photonics* **12**, 135 (2020).
147. C. Y. Wang *et al.*, "Mid-infrared optical frequency combs at 2.5 μm based on crystalline microresonators," *Nat. Commun.* **4**, 1345 (2013).
148. A. A. Savchenkov *et al.*, "Tunable optical frequency comb with a crystalline whispering gallery mode resonator," *Phys. Rev. Lett.* **101**, 093902 (2008).
149. G. Lin *et al.*, "Barium fluoride whispering-gallery-mode disk-resonator with one billion quality-factor," *Opt. Lett.* **39**, 6009 (2014).
150. R. Henriot *et al.*, "Kerr optical frequency comb generation in strontium fluoride whispering-gallery mode resonators with billion quality factor," *Opt. Lett.* **40**, 1567 (2015).
151. N. L. B. Sayson *et al.*, "Octave-spanning tunable parametric oscillation in crystalline Kerr microresonators," *Nat. Photonics* **13**, 701 (2019).
152. Y. Xuan *et al.*, "High-Q silicon nitride microresonators exhibiting low-power frequency comb initiation," *Optica* **3**, 1171 (2016).
153. T. C. Briles *et al.*, "Interlocking Kerr-microresonator frequency combs for microwave to optical synthesis," *Opt. Lett.* **43**, 2933 (2018).
154. C. Wang *et al.*, "High-Q microresonators on 4H-silicon-carbide-on-insulator platform for nonlinear photonics," *Light Sci. Appl.* **10**, 139 (2021).
155. H. Jung *et al.*, "Tantala Kerr nonlinear integrated photonics," *Optica* **8**, 811 (2021).
156. Y. Okawachi *et al.*, "Octave-spanning frequency comb generation in a silicon nitride chip," *Opt. Lett.* **36**, 3398 (2011).
157. L. Chang *et al.*, "Ultra-efficient frequency comb generation in AlGaAs-on-insulator microresonators," *Nat. Commun.* **11**, 1331 (2020).
158. L. Razzari *et al.*, "CMOS-compatible integrated optical hyperparametric oscillator," *Nat. Photonics* **4**, 41 (2010).
159. Y. Zhao *et al.*, "Visible nonlinear photonics via high-order-mode dispersion engineering," *Optica* **7**, 135 (2020).
160. A. G. Griffith *et al.*, "Silicon-chip mid-infrared frequency comb generation," *Nat. Commun.* **6**, 6299 (2015).
161. M. Zhang *et al.*, "Broadband electro-optic frequency comb generation in a lithium niobate microring resonator," *Nature* **568**, 373 (2019).
162. K. Schneider *et al.*, "Gallium phosphide-on-silicon dioxide photonic devices," *J. Lightwave Technol.* **36**, 2994 (2018).
163. R. Soref, "Mid-infrared photonics in silicon and germanium," *Nat. Photonics* **4**, 495 (2010).
164. X. Ji *et al.*, "Exploiting ultralow loss multimode waveguides for broadband frequency combs," *Laser Photonics Rev.* **15**, 2000353 (2021).
165. T. S. Tebeneva *et al.*, "Crystalline germanium high-Q microresonators for mid-IR," *Opt. Express* **32**, 15680 (2024).
166. R. Guo *et al.*, "Is Ge an excellent material for mid-IR Kerr frequency combs around 3- μm wavelengths?" *J. Lightwave Technol.* **40**, 2097 (2021).

167. X. Liu *et al.*, “Integrated high-Q crystalline AlN microresonators for broadband Kerr and Raman frequency combs,” *ACS Photonics* **5**, 1943 (2018).
168. Y. Zheng *et al.*, “Integrated gallium nitride nonlinear photonics,” *Laser Photonics Rev.* **16**, 2100071 (2022).
169. W. Xie *et al.*, “Ultrahigh-Q AlGaAs-on-insulator microresonators for integrated nonlinear photonics,” *Opt. Express* **28**, 32894 (2020).
170. D. Xia *et al.*, “Integrated chalcogenide photonics for microresonator soliton combs,” *Laser Photonics Rev.* **17**, 2200219 (2023).
171. I. S. Grudinin, V. S. Ilchenko, and L. Maleki, “Ultrahigh optical Q factors of crystalline resonators in the linear regime,” *Phys. Rev. A* **74**, 063806 (2006).
172. W. Liang *et al.*, “Miniature multioctave light source based on a monolithic microcavity,” *Optica* **2**, 40 (2015).
173. Z. Qu *et al.*, “Fabrication of an ultra-high quality MgF₂ microresonator for a single soliton comb generation,” *Opt. Express* **31**, 3005 (2023).
174. X. Yi *et al.*, “Soliton frequency comb at microwave rates in a high-Q silica microresonator,” *Optica* **2**, 1078 (2015).
175. M. Wang *et al.*, “Kerr frequency comb and stimulated Raman comb covering S plus C plus L plus U band based on a packaged silica spherical microcavity,” *J. Lightwave Technol.* **41**, 199 (2023).
176. L. Yao *et al.*, “Soliton microwave oscillators using oversized billion Q optical microresonators,” *Optica* **9**, 561 (2022).
177. H. Lee *et al.*, “Chemically etched ultrahigh-Q wedge-resonator on a silicon chip,” *Nat. Photonics* **6**, 369 (2012).
178. J. Li *et al.*, “Low-pump-power, low-phase-noise, and microwave to millimeter-wave repetition rate operation in microcombs,” *Phys. Rev. Lett.* **109**, 233901 (2012).
179. K. Y. Yang *et al.*, “Broadband dispersion-engineered microresonator on a chip,” *Nat. Photonics* **10**, 316 (2016).
180. K. Y. Yang *et al.*, “Bridging ultrahigh-Q devices and photonic circuits,” *Nat. Photonics* **12**, 297 (2018).
181. B. E. Little *et al.*, “Very high-order microring resonator filters for WDM applications,” *IEEE Photon. Technol. Lett.* **16**, 2263 (2004).
182. D. Duchesne *et al.*, “Efficient self-phase modulation in low loss, high index doped silica glass integrated waveguides,” *Opt. Express* **17**, 1865 (2009).
183. D. J. Moss *et al.*, “New CMOS-compatible platforms based on silicon nitride and Hydex for nonlinear optics,” *Nat. Photonics* **7**, 597 (2013).
184. C. Murray *et al.*, “Investigating the thermal robustness of soliton crystal microcombs,” *Opt. Express* **31**, 37749 (2023).
185. X. Ji *et al.*, “Ultra-low-loss on-chip resonators with sub-milliwatt parametric oscillation threshold,” *Optica* **4**, 619 (2017).
186. J. A. Smith *et al.*, “SiN foundry platform for high performance visible light integrated photonics,” *Opt. Mater. Express* **13**, 458 (2023).
187. Z. Ye *et al.*, “High-Q Si₃N₄ microresonators based on a subtractive processing for Kerr nonlinear optics,” *Opt. Express* **27**, 35719 (2019).
188. J. Hu *et al.*, “Photo-induced cascaded harmonic and comb generation in silicon nitride microresonators,” *Sci. Adv.* **8**, eadd8252 (2022).
189. A. Billat *et al.*, “Large second harmonic generation enhancement in Si₃N₄ waveguides by all-optically induced quasi-phase-matching,” *Nat. Commun.* **8**, 1016 (2017).
190. A. D. White *et al.*, “Integrated passive nonlinear optical isolators,” *Nat. Photonics* **17**, 143 (2023).
191. E. A. Douglas *et al.*, “Effect of precursors on propagation loss for plasma-enhanced chemical vapor deposition of SiN_x:H waveguides,” *Opt. Mater. Express* **6**, 2892 (2016).
192. Z. Shao *et al.*, “Ultra-low temperature silicon nitride photonic integration platform,” *Opt. Express* **24**, 1865 (2016).
193. J. Chiles *et al.*, “Deuterated silicon nitride photonic devices for broadband optical frequency comb generation,” *Opt. Lett.* **43**, 1527 (2018).
194. D. Bose *et al.*, “Anneal-free ultra-low loss silicon nitride integrated photonics,” *Light Sci. Appl.* **13**, 156 (2024).
195. D.-G. Kim *et al.*, “Universal light-guiding geometry for on-chip resonators having extremely high Q-factor,” *Nat. Commun.* **11**, 5933 (2020).
196. M. Garrett *et al.*, “Integrated microwave photonic notch filter using a heterogeneously integrated Brillouin and active-silicon photonic circuit,” *Nat. Commun.* **14**, 7544 (2023).
197. R. Schilling *et al.*, “Ultrahigh-Q on-chip silicon-germanium microresonators,” *Optica* **9**, 284 (2022).
198. R. Soref, “The past, present, and future of silicon photonics,” *IEEE J. Sel. Top. Quantum Electron.* **12**, 1678 (2006).
199. Z. Tao *et al.*, “Versatile photonic molecule switch in multimode microresonators,” *Light Sci. Appl.* **13**, 51 (2024).
200. S. A. Miller *et al.*, “Low-loss silicon platform for broadband mid-infrared photonics,” *Optica* **4**, 707 (2017).
201. J. S. Penadés *et al.*, “Suspended silicon waveguides for long-wave infrared wavelengths,” *Opt. Lett.* **43**, 795 (2018).
202. L. Zhang *et al.*, “Nonlinear group IV photonics based on silicon and germanium: from near-infrared to mid-infrared,” *Nanophotonics* **3**, 247 (2014).
203. L. Carletti *et al.*, “Nonlinear optical response of low loss silicon germanium waveguides in the mid-infrared,” *Opt. Express* **23**, 8261 (2015).
204. M. Sinobad *et al.*, “Mid-infrared octave spanning supercontinuum generation to 8.5 μm in silicon-germanium waveguides,” *Optica* **5**, 360 (2018).
205. W. Xie *et al.*, “Silicon-integrated nonlinear III–V photonics,” *Photonics Res.* **10**, 535 (2022).
206. X. Liu *et al.*, “Aluminum nitride nanophotonics for beyond-octave soliton microcomb generation and self-referencing,” *Nat. Commun.* **12**, 5428 (2021).
207. Y. He *et al.*, “High-speed tunable microwave-rate soliton microcomb,” *Nat. Commun.* **14**, 3467 (2023).
208. P. Latawiec *et al.*, “On-chip diamond Raman laser,” *Optica* **2**, 924 (2015).
209. M. Ruf *et al.*, “Quantum networks based on color centers in diamond,” *J. Appl. Phys.* **130**, 070901 (2021).
210. P. K. Shandilya *et al.*, “Diamond integrated quantum nanophotonics: spins, photons and phonons,” *J. Lightwave Technol.* **40**, 7538 (2022).
211. D. M. Lukin, M. A. Guidry, and J. Vučković, “Integrated quantum photonics with silicon carbide: challenges and prospects,” *PRX Quantum* **1**, 020102 (2020).
212. A. A. Savchenkov *et al.*, “Optical resonators with ten million finesse,” *Opt. Express* **15**, 6768 (2007).
213. X. Zhang and A. M. Armani, “Silica microtoroid resonator sensor with monolithically integrated waveguides,” *Opt. Express* **21**, 23592 (2013).
214. J. Liu *et al.*, “High-yield, wafer-scale fabrication of ultralow-loss, dispersion-engineered silicon nitride photonic circuits,” *Nat. Commun.* **12**, 2236 (2021).
215. S. Fujii *et al.*, “All-precision-machining fabrication of ultrahigh-Q crystalline optical microresonators,” *Optica* **7**, 694 (2020).
216. K. N. Min’kov *et al.*, “Fabrication of high-Q crystalline whispering gallery mode microcavities using single-point diamond turning,” *J. Opt. Technol.* **88**, 348 (2021).
217. M. Wang *et al.*, “Fabrication and packaging for high-Q CaF₂ crystalline resonators with modal modification,” *Chin. Opt. Lett.* **17**, 111401 (2019).
218. V. S. Ilchenko *et al.*, “Nonlinear optics and crystalline whispering gallery mode cavities,” *Phys. Rev. Lett.* **92**, 043901 (2004).
219. A. A. Savchenkov *et al.*, “Kilohertz optical resonances in dielectric crystal cavities,” *Phys. Rev. A* **70**, 051804 (2004).

220. M. Cai, O. Painter, and K. J. Vahala, "Observation of critical coupling in a fiber taper to a silica-microsphere whispering-gallery mode system," *Phys. Rev. Lett.* **85**, 74 (2000).
221. M. Cai, G. Hunziker, and K. Vahala, "Fiber-optic add-drop device based on a silica microsphere-whispering gallery mode system," *IEEE Photon. Technol. Lett.* **11**, 686 (1999).
222. P. Wang *et al.*, "Lead silicate glass microsphere resonators with absorption-limited Q," *Appl. Phys. Lett.* **98**, 181105 (2011).
223. T. Tan *et al.*, "Multispecies and individual gas molecule detection using Stokes solitons in a graphene over-modal microresonator," *Nat. Commun.* **12**, 6716 (2021).
224. T. Kippenberg, S. Spillane, and K. Vahala, "Demonstration of ultra-high-Q small mode volume toroid microcavities on a chip," *Appl. Phys. Lett.* **85**, 6113 (2004).
225. M. H. P. Pfeiffer *et al.*, "Octave-spanning dissipative Kerr soliton frequency combs in Si₃N₄ microresonators," *Optica* **4**, 684 (2017).
226. P. Maier *et al.*, "Sub-kHz-linewidth external-cavity laser (ECL) with Si₃N₄ resonator used as a tunable pump for a Kerr frequency comb," *J. Lightwave Technol.* **41**, 3479 (2023).
227. Y. Liu *et al.*, "A photonic integrated circuit-based erbium-doped amplifier," *Science* **376**, 1309 (2022).
228. Y. Liu *et al.*, "A fully hybrid integrated erbium-based laser," *Nat. Photonics* **18**, 829 (2024).
229. J. Liu *et al.*, "Photonic microwave generation in the X- and K-band using integrated soliton microcombs," *Nat. Photonics* **14**, 486 (2020).
230. Y. Wang, Y. Jiao, and K. Williams, "Scaling photonic integrated circuits with InP technology: a perspective," *APL Photonics* **9**, 050902 (2024).
231. D. Liang and J. E. Bowers, "Recent progress in lasers on silicon," *Nat. Photonics* **4**, 511 (2010).
232. Y. Gao *et al.*, "High-power, narrow-linewidth, miniaturized silicon photonic tunable laser with accurate frequency control," *J. Lightwave Technol.* **38**, 265 (2020).
233. T. Tekin, "Review of packaging of optoelectronic, photonic, and MEMS components," *IEEE J. Sel. Top. Quantum Electron.* **17**, 704 (2011).
234. M. He *et al.*, "Two-microlens coupling scheme with revolved hyperboloid sol-gel microlens arrays for high-power-efficiency optical coupling," *J. Lightwave Technol.* **24**, 2940 (2006).
235. K. Kunze *et al.*, "Microlens arrays for multichannel laser-to-waveguide coupling," *Appl. Opt.* **63**, 5876 (2024).
236. M. R. Billah *et al.*, "Hybrid integration of silicon photonics circuits and InP lasers by photonic wire bonding," *Optica* **5**, 876 (2018).
237. N. Lindenmann *et al.*, "Photonic wire bonding: a novel concept for chip-scale interconnects," *Opt. Express* **20**, 17667 (2012).
238. C. Xiang *et al.*, "3D integration enables ultralow-noise isolator-free lasers in silicon photonics," *Nature* **620**, 78 (2023).
239. S. Keyvaninia *et al.*, "Heterogeneously integrated III-V/silicon distributed feedback lasers," *Opt. Lett.* **38**, 5434 (2013).
240. A. W. Fang *et al.*, "Electrically pumped hybrid AlGaInAs-silicon evanescent laser," *Opt. Express* **14**, 9203 (2006).
241. C. Xiang *et al.*, "High-performance lasers for fully integrated silicon nitride photonics," *Nat. Commun.* **12**, 6650 (2021).
242. G. Roelkens *et al.*, "Present and future of micro-transfer printing for heterogeneous photonic integrated circuits," *APL Photonics* **9**, 010901 (2024).
243. B. Haq *et al.*, "Micro-transfer-printed III-V-on-silicon C-band semiconductor optical amplifiers," *Laser Photonics Rev.* **14**, 1900364 (2020).
244. J. R. Vaskasi *et al.*, "High wall-plug efficiency and narrow linewidth III-V-on-silicon C-band DFB laser diodes," *Opt. Express* **30**, 27983 (2022).
245. A. Lee *et al.*, "Continuous-wave InAs/GaAs quantum-dot laser diodes monolithically grown on Si substrate with low threshold current densities," *Opt. Express* **20**, 22181 (2012).
246. Y. Arakawa and H. Sakaki, "Multidimensional quantum well laser and temperature-dependence of its threshold current," *Appl. Phys. Lett.* **40**, 939 (1982).
247. Z. Zhou *et al.*, "Prospects and applications of on-chip lasers," *Elight* **3**, 1 (2023).
248. Y. Wan *et al.*, "1.3 μm quantum dot-distributed feedback lasers directly grown on (001) Si," *Laser Photonics Rev.* **14**, 2000037 (2020).
249. C. Shang *et al.*, "High-temperature reliable quantum-dot lasers on Si with misfit and threading dislocation filters," *Optica* **8**, 749 (2021).
250. P. Kik and A. Polman, "Cooperative upconversion as the gain-limiting factor in Er doped miniature Al₂O₃ optical waveguide amplifiers," *J. Appl. Phys.* **93**, 5008 (2003).
251. H. R. Telle *et al.*, "Carrier-envelope offset phase control: a novel concept for absolute optical frequency measurement and ultrashort pulse generation," *Appl. Phys. B* **69**, 327 (1999).
252. Z. Li *et al.*, "Experimental observations of bright dissipative cavity solitons and their collapsed snaking in a Kerr resonator with normal dispersion driving," *Optica* **7**, 1195 (2020).
253. S. Coen and M. Erkintalo, "Universal scaling laws of Kerr frequency combs," *Opt. Lett.* **38**, 1790 (2013).
254. J. Gu *et al.*, "Octave-spanning soliton microcomb in silica micro-disk resonators," *Opt. Lett.* **48**, 1100 (2023).
255. P.-Y. Wang *et al.*, "Octave soliton microcombs in lithium niobate microresonators," *Opt. Lett.* **49**, 1729 (2024).
256. M. H. Anderson *et al.*, "Zero dispersion Kerr solitons in optical microresonators," *Nat. Commun.* **13**, 4764 (2022).
257. A. F. J. Runge *et al.*, "Infinite hierarchy of solitons: Interaction of Kerr nonlinearity with even orders of dispersion," *Phys. Rev. Res.* **3**, 013166 (2021).
258. H. Taheri and A. B. Matsko, "Quartic dissipative solitons in optical Kerr cavities," *Opt. Lett.* **44**, 3086 (2019).
259. S. Yao, K. Liu, and C. Yang, "Pure quartic solitons in dispersion-engineered aluminum nitride micro-cavities," *Opt. Express* **29**, 8312 (2021).
260. Y. L. Qiang, T. J. Alexander, and C. M. de Sterke, "Generalized sixth-order dispersion solitons," *Phys. Rev. A* **105**, 023501 (2022).
261. P. Parra-Rivas, D. Gomila, and L. Gelens, "Coexistence of stable dark and bright-soliton Kerr combs in normal-dispersion resonators," *Phys. Rev. A* **95**, 053863 (2017).
262. Z. Xiao *et al.*, "Near-zero-dispersion soliton and broadband modulational instability Kerr microcombs in anomalous dispersion," *Light Sci. Appl.* **12**, 33 (2023).
263. S. Zhang, T. Bi, and P. Del'Haye, "Quintic dispersion soliton frequency combs in a microresonator," *Laser Photonics Rev.* **17**, 2300075 (2023).
264. S.-P. Yu *et al.*, "A continuum of bright and dark-pulse states in a photonic-crystal resonator," *Nat. Commun.* **13**, 3134 (2022).
265. X. Lu *et al.*, "Multi-mode microcavity frequency engineering through a shifted grating in a photonic crystal ring," *Photonics Res.* **11**, A72 (2023).
266. H. Shu *et al.*, "Submilliwatt, widely tunable coherent microcomb generation with feedback-free operation," *Adv. Photonics* **5**, 036007 (2023).
267. H. Wang *et al.*, "Dirac solitons in optical microresonators," *Light Sci. Appl.* **9**, 205 (2020).
268. Z. Lin *et al.*, "Turnkey generation of Kerr soliton microcombs on thin-film lithium niobate on insulator microresonators powered by the photorefractive effect," *Opt. Express* **29**, 42932 (2021).
269. Y. Okawachi *et al.*, "Active tuning of dispersive waves in Kerr soliton combs," *Opt. Lett.* **47**, 2234 (2022).
270. Z. Yuan *et al.*, "Soliton pulse pairs at multiple colours in normal dispersion microresonators," *Nat. Photonics* **17**, 977 (2023).
271. Q.-X. Ji, *et al.*, "Engineered zero-dispersion microcombs using CMOS-ready photonics," *Optica* **10**, 279 (2023).

272. D. Goldring, U. Levy, and D. Mendlovic, "Highly dispersive micro-ring resonator based on one dimensional photonic crystal waveguide design and analysis," *Opt. Express* **15**, 3156 (2007).
273. X. Lu, A. McClung, and K. Srinivasan, "High-Q slow light and its localization in a photonic crystal microring," *Nat. Photonics* **16**, 66 (2022).
274. G. Moille *et al.*, "Fourier synthesis dispersion engineering of photonic crystal microrings for broadband frequency combs," *Commun. Phys.* **6**, 144 (2023).
275. S. Zhang *et al.*, "Spectral extension and synchronization of microcombs in a single microresonator," *Nat. Commun.* **11**, 6384 (2020).
276. G. Moille *et al.*, "Ultra-broadband Kerr microcomb through soliton spectral translation," *Nat. Commun.* **12**, 7275 (2021).
277. X. Xue *et al.*, "Microresonator Kerr frequency combs with high conversion efficiency," *Laser Photonics Rev.* **11**, 1600276 (2017).
278. J. M. C. Boggio *et al.*, "Efficient Kerr soliton comb generation in micro-resonator with interferometric back-coupling," *Nat. Commun.* **13**, 1292 (2022).
279. J. Zang *et al.*, "Laser-power consumption of soliton formation in a bidirectional Kerr resonator," arXiv:2401.16740 (2024).
280. J. K. Jang *et al.*, "Conversion efficiency of soliton Kerr combs," *Opt. Lett.* **46**, 3657 (2021).
281. X. Zhang *et al.*, "Advances in resonator-based Kerr frequency combs with high conversion efficiencies," *npj Nanophotonics* **1**, 26 (2024).
282. Q.-F. Yang *et al.*, "Efficient microresonator frequency combs," *eLight* **4**, 18 (2024).
283. C. Bao *et al.*, "Nonlinear conversion efficiency in Kerr frequency comb generation," *Opt. Lett.* **39**, 6126 (2014).
284. R. Kormokar, M. H. M. Shamim, and M. Rochette, "Energy conversion efficiency from a high-order soliton to fundamental solitons in the presence of Raman scattering," *J. Opt. Soc. Am. B* **40**, 412 (2023).
285. J. Zang *et al.*, "High-efficiency microcombs aligned with ITU-T grid for WDM optical interconnects," in *Optical Fiber Communication Conference* (2023), paper Th1B.6.
286. I. Rebolledo-Salgado *et al.*, "Platonic dynamics in photonic molecules," *Commun. Phys.* **6**, 303 (2023).
287. K. Nishimoto *et al.*, "Investigation of the phase noise of a microresonator soliton comb," *Opt. Express* **28**, 19295 (2020).
288. F. Lei *et al.*, "Optical linewidth of soliton microcombs," *Nat. Commun.* **13**, 3161 (2022).
289. T. E. Drake *et al.*, "Thermal decoherence and laser cooling of Kerr microresonator solitons," *Nat. Photonics* **14**, 480 (2020).
290. G. Moille *et al.*, "Kerr-microresonator soliton frequency combs at cryogenic temperatures," *Phys. Rev. Appl.* **12**, 034057 (2019).
291. Q.-F. Yang *et al.*, "Dispersive-wave induced noise limits in miniature soliton microwave sources," *Nat. Commun.* **12**, 1442 (2021).
292. D. Hou *et al.*, "Long-term stabilization of fiber laser using phase-locking technique with ultra-low phase noise and phase drift," *IEEE J. Sel. Top. Quantum Electron.* **20**, 456 (2014).
293. G. Rizzelli *et al.*, "Phase noise impact and scalability of self-homodyne short-reach coherent transmission using DFB lasers," *J. Lightwave Technol.* **40**, 37 (2022).
294. E. D. Black, "An introduction to Pound-Drever-Hall laser frequency stabilization," *Am. J. Phys.* **69**, 79 (2001).
295. D. Kwon *et al.*, "Ultrastable microwave and soliton-pulse generation from fibre-photonic-stabilized microcombs," *Nat. Commun.* **13**, 381 (2022).
296. R. Liu *et al.*, "Low-phase-noise microwave generation with a free-running dual-pumped Si₃N₄ soliton microcomb," *Opt. Lett.* **49**, 754 (2024).
297. Z.-Y. Wang *et al.*, "Numerical characterization of soliton microcomb in an athermal hybrid Si₃N₄-TiO₂ microring," *Appl. Opt.* **61**, 4329 (2022).
298. A. F. Fercher *et al.*, "Optical coherence tomography-principles and applications," *Rep. Prog. Phys.* **66**, 239 (2003).
299. A. C. Triscari *et al.*, "Quiet point engineering for low-noise microwave generation with soliton microcombs," *Commun. Phys.* **6**, 318 (2023).
300. C. Lao *et al.*, "Quantum decoherence of dark pulses in optical microresonators," *Nat. Commun.* **14**, 1802 (2023).
301. W. Weng *et al.*, "Spectral purification of microwave signals with disciplined dissipative Kerr solitons," *Phys. Rev. Lett.* **122**, 013902 (2019).
302. W. Weng *et al.*, "Microresonator dissipative Kerr solitons synchronized to an optoelectronic oscillator," *Phys. Rev. Appl.* **17**, 024030 (2022).
303. F. Lei *et al.*, "Self-injection-locked optical parametric oscillator based on microcombs," *Optica* **11**, 420 (2024).
304. J. D. Jost *et al.*, "Counting the cycles of light using a self-referenced optical microresonator," *Optica* **2**, 706 (2015).
305. L. Cai *et al.*, "Octave-spanning microcomb generation in 4H-silicon-carbide-on-insulator photonics platform," *Photonics Res.* **10**, 870 (2022).
306. P. Del'Haye *et al.*, "Full stabilization of a microresonator-based optical frequency comb," *Phys. Rev. Lett.* **101**, 053903 (2008).
307. V. Brasch *et al.*, "Self-referenced photonic chip soliton Kerr frequency comb," *Light Sci. Appl.* **6**, e16202 (2017).
308. H. Weng *et al.*, "Directly accessing octave-spanning dissipative Kerr soliton frequency combs in an AlN microresonator," *Photonics Res.* **9**, 1351 (2021).
309. T. E. Drake *et al.*, "Terahertz-rate Kerr-microresonator optical clockwork," *Phys. Rev. X* **9**, 031023 (2019).
310. K. Wu *et al.*, "Vernier microcombs for high-frequency carrier envelope offset and repetition rate detection," *Optica* **10**, 626 (2023).
311. L. Stern *et al.*, "Direct Kerr frequency comb atomic spectroscopy and stabilization," *Sci. Adv.* **6**, eaax6230 (2020).
312. M. Yu *et al.*, "Gas-phase microresonator-based comb spectroscopy without an external pump laser," *ACS Photonics* **5**, 2780 (2018).
313. E. Zano *et al.*, "Plasmonic-enhanced multiparameter direct microcomb spectroscopy," *Optica* **11**, 1192 (2024).
314. Q.-F. Yang *et al.*, "Vernier spectrometer using counterpropagating soliton microcombs," *Science* **363**, 965 (2019).
315. J. N. Eckstein, A. I. Ferguson, and T. W. Hansch, "High-resolution 2-photon spectroscopy with picosecond light-pulses," *Phys. Rev. Lett.* **40**, 847 (1978).
316. N. Picque and T. W. Haensch, "Frequency comb spectroscopy," *Nat. Photonics* **13**, 146 (2019).
317. A. R. Johnson *et al.*, "Microresonator-based comb generation without an external laser source," *Opt. Express* **22**, 1394 (2014).
318. D. C. Cole *et al.*, "Kerr-microresonator solitons from a chirped background," *Optica* **5**, 1304 (2018).
319. S.-J. Lee *et al.*, "Ultrahigh scanning speed optical coherence tomography using optical frequency comb generators," *Jpn. J. Appl. Phys.* **40**, L878 (2001).
320. A. Dutt *et al.*, "On-chip dual-comb source for spectroscopy," *Sci. Adv.* **4**, e1701858 (2018).
321. Q.-F. Yang *et al.*, "Counter-propagating solitons in microresonators," *Nat. Photonics* **11**, 560 (2017).
322. M. Yu *et al.*, "Silicon-chip-based mid-infrared dual-comb spectroscopy," *Nat. Commun.* **9**, 1869 (2018).
323. M.-G. Suh and K. J. Vahala, "Soliton microcomb range measurement," *Science* **359**, 884 (2018).
324. J. Wang *et al.*, "Long-distance ranging with high precision using a soliton microcomb," *Photonics Res.* **8**, 1964 (2020).
325. R. Collis, "Lidar," *Appl. Opt.* **9**, 1782 (1970).
326. F. Keilmann, C. Gohle, and R. Holzwarth, "Time-domain mid-infrared frequency-comb spectrometer," *Opt. Lett.* **29**, 1542 (2004).

327. I. Coddington *et al.*, "Rapid and precise absolute distance measurements at long range," *Nat. Photonics* **3**, 351 (2009).
328. Y. Yang *et al.*, "Optical ranging using coherent Kerr soliton dual-microcombs with extended ambiguity distance," *J. Lightwave Technol.* **42**, 5450 (2024).
329. A. Lukashchuk *et al.*, "Dual chirped microcomb based parallel ranging at megapixel-line rates," *Nat. Commun.* **13**, 3280 (2022).
330. P. J. Marchand *et al.*, "Soliton microcomb based spectral domain optical coherence tomography," *Nat. Commun.* **12**, 427 (2021).
331. R. Leitgeb, C. K. Hitzenberger, and A. F. Fercher, "Performance of Fourier domain vs. time domain optical coherence tomography," *Opt. Express* **11**, 889 (2003).
332. T. Bajraszewski *et al.*, "Improved spectral optical coherence tomography using optical frequency comb," *Opt. Express* **16**, 4163 (2008).
333. T. Melton *et al.*, "Optical coherence tomography imaging and noise characterization based on 1 μm microresonator frequency combs," *APL Photonics* **9**, 086105 (2024).
334. X. Li *et al.*, "Multi-scale reconstruction of undersampled spectral-spatial OCT data for coronary imaging using deep learning," *IEEE Trans. Biomed. Eng.* **69**, 3667 (2022).
335. T. Wilken *et al.*, "A spectrograph for exoplanet observations calibrated at the centimetre-per-second level," *Nature* **485**, 611 (2012).
336. E. Obrzud *et al.*, "A microphotonic astrocomb," *Nat. Photonics* **13**, 31 (2019).
337. T. Wilken *et al.*, "High-precision calibration of spectrographs," *Mon. Not. R. Astron. Soc.* **405**, L16 (2010).
338. P. Marin-Palomo *et al.*, "Microresonator-based solitons for massively parallel coherent optical communications," *Nature* **546**, 274 (2017).
339. A. Fulop *et al.*, "High-order coherent communications using mode-locked dark-pulse Kerr combs from microresonators," *Nat. Commun.* **9**, 1598 (2018).
340. B. Corcoran *et al.*, "Ultra-dense optical data transmission over standard fibre with a single chip source," *Nat. Commun.* **11**, 2568 (2020).
341. A. A. Jorgensen *et al.*, "Petabit-per-second data transmission using a chip-scale microcomb ring resonator source," *Nat. Photonics* **16**, 798 (2022).
342. B. M. M. Heffernan *et al.*, "60 Gbps real-time wireless communications at 300 GHz carrier using a Kerr microcomb-based source," *APL Photonics* **8**, 066106 (2023).
343. C. Prayoonyong *et al.*, "Frequency comb distillation for optical superchannel transmission," *J. Lightwave Technol.* **39**, 6097 (2021).
344. Y. Geng *et al.*, "Coherent optical communications using coherence-cloned Kerr soliton microcombs," *Nat. Commun.* **13**, 1070 (2022).
345. J. Feldmann *et al.*, "Parallel convolutional processing using an integrated photonic tensor core," *Nature* **589**, 52 (2021).
346. B. Bai *et al.*, "Microcomb-based integrated photonic processing unit," *Nat. Commun.* **14**, 66 (2023).
347. D. A. B. Miller, "Attojoule optoelectronics for low-energy information processing and communications," *J. Lightwave Technol.* **35**, 346 (2017).
348. Y. Shen *et al.*, "Deep learning with coherent nanophotonic circuits," *Nat. Photonics* **11**, 441 (2017).
349. X. Lin *et al.*, "All-optical machine learning using diffractive deep neural networks," *Science* **361**, 1004 (2018).
350. S. Xu *et al.*, "High-order tensor flow processing using integrated photonic circuits," *Nat. Commun.* **13**, 7970 (2022).
351. B. J. Shastri *et al.*, "Photonics for artificial intelligence and neuromorphic computing," *Nat. Photonics* **15**, 102 (2021).
352. D. Marpaung, J. Yao, and J. Capmany, "Integrated microwave photonics," *Nat. Photonics* **13**, 80 (2019).
353. B. Wang *et al.*, "Towards high-power, high-coherence, integrated photonic mmWave platform with microcavity solitons," *Light Sci. Appl.* **10**, 4 (2021).
354. E. Lucas *et al.*, "Ultralow-noise photonic microwave synthesis using a soliton microcomb-based transfer oscillator," *Nat. Commun.* **11**, 374 (2020).
355. S. Sun *et al.*, "Integrated optical frequency division for microwave and mmWave generation," *Nature* **627**, 540 (2024).
356. I. Kudelin *et al.*, "Photonic chip-based low-noise microwave oscillator," *Nature* **627**, 534 (2024).
357. Y. Zhao *et al.*, "All-optical frequency division on-chip using a single laser," *Nature* **627**, 546 (2024).
358. X. Xu *et al.*, "Advanced adaptive photonic RF filters with 80 taps based on an integrated optical micro-comb source," *J. Lightwave Technol.* **37**, 1288 (2019).
359. X. Xu *et al.*, "Broadband RF channelizer based on an integrated optical frequency Kerr comb source," *J. Lightwave Technol.* **36**, 4519 (2018).
360. X. Xu *et al.*, "Photonic microwave true time delays for phased array antennas using a 49 GHz FSR integrated optical micro-comb source Invited," *Photonics Res.* **6**, B30 (2018).
361. M. Tan *et al.*, "Microwave and RF photonic fractional hilbert transformer based on a 50 GHz Kerr micro-comb," *J. Lightwave Technol.* **37**, 6097 (2019).
362. X. Xu *et al.*, "Reconfigurable broadband microwave photonic intensity differentiator based on an integrated optical frequency comb source," *APL Photonics* **2**, 096104 (2017).
363. X. Xu *et al.*, "Photonic RF and microwave integrator based on a transversal filter with soliton crystal microcombs," *IEEE Trans. Circuits Syst.* **67**, 3582 (2020).
364. M. Tan *et al.*, "Photonic RF arbitrary waveform generator based on a soliton crystal micro-comb source," *J. Lightwave Technol.* **38**, 6221 (2020).
365. T. G. Nguyen *et al.*, "Integrated frequency comb source based Hilbert transformer for wideband microwave photonic phase analysis," *Opt. Express* **23**, 22087 (2015).
366. B. Wang *et al.*, "Radio-frequency line-by-line Fourier synthesis based on optical soliton microcombs," *Photonics Res.* **10**, 932 (2022).
367. W. Han *et al.*, "Dual-polarization RF channelizer based on microcombs," *Opt. Express* **32**, 11281 (2024).
368. J. Hu *et al.*, "Reconfigurable radiofrequency filters based on versatile soliton microcombs," *Nat. Commun.* **11**, 4377 (2020).
369. X. Xue *et al.*, "Microcomb-based true-time-delay network for microwave beamforming with arbitrary beam pattern control," *J. Lightwave Technol.* **36**, 2312 (2018).
370. X. Xu *et al.*, "Broadband microwave frequency conversion based on an integrated optical micro-comb source," *J. Lightwave Technol.* **38**, 332 (2020).
371. A. Lukashchuk *et al.*, "Chaotic microcomb-based parallel ranging," *Nat. Photonics* **17**, 814 (2023).
372. P. Li *et al.*, "Scalable parallel ultrafast optical random bit generation based on a single chaotic microcomb," *Light Sci. Appl.* **13**, 66 (2024).
373. A. Lukashchuk *et al.*, "Chaotic microcomb inertia-free parallel ranging," *APL Photonics* **8**, 056102 (2023).
374. W. Xiong *et al.*, "3D parallel pulsed chaos LiDAR system," *Opt. Express* **32**, 11763 (2024).
375. Y. Liu *et al.*, "Parallel wavelength-division-multiplexed signal transmission and dispersion compensation enabled by soliton microcombs and microrings," *Nat. Commun.* **15**, 3645 (2024).
376. A. Rizzo *et al.*, "Massively scalable Kerr comb-driven silicon photonic link," *Nat. Photonics* **17**, 781 (2023).
377. I. S. Grudinin *et al.*, "Ultra high Q crystalline microcavities," *Opt. Commun.* **265**, 33 (2006).
378. W. Liang *et al.*, "Generation of near-infrared frequency combs from a MgF₂ whispering gallery mode resonator," *Opt. Lett.* **36**, 2290 (2011).